Proceedings, 5th Chaotic Modeling and Simulation International Conference, 12 – 15 June 2012, Athens Greece

Pattern Formation in Volumetrically Heated Fluids

Gregory Cartland Glover[1] Kaoru Fujimura[2] and Sotos Generalis[3]

[1] Marie Curie IE Fellow, Mathematics, Aston University, Birmingham B4 7ET, UK
(E-mail: g.cartland-glover@aston.ac.uk)
[2] Department of Applied Mathematics and Physics, Tottori University, Japan
(E-mail: kaoru@damp.tottori-u.ac.jp)
[3] Mathematics, Aston University, Birmingham B4 7ET, UK
(E-mail: s.c.generalis@aston.ac.uk)

Abstract. Finite element simulations have been performed along side Galerkin-type calculations that examined the development of volumetrically heated flow patterns in a horizontal layer controlled by the Prandtl number, Pr, and the Grashof number, Gr. The fluid was bounded by an isothermal plane above an adiabatic plane. In the simulations performed here, a number of convective polygonal planforms occurred, as Gr increased above the critical Grashof number, Gr_c at $Pr = 7$, while roll structures were observed for $Pr < 1$ at $2Gr_c$.
Keywords: Non-linear, bifurcation, stability, volumetric heating, asymmetric boundaries.

1 Introduction

This work is concerned with the numerical simulation of the early stage transition regime of an internally heated fluid layer situated between a conducting upper boundary and an insulating lower boundary. The study described here is motivated by earlier studies ([4], [6], [8]) and the importance such flow structures have in the development of flows found in many engineering and geophysical applications.

Examples of volumetric heating cover thermal convection driven by the radioactive decay of fluid components. Asfia and Dhir [2] who studied thermal convection in a pool that mimicked the motion caused by fission product decay in the molten fuel elements that collect in the lower head of a nuclear reactor during a severe accident. Briant and Weinberg [3] devised the molten salt nuclear reactor concept, where the fissile material is dissolved in the coolant and thus provides volumetric heating to the fluid phase. Geophysical flows in the Earth's mantle are driven by radioactive decay ([5], [10], [13], [14]). Tritton and Zarraga [18], Tasaka *et al.* [16], Takahashi *et al.* [15] have studied the phenomena experimentally using various approaches to generate fluid motion and record the structures observed.

Several numerical studies of thermal convection driven by internal heating have been performed using a variety of techniques to resolve the evolving circulation cells via the application of mean field approximations ([12]), finite amplitude expansions used in pseudospectral techniques ([8], [10], [13], [14], [9], [20], [17]) and finite volume or element approaches ([6], [11]).

Cartland Glover and Generalis [6] focussed on domains with aspect ratios of $\left\{1 : 4\sqrt{3} : 12\right\}$ suggested by Ichikawa *et al.* [11]. Several types of circulation cells were observed by Cartland Glover and Generalis [6], as Gr was increased. Nevertheless, two key factors that affected the development of the circulation cells in Cartland Glover and Generalis [6] was how the internal heating conditions were defined and the influence of the periodic conditions on the flow field. Cartland Glover and Generalis [6] assumed a constant temperature difference and varied the depth between the parallel plates to control Gr and the internal heating supplied. Therefore, a further study has been performed, where the variation of the internal heating condition was driven by the temperature difference rather than modifying the depth between the parallel planes, which is more consistent with experimental methods, for example Tasaka *et al.* [16] and Takahashi *et al.* [15]. The extent of the domain was also increased from $\left\{1 : 4\sqrt{3} : 12\right\}$ to $\{1 : 12 : 12\}$.

2 Theory

2.1 Non-dimensional numbers

Two non-dimensional numbers were used to control the volumetric heating supplied to the horizontal layer and the influence of the thermal diffusivity. These were the Grashof number with the form $Gr = g\rho^2\beta S_i L^5/2\mu^2 k$ and the Prandtl number, $Pr = c_p\mu/k$. Here S_i and L are the volumetric heat source and the layer depth. The fluid properties are defined by the specific heat capacity at constant pressure, c_p, thermal conductivity, k, dynamic viscosity, μ and the density, ρ. Several Gr over the range $1 \leq \varepsilon \leq 12$ were selected in order to vary the temperature difference at $Pr = 7$ and therefore the heat flux applied, where $\varepsilon = Gr/Gr_c$. Then Pr was varied to observe the influence of thermal diffusivity on the resolved flow states. The treatment of the non-dimensional numbers differs between the finite element method and the Galerkin-Tau type method.

2.2 Linear stability analysis

A linear normal mode analysis of the problem is resolved using a Galerkin-Tau approach. Chebyshev polynomials are used in the expansion of the pertubation equations, which are evaluated at collocation points as an eigenvalue problem via the QZ algorithm. The asymmentry in the boundary conditions is dealt with by applying the zero gradient condition to the bottom row of the matrix for the temperature equation. The boundary conditions applied to the temperature take the form $-0.5Gr(x^2 + 2 * x - 3)$ based on the profile reported by Roberts [12]. No-slip conditions are applied to the Orr-Sommerfeld equation. Note that 20 modes are used to resolve the neutral curves presented here.

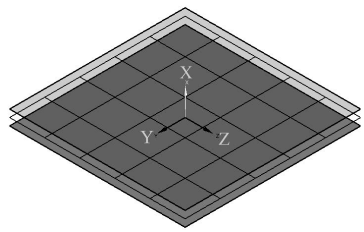

Fig. 1. Diagram of the homogeneous layer with an isothermal surface above an adiabatic surface. The coordinate axis is at the origin and the midplane surface is also indicated by the coarse grid.

2.3 Simulation method

As the solver used in the finite element method used dimensional equations [1], it is necessary to specify $S_i = 2k\Delta T_i/L^2$ in terms of Gr (see below) and $L = 0.007$ m, which was defined according to the experimental studies of Tasaka *et al.* [16]. The boundary conditions are $T|_{x=L} = T_r$, $\partial_x T|_{x=0} = 0$ K m^{-1}, $u|_{x=0} = v|_{x=0} = w|_{x=0} = u|_{x=L} = v|_{x=L} = w|_{x=L} = 0$ m s^{-1} and the initial conditions are $T = T_r$ and $u = v = w = 0$ m s^{-1}. T_r is the reference temperature of the fluid modelled. Periodic conditions are applied to the vertical surfaces of the domain Figure 1. Please refer to Cartland Glover and Generalis [6] for a thorough description of the specifications required to perform the finite element method. Key exceptions from [6] are the domain used, which was a square layer with an aspect ratio of $\{1 : 12 : 12\}$ that had the respective node resolution of $\{30 : 180 : 180\}$ and the assumed physical time-scale, $c_p\rho L^2/k$, to control the rate of convergence.

3 Results

The resultant solutions for convection caused by volumetrically heating a horizontal layer show the deviations from the conductive laminar state. At $Pr = 7$, the transition from conductive to convective flow occurs at $Gr_c = 198$, which corresponds to $Ra_c = 1386$ ([12], [11], [20]). The structures are indicated by the change in characteristic parameters, which are plotted between Figure 2 and Figure 5. Figure 2 presents the neutral curves obtained by the linear analysis. Contour plots of the temperature and the vertical velocity component for $Pr = 7$, where $\varepsilon\forall\,(1, 2, 3, 6, 12)$ are illustrated by Figure 3. The change of velocity components and the temperature with ε are plotted in Figure 4. Contour plots of the temperature and the vertical velocity component for $Pr\forall\,(0.005, 0.659-0.745, 0.802-0.883, 8.933)$ are given in Figure 5.

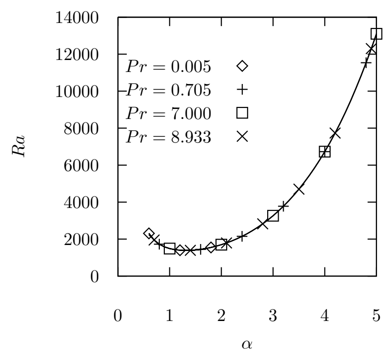

Fig. 2. Neutral curves of stability (solid lines) obtained from the linear normal mode analysis, where α is the wavenumber.

3.1 Fluids with Pr=7

The neutral curves obtained from the linear normal mode analysis are given in Figure 2, where the curves indicate the highest value allowed by the linear analysis for the basic flow to retain its laminar form. The curves for each Pr considered coincide with one another, which is consistent with the findings of Generalis and Nagata [8].

At ε=0, Figure 3 already shows non-vanishing hexagonal pattern. This is due to the fact that the lower bound of stable down-hexagons is subcritical i.e. ε <1. Indeed, the branch of stable down-hexagons ends up with a limiting point (or saddle-node point) at which the stable branch is connected with the solution branch of the transcritical bifurcation stemmed subcritically from the point ε=1. Note that the stable down-hexagons are generated in the following sequence: hexagons true to the transverse axis at $\varepsilon = 1$ (Figure 3A), hexagons perpendicular to the transverse axis (Figure 3B), hexagons aligned at $\sim 50^{\circ}$ to transverse axis (Figure 3C), polygonal structures (Figure 3D), hexagons with spokes (Figure 3E). Note that the change in the alignment of the hexagons between Figure 3A and 3C indicates that there is no preference between the wavenumbers for longitudinal or transverse waves.

The structures depicted Figure 3 are qualitatively comparable with the experimental studies of Takahashi *et al.* [15] and Tasaka *et al.* [16], where measurements of the temperature field [16] and the velocity field [15] were made $\varepsilon \in (3, 6)$. These conditions correspond to cases C and D presented in Figure 3. The increase in the size of the circulation cell is of a similar magnitude in both the experiments and the simulation. The range of vertical

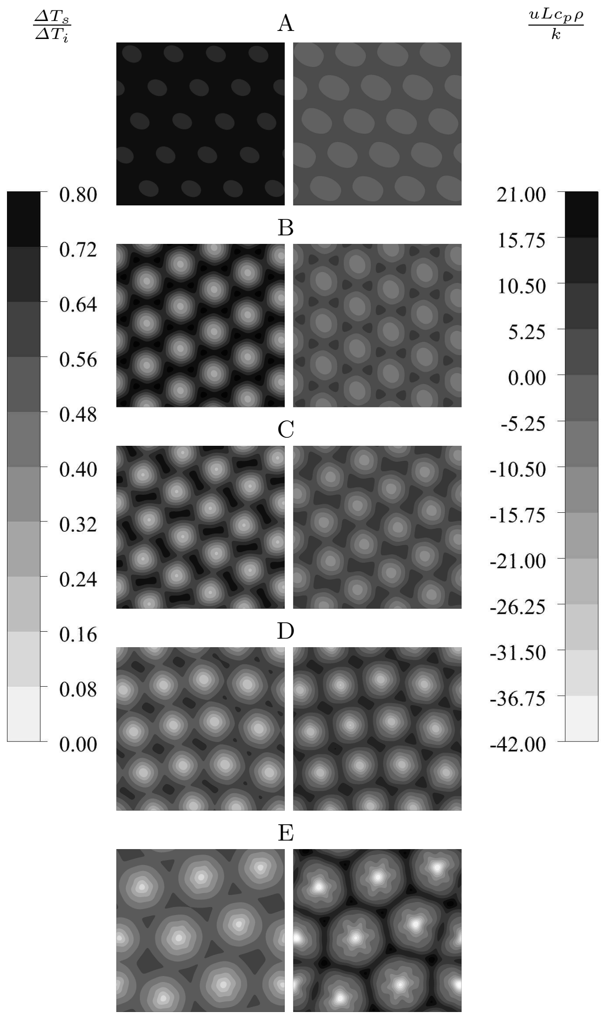

Fig. 3. Non-dimensional temperature (left) and vertical velocity (right) contours on the midplane surface in Figure 1. Here $\Delta T_s = |T - T_{\min}|_s$. Cases – A: $\varepsilon = 1$; B: $\varepsilon = 2$; C: $\varepsilon = 3$; D: $\varepsilon = 6$; E: $\varepsilon = 12$;

velocities observed in the simulations described are similar to those reported by Takahashi *et al.* [15].

In Figure 4 we show the change of key variables with ε for the simulations using the finite element code. A significant increase in all the velocity components at $\varepsilon = 1$ in Figure 4a. The increases in the velocity are associated with the change in the state of the fluid layer at the critical transition, where we conjecture that isotropic hexagons are formed. The patterns formed are

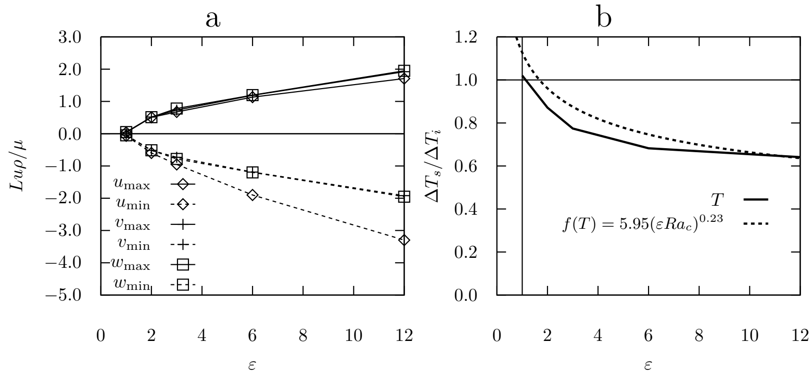

Fig. 4. Profiles against ε obtained from the finite element code. a) The maximum and the minimum values of the velocity components; b) $\Delta T_s/\Delta T_i = |T - T_{\min}|_s / \left(Gr\mu^2\right) / \left(g\rho^2\beta\ L^3\right)$, where s refers to the temperature extracted from the solved flow field. $f(T) = 5.95(\varepsilon * Ra_c)^{-0.23}$, an empirical profile given by Turcotte *et al.* [19] as reported by Takahashi *et al.* [15]; Horizontal line: Conduction condition; Vertical line: Transition between conduction and convection.

considered to be isotropic as the minima and maxima of the v and w display similar magnitudes.

The down-welling minimum velocity indicated in figure 11 of Takahashi *et al.* [15] gave vertical velocities, which were approximately one third less than the vertical velocities in Figure 4. This difference could be due to methods used to assess the minimum vertical velocity or the influence of the heat flux across the lower boundary used. The minimum vertical velocity of Takahashi *et al.* [15] was determined from the planes defined by the laser sheets used for their PIV measurements, while the velocities in Figure 4a are the minimum and maximum values for the whole of the simulated domain.

The effect of the transition from conductive to convective flow is also shown by the change in the temperature difference relative to the initial or conductive temperature difference (Figure 4b). At higher heat fluxes the temperature difference caused by convection drops below the conductive temperature difference. This is due to the influence that cellular convection has on the layer as energy from the volumetric heat source is used to drive the fluids across the layer [5]. A portion of the internal heating supplied is also lost from the system through the top isothermal boundary [18]. An empirical relation of the decrease in the temperature difference due to convection is also plotted in Figure 4 [19].

3.2 Other fluids

To confirm the secondary flows predicted by the finite element code soon after Gr_c are appropriate, fluids of different Pr were tested for $\varepsilon = 2$. For

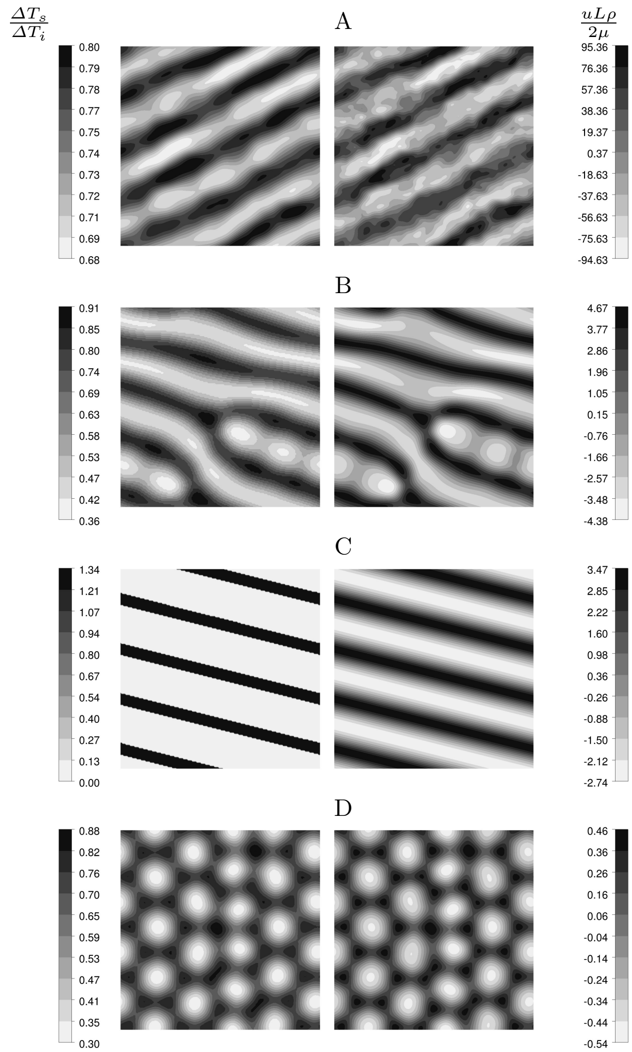

Fig. 5. Non-dimensional temperature (left) and vertical velocity (right) contours on the midplane surface in Figure 1, for different Pr at $\varepsilon = 2$. Here $\Delta T_s = |T - T_{\min}|_s$. Cases – A: $Pr = 0.005$; B: $Pr = 0.705$; C: $Pr = 0.883$; D: $Pr = 8.933$;

$Pr < 1$, the circulation cells take the form of stable ($0.5 < \mathrm{Pr} < 1$) or unstable ($Pr < 0.1$) two-dimensional rolls. While a mix of polygonal structures occur for $Pr = 8.933$. For $Pr \sim 0.70$ dislocations in the roll structures are also observed, which may disappear in time-averaged plots obtained from a time-marching solution. For $Pr \sim 0.85$, where supercritical or high pressure fluids were considered, small non-measureable differences in the temperature resulted from the strict limits applied in the Boussinesq approximation. This lead to the formation of sharply defined differences in the temperature.

4 Conclusions

The main interest in the present work is the hierarchical transition from conductive flow to convective flow and on to the turbulent regime in an asymmetric horizontal layer. We have concentrated on the stability boundary of the basic flow in order to compare states found numerically with those observed in experiments ([16],[15]). The present study used both finite element simulations and linear stability analysis to indicate that hexagonal cells are the preferred mode for the instability evolution of homogeneous systems at and just beyond the critical point for $Pr = 7$.

Beyond $\varepsilon = 6$ at $Pr = 7$, the finite element code predicts that the secondary structures deform resulting in different possibly rectangular states that are qualitatively comparable with the experimental studies of the Takeda group ([16],[15]). Between $\varepsilon = 1$ and $\varepsilon = 3$ the changes in orientation of the hexagons indicates that there is no preference between the wavenumbers for transverse and longitudinal waves. Further non-linear analyses are being performed to explore the stability of the flow patterns observed at the transition to convective flow for a homogeneously heated layer with asymmetric boundary conditions.

Acknowledgements

We wish to thank the Institute for Safety Research at the Helmholtz-Zentrum Dresden-Rossendorf for kindly allowing access to the computational cluster upon which the computational fluid dynamic calculations were performed.

Nomenclature

c_p	specific heat capacity at constant pressure, J kg^{-1} K^{-1}
Gr	Grashof number, $Gr = g\beta\rho^2 S_i L^5/2\mu^2 k$
Gr_c	critical Grashof number, Gr_c
g	acceleration due to gravity, m s^{-2}
k	thermal conductivity, W m^{-1} K^{-1}
L	characteristic length, 0.007 m
Pr	Prandtl number, $Pr = c_p/\mu k$
Ra	Rayleigh number $Ra = GrPr$
Ra_c	critical Rayleigh number $Ra_c = 1386$
S_i	volumetric heat source $S_i = 2k\Delta T_i/L^2$, kg m^{-1} s^{-3}
T	temperature, K
T_r	reference temperature, K

ΔT_i	initial temperature difference, $\Delta T_i = \left(Gr\mu^2\right) / \left(g\rho^2\beta\ L^3\right)$, K
ΔT_s	temperature difference of the solved flow, K
t	time, s
u, v, w	velocity vector components, m s^{-1}
x, y, z	direction vector components, m

Greek symbols

α	wavenumber
β	expansion coefficient, 1/K
ε	reduced Grashof number = Gr/Gr_c
μ	dynamic viscosity, kg m^{-1} s^{-1}
ρ	density, kg m^{-3}

References

1. ANSYS. *ANSYS CFX 12*, Canonsburg, USA, 2009. ANSYS Inc.
2. F. J. Asfia and V. K. Dhir. An experimental study of natural convection in a volumetrically heated spherical pool bounded on top with a rigid wall. Nuclear Engineering & Design, 163:333-348, 1996.
3. R. C. Briant and A. M. Weinberg. Molten fluorides as power reactor fuels. Nuclear Science & Engineering, 2:797-803, 1957.
4. F. H. Busse. The stability of finite amplitude cellular convection and its relation to an extremum principle. Journal of Fluid Mechanics, 30(4):625-649, 1967.
5. F. H. Busse. Fundamentals of thermal convection. In W. R. Peltier, editor, *Mantle Convection. Plate Tectonics and Global Dynamics (Fluid mechanics of astrophysics and geophysics vol 4)* pages 23-95, New York, 1989. Gordon and Breach.
6. G. M. Cartland Glover and S. C. Generalis. Pattern competition in homogeneously heated fluid layers. Engineering Applications of Computational Fluid Mechanics, 3(2):164-174, 2009.
7. R. M. Clever and F. H. Busse. Hexagonal convection cells under conditions of vertical symmetry Physical Review E, 53(3):2037-2040, 1996.
8. S. Generalis and M. Nagata Transition in homogeneously heated inclined plane parallel shear flows. Journal of Heat Transfer, 125:795-803, 2003.
9. G. M. Gershuni, E. M. Zhukhovitsky and A. A. Yakimov. On stability of plane-parallel convective motion due to internal heat sources. International Journal of Heat & Mass Transfer, 17(7):717-726, 1974.
10. G. Houseman. The dependence of convection planform on mode of heating, Nature 332:346-349, 1988.
11. H. Ichikawa, K. Kurita, Y. Yamagishi and T. Yanagisawa. Cell pattern of thermal convection induced by internal heating. Physics of Fluids, 18:038101, 2006.
12. P. H. Roberts. Convection in horizontal layers with internal heat generation. Theory *J. Fluid Mech.* **30**(1):33-49, 1967
13. J. Schmalzl, G. A. Houseman and U. Hansen. Mixing properties of three-dimensional (3-d) stationary convection. Physics of Fluids, 7(5):1027-1033, 1995.

14. G. Schubert, G. A. Glatzmaier and B. Travis. Steady, three-dimensional, internally heated convection. Physics of Fluids, 5(8):1928-1932, 1993.
15. J. Takahashi, Y. Tasaka, Y. Murai, Y. Takeda, T. Yanagisawa. Experimental study of cell pattern formation induced by internal heat sources in a horizontal fluid layer. International Journal of Heat & Mass Transfer, 53(7-8):1483-1490, 2010.
16. Y. Tasaka, Y. Kudoh, Y. Takeda and T. Yanagisawa. Experimental investigation of natural convection induced by internal heat generation. Journal of Physics Conference Series, 14:168-179, 2005.
17. Y. Tasaka and Y. Takeda. Effects of heat source distribution on natural convection induced by internal heating. International Journal of Heat and Mass Transfer, 48:1164-1174, 2005.
18. D. J. Tritton and M. N. Zarraga. Convection in horizontal layers with internal heat generation. Journal of Fluid Mechanics, 30(1):21-31.
19. D. L. Turcotte, J. Schubert, G. Schubert *Geodynamics*, second edition, Cambridge, 2001 Cambridge University Press. – Reported by Takahashi *et al.* [15].
20. M. Tveitereid and E. Palm. Convection due to internal heat sources. Journal of Fluid Mechanics, 76:481-499, 1976.

Proceedings, 5th Chaotic Modeling and Simulation International Conference, 12 – 15 June 2012, Athens Greece

Can the multifractal spectrum be used as a diagnostic tool?

K. P. Harikrishnan[1], R. Misra[2], and G. Ambika

[1] Department of Physics, The Cochin College, Cochin - 682 002, India
(E-mail: *kp_hk2002@yahoo.co.in*)
[2] Inter University Centre for Astronomy and Astrophysics, Pune - 411 007
(E-mail: rmisra@iucaa.ernet.in)
[3] Indian Institute of Science Education and Research, Pune - 411 021, India
(E-mail: g.ambika@iiserpune.ac.in)

Abstract. We seek the possibility of using multifractal spectrum as a diagnostic tool to differentiate between healthy and pathological time series. The data sets used for the analysis consist of EEG and Heart Rate Variability (HRV) time seres downloaded from Physio Bank archives. We use the automated algorithmic scheme recently proposed by us to compute the multifractal spectrum, which provides a set of parameters to compare different data sets. We show that the set of parameters characterising the multifractal spectrum can distinguish between healthy and pathological states in both EEG and HRV.
Keywords: Time Series Analysis, Physiological Chaos, Multifractal Spectrum.

1 Introduction

Recently, many authors [1,2] have stressed the importance of multifractality in the study of heart rate variability and suggested that it could provide a new observational window into the complexity mechanism of heart rate control. The study also highlights the need for evaluating new nonlinear parameters for a better physiologcal investigation and for finding new clinical applications. The main issues regarding the characterisation of complex physiological signals are discussed in a recent review [3].

Out of the large number of studies done on physiological data, the focus has mainly been on the analysis of EEG and ECG time series data, with the purpose of characterisation and prediction from a dynamical systems point of view. The analysis of EEG data from healthy persons and epiletic patients has lead to a better understanding of various aspects of epileptic seizure activities and the corresponding brain states [4,5], but the question of whether the seizure can be predicted in advance is still an open one [6].

There have been a multitude of studies on ECG data sets recorded from healthy persons as well as during some pathological cases, such as, congestive heart disorders and ventricular fibrillation [7–9]. Most of these studies have searched for deterministic nonlinearity in the time series from cardiac system [10,11], and the reliability of these results have also been questioned [12–

14] due to various reasons, such as, insufficient data, presence of noise, the subjective nature of the computational techniques and so on.

In this paper, we present some preliminary results for the analysis of physiological data, by computing the $f(\alpha)$ spectrum from the time series using an automated algorithmic scheme. The details of the scheme are presented and tested in the next section and it is applied to physiological data in §3. The conclusions are drawn in §4.

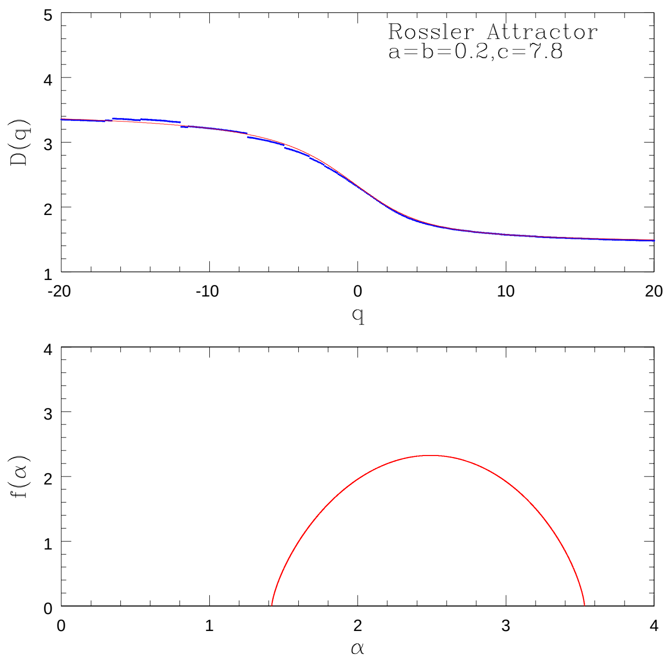

Fig. 1. The D_q spectrum (points) and its best fit curve (continuous line) for the Rossler attractor computed from 10000 data points are shown in the upper panel. The lower panel shows the $f(\alpha)$ spectrum computed from the best fit curve using our scheme.

2 Computing the Multifractal Spectrum

Here we discuss only the salient features of the algorithmic scheme and more mathematical details are presented elsewhere [15,**?**]. The scheme provides us with a set of parameters characterising the spectrum which are good quantifiers to compare the changes in the multifractal character as reflected in the time series.

As the first step, the spectrum of generalised dimensions D_q is computed from the time series using the equation

$$D_q \equiv \frac{1}{q-1} \lim_{R \to 0} \frac{\log\ C_q(R)}{\log\ R} \tag{1}$$

where $C_q(R)$ are the generalised correlation sum. This is done by choosing the scaling region algorithmically as discussed earlier [16]. We make the conditions for R_{max} and R_{min} fixed by the algorithm itself so that the comparison between data sets becomes nonsubjective.

We then use an entirely different algorithmic approach for the computation of the smooth profile of the $f(\alpha)$ spectrum. The $f(\alpha)$ function is a single valued function between α_{max} and α_{min} and also has to satisfy several other conditions, such as, it has a single maximum and $f(\alpha_{max}) = f(\alpha_{min}) = 0$. A simple function that can satisfy all the necessary conditions is

$$f(\alpha) = A(\alpha - \alpha_{min})^{\gamma_1}(\alpha_{max} - \alpha)^{\gamma_2} \tag{2}$$

where A, γ_1, γ_2, α_{min} and α_{max} are a set of parameters characterising a particular $f(\alpha)$ curve. It can be shown [16] that only four of these parameters are independent and any general $f(\alpha)$ curve can be fixed by four independent parameters. Moreover, by imposing the conditions on the $f(\alpha)$ curve, it can also be shown that

$$0 < \gamma_1, \gamma_2 < 1 \tag{3}$$

The scheme first takes $\alpha_1(\equiv D_1), \alpha_{min}(\equiv D_\infty)$ and $\alpha_{max}(\equiv D_{-\infty})$ as input parameters from the computed D_q values and choosing an initial value for γ_1 in the range $[0,1]$, the parameters γ_2 and A are calculated. The $f(\alpha)$ curve is then computed in the range $[\alpha_{min}, \alpha_{max}]$. From this, a smooth D_q versus q curve can be obtained by inverting using the Legendre transformation equations, which is then fitted to the D_q spectrum derived from the time series. The parameter values are changed continuously until the D_q curve matches with the D_q spectrum from the time series and the statistically best fit D_q curve is chosen. From this, the final $f(\alpha)$ curve can be evaluated. An important aspect of the scheme is that it also provides a set of parameters that can completely characterise a given $f(\alpha)$ curve. The parameters can play an important role in the nonsubjective comparison of the multifractal properties of the same system under different conditions, such as, the changes in the chaotic attractor due to parameter variation, changes in the physiological conditions etc.

To illustrate our scheme, we choose the time series from a standard chaotic attractor, namely the Rossler attractor with parameter values $a = 0.2, b = 0.2$ and $c = 7.8$. We use 10000 data points generated with a time step $\Delta t = 0.1$. The D_q spectrum is first computed with embedding dimension $M = 3$, for q values in the range $[-20, +20]$, taking a step width of $\Delta q = 0.1$. Choosing D_{-20}, D_1 and D_{20} as the input values for the $f(\alpha)$ function Eq. (2), the

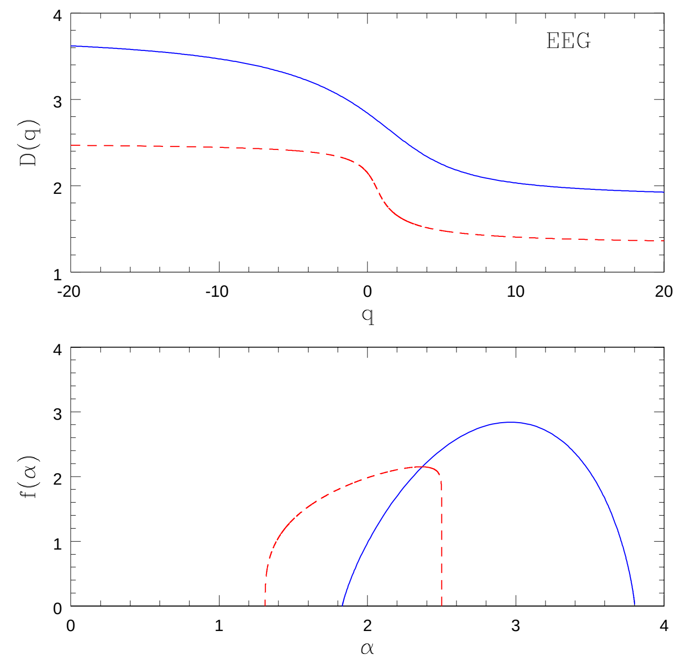

Fig. 2. The top panel shows the D_q spectrum computed using our scheme from representative EEG time series for healthy persons (continuous line) and during epileptic seizure (dashed line). The bottom panel shows the corresponding $f(\alpha)$ spectrum.

parameters γ_1 and γ_2 are scanned in the range $[0, 1]$ and the statistically best fit D_q curve is chosen. The complete $f(\alpha)$ spectrum is then computed from the best fit D_q curve. The D_q spectrum and the best fit D_q curve are shown in Fig. 1 (top panel). The complete $f(\alpha)$ profile computed from the best fit D_q curve is also shown in Fig. 1 (bottom panel).

3 Application to Physiological Data

Physiological systems are, in general, complex where several nonlinearities are involved. We use physiological data commonly used for this kind of analysis, namely, EEG and HRV. In the case of EEG, we analyse signals from normal state and during epileptic seizure. Four data sets each from both cases are used for the analysis. In the case of HRV, we use three catagories of time series. The first one is from normal healthy persons, while the second and third corresponding to different pathological conditions of the heart, namely, congestive heart failure (CHF) and atrial fibrillation (AF). Four data sets for each of the above mentioned classes of HRV are analysed.

The EEG data were downloaded from the website of the Department of Epileptology, University of Bonn while the ECG data were obtained from http://www.physionet.org/physiobank/archives. The EEG data sets consist of continuous data streams of about 24 secs long and with approximately 5000 data points. The HRV data sets for different catagories consist of continuous data streams of approximately 5400 data points with a time step of 0.04 secs. All computations are done for an embedding dimension $M = 3$ and we show results for representative time series from each class.

The D_q and $f(\alpha)$ spectra for the two classes of EEG signals computed by our scheme are shown in Fig. 2. Similarly, the D_q and $f(\alpha)$ spectra for the three different classes of HRV time series are shown in Fig.3 and Fig. 4 respectively. One result which is clear from the figures is that all these signals show multifractal character. Some earlier studies had suggested that there could be a loss of multfractality for HRV in some pathological states [**?**]. But we find that there is only a change in the multifractal character from healthy to pathological states.

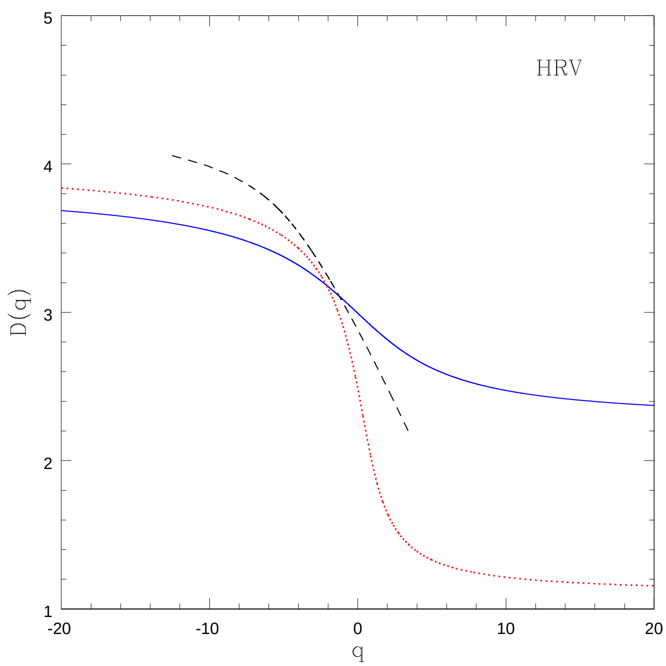

Fig. 3. Typical D_q spectra for HRV signals computed from healthy persons (continuous line), persons with CHF (dotted line) and those with AF (dashed line).

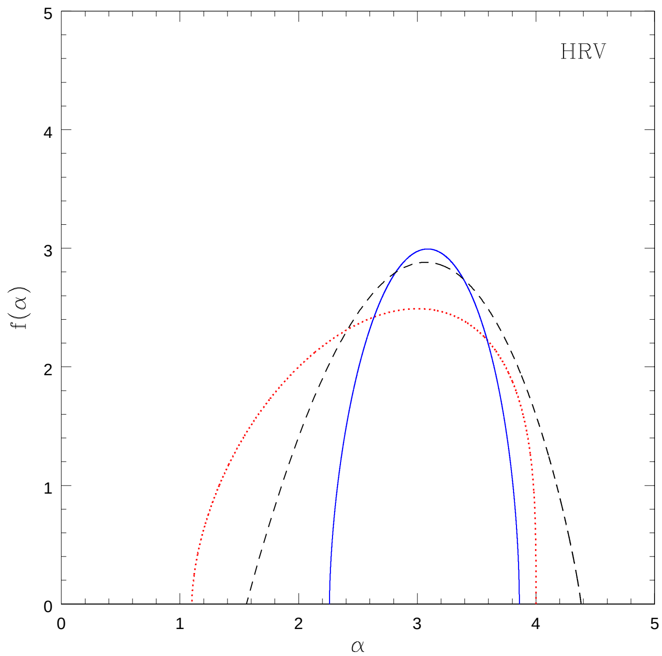

Fig. 4. The $f(\alpha)$ spectrum corresponding to the three cases of HRV signals shown in the previous figure.

Of course, the difference between healthy and pathological time series is evident even visually, with the healthy signals appearing much like random fluctuations and the pathological ones do have some spiky nature. So we expect that these differences are also reflected in their D_q and $f(\alpha)$ spectra. The question is whether these qualitative changes can be quantified using our algorithmic scheme. It is quite evident from the figures that the nature of the $f(\alpha)$ profile is different for healthy and pathological states, in the case of both EEG and HRV. There is significant change in the profile of the spectrum and the parameter values between healthy and pathological states, for both EEG and HRV.

The range of α values, $|\alpha_{max} - \alpha_{min}|$, generally tend to change from healthy to pathological states in all cases. But the changes in the other three parameter values seems to be more significant. The values of γ_1 and γ_2 appear to be more sensitive to the changes in the multifractal character of the time series, especially since the range of γ_1 and γ_2 is limited $(0 < \gamma_1, \gamma_2 < 1)$. For example, for the healthy data sets, the values of γ_1 and γ_2 are very close and always $\gamma_1, \gamma_2 > 0.8$. But in the case of pathological states, their values are generally found to be much less, with the difference $|\gamma_1 - \gamma_2|$ increasing.

This, in turn, increases the asymmetry between the two branches of the $f(\alpha)$ profile.

Thus our results clearly indicates the importance of computing the multi-fractal spectrum using an algorithmic scheme and the utility of the associated parameters in differentiating signals from different physiological conditions. But we have used only limited number of data sets for the analysis. Whether all the trends shown by the parameters as discussed above are genuine and whether they can be used as diagnostic tools from a practical point of view will have to be confirmed by a much more comprehensive data analysis.

4 Conclusion

In this paper, we analyse an ensemble of physiological signals generated from different physiological conditions and try to distinguish them based on their multifractal properties. We use the automated algorithmic scheme recently proposed by us to compute the $f(\alpha)$ spectrum from the time series. The scheme provides a set of parameters to characterise a given $f(\alpha)$ spectrum. The scheme is first tested and illustrated using synthetic time series from standard chaotic systems. It is then applied to two catagories of physiological data, namely, EEG and HRV. The signals from healthy and pathological states in both catagories are analysed. Our analysis indicates that the set of parameters characterising the $f(\alpha)$ spectrum show systematic difference between healthy and pathological states in both catagories. Thus, we find that measures based on multifractal structure can be effectively employed for differentiating signals from healthy and pathological states.

The authors thank the Department of Epileptology, University of Bonn, for making the human brain EEG data available on their website.

KPH and RM acknowledge the financial support from Department of Science and Technology, Govt. of India, through a research grant No. SR/SP/HEP-11/2008.

References

1.R. Sassi, M. G. Signorini and S. Cerutti, *CHAOS*, 19: 028507, 2009.
2.U. Freitas, E. Roulin, Jean-Francois Muir and C. Letellier, *CHAOS*, 19:028505, 2009.
3.L. Glass, *CHAOS*, 19:028501, 2009.
4.N. Pradhan and D. Narayana Dutt, *Comput. Biol. Med.*, 23:425, 1993.
5.W. Latzenberger, H. Preissl and F. Pulvermiller, *Biol. Cybernetics*, 73:477, 1995.
6.M. A. F. Harrison, I. Osorio, M. G. Frei, S. Asuri and Ying-Chang Lai, *CHAOS*, 15:033106, 2005.
7.L. Glass, A. L. Goldberger, M. Courtemanche and A. Shrier, *Proc. R. Soc. Lond. Ser. A*, 413:9, 1987.
8.F. X. Witkowski, K. M. Karnagh, P. A. Penkoske, R. Plonsey, M. L. Spano, W. L. Ditto and D. T. Kaplan, *Phys. Rev. Lett.*, 75:1230, 1995.

9.C. S. Poon and C. K. Merril, *Nature*, 389:492, 1997.
10.F. Ravelli and Anbolin, *Biol. Cybernetics*, 67:57, 1992.
11.R. B. Govindan, K. Narayanan and M. S. Gopinathan, *CHAOS*, 8:495, 1998.
12.L. Glass and P. Hunter, *Physica D*, 43:1, 1990.
13.A. L. Goldberger, *News. Physiol. Sci.*, 6:87, 1991.
14.F. Mitschke and M. Dimming, *Int. J. Bif. Chaos*, 3:693, 1993.
15.K. P. Harikrishnan, R. Misra, G. Ambika and A. K. Kembhavi, *Physica D*, 215:137, 2006.
16.K. P. Harikrishnan, R. Misra, G. Ambika and R. E. Amritkar, *CHAOS*, 19:143129, 2010.

Proceedings, 5th Chaotic Modeling and Simulation International Conference, 12 – 15 June 2012, Athens Greece

Calculation Method of Bifurcation Point for an Impact Oscillator with Periodic Function

Goki Ikeda[1], Kazuyuki Aihara[2] and Takuji Kousaka[1]

[1] Faculty of Engineering, Oita University, 700 Dannoharu, Oita, Japan (E-mail: goki@bifurcation.jp, takuji@oita-u.ac.jp)

[2] Institute of Industrial Science, The University of Tokyo, 7-3-1, Hongo, Bukyo-ku, Tokyo, Japan (E-mail: aihara@sat.t.u-tokyo.ac.jp)

Abstract. We propose a calculation method of the bifurcation point for an impact oscillator with periodic function. First, we show a physical model and explain its dynamics. Next, the Poincaré map is constructed for the following analysis. Furthermore, we specify the derivative of the Poincaré map to calculate the bifurcation point. Finally, we apply the proposed method for a rigid overhead wire-pantograph system and confirm the validity of the method for calculate the bifurcation point in an impact oscillator.

Keywords: Impact oscillator with periodic function, Bifurcation point, Poincaré map, Jacobian matrix, Fixed point.

1 Introduction

The switching system depending on its state and a periodic interval has the interrupted characteristics (we call these systems as interrupted system in this paper). In particular, impact oscillator is the interrupted system; impact oscillator has the characteristics that the solution jumps when the trajectory hits the border. Impact oscillator can be observed in many engineering field. Thus, analyzing the qualitative property of the impact oscillator is a crucial topic from the practical view point.

On the other hand, the impact oscillators have rich compelling phenomena. For instance, bifurcation phenomena can be observed in impact oscillator depending on its complex impact behavior and many researchers have analyzed it since old times, e.g., bifurcation analysis in impact-dampers [1] [2], in spiking neuron model [3] [4], in forest fire model [5], and so on. However, it is difficult to calculate the exact solution in the impact oscillators if the system is high-dimensional or the system has the nonlinear property. For this reason, there are few calculation method for the bifurcation point in the impact oscillator. In the previous work, we have proposed the calculation method for the bifurcation point of the fixed point [6]. Although, it is possible to calculate the bifurcation point for the fixed point in a wide parameter space by solving the characteristic equation iteratively. Hence, we improve previous method in order to calculate the bifurcation point for the fixed point more effectively in this paper. Here, we propose a calculation method of the bifurcation point for an impact oscillator with periodic function.

First of all, we show the two-dimensional differential equation of impact oscillator. Next, we define the function of jump and Poincaré map. Furthermore, we describe the derivative of Poincaré map to solve the characteristic multiplier for the fixed point. In addition, we can calculate the bifurcation point by solving a simultaneous equation of the fixed point and the characteristic equation. Finally, we apply this method for a rigid overhead wire-pantograph system [7] to confirm the validity of the method.

2 Analytical method

2.1 Poincaré map

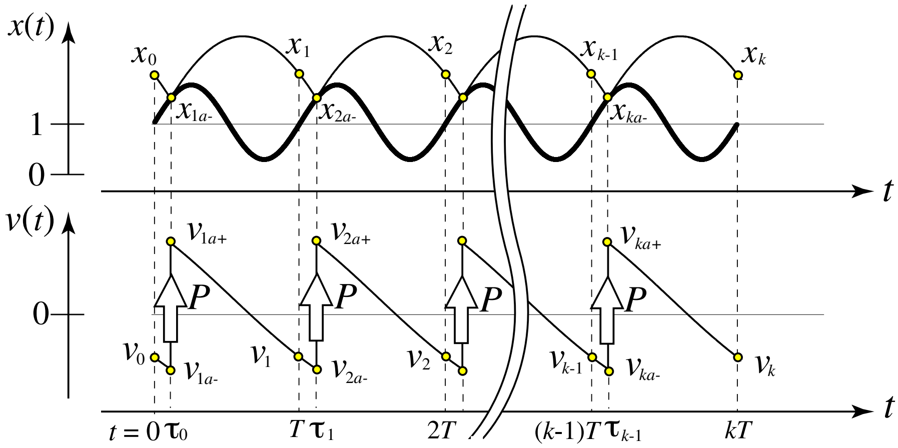

Fig. 1. Two-dimensional impact oscillator.

We consider the impact oscillator shown in Fig. 1. The solutions in Fig. 1 can be described by the following two-dimensional system

$$\begin{cases} \dfrac{dx}{dt} = f(x, v, \boldsymbol{\lambda}) \\ \dfrac{dv}{dt} = g(x, v, \boldsymbol{\lambda}) \end{cases}, \tag{1}$$

where the parameters t, x, v and λ satisfy $t \in \boldsymbol{R}$, $x, v \in \boldsymbol{R}^2$, $f, g : \boldsymbol{R}^2 \to \boldsymbol{R}^2$. Now, Eq. (1) is written as follows:

$$\begin{cases} x(t) = \varphi(t; x_0, v_0, \boldsymbol{\lambda}),\ \ x(0) = x_0 \\ v(t) = \phi(t; x_0, v_0, \boldsymbol{\lambda}),\ \ v(0) = v_0 \end{cases}, \tag{2}$$

where x_0 and v_0 means the initial value at time $t = 0$. Next, we define the following local section $\Pi \in \boldsymbol{R}^2$ by using scalar function q : $\boldsymbol{R}^2 \in \boldsymbol{R}^2$.

$$\Pi = \{x, v \in \boldsymbol{R}^2 : q_0(x, v) = 0, q : \boldsymbol{R}^2 \to \boldsymbol{R}\}, \tag{3}$$

$$q(t + T; x, v) = q(t; x, v). \tag{4}$$

Also, the map P is written by using functions r and s. If x reaches to Π, the solutions are jumped by the map P :

$$\begin{aligned} P : \boldsymbol{R}^2 &\to \boldsymbol{R}^2, \\ \boldsymbol{x}_{1a-} = \begin{bmatrix} x_{1a-} \\ v_{1a-} \end{bmatrix} &= \begin{bmatrix} \varphi(\tau_0; x_0, v_0, \boldsymbol{\lambda}) \\ \phi(\tau_0; x_0, v_0, \boldsymbol{\lambda}) \end{bmatrix} \\ \mapsto \boldsymbol{x}_{1a+} = \begin{bmatrix} x_{1a+} \\ v_{1a+} \end{bmatrix} &= \begin{bmatrix} r(\tau_0; x_0, v_0) \\ s(\tau_0; x_0, v_0) \end{bmatrix} \end{aligned} \tag{5}$$

where τ_0 denotes the time when the solution reaches to Π. The discretized solutions $\boldsymbol{x}_1$ are expressed as

$$\boldsymbol{x}_1 = \begin{bmatrix} x_1 \\ v_1 \end{bmatrix} = \begin{bmatrix} \varphi(T - \tau_0; x_{1a-}, v_{1a+}, \boldsymbol{\lambda}) \\ \phi(T - \tau_0; x_{1a-}, v_{1a+}, \boldsymbol{\lambda}) \end{bmatrix}. \tag{6}$$

Next, we define the maps as follow:

$$\begin{aligned} M_0 : \boldsymbol{R}^2 &\to \Pi_1 & \qquad M_1 : \Pi_0 &\to \boldsymbol{R}^2 \\ \boldsymbol{x}_0 &\mapsto \boldsymbol{x}_{1a-}, & \boldsymbol{x}_{1a+} &\mapsto \boldsymbol{x}_1. \end{aligned} \tag{7}$$

Consequently, the Poincaré map is given by

$$\begin{aligned} M : \boldsymbol{R}^2 &\to \boldsymbol{R}^2 \\ \boldsymbol{x}_0 &\mapsto M_1 \circ P \circ M_0. \end{aligned} \tag{8}$$

In the following analysis, we discuss the derivative of the Poincaré map written as follows:

$$\begin{aligned} DM(\boldsymbol{x}_0, \boldsymbol{v}_0) = \frac{\partial M}{\partial \boldsymbol{x}_0} &= \begin{bmatrix} \dfrac{\partial [1\ 0] M(x_0, v_0)}{\partial x_0} & \dfrac{\partial [1\ 0] M(x_0, v_0)}{\partial v_0} \\ \dfrac{\partial [0\ 1] M(x_0, v_0)}{\partial x_0} & \dfrac{\partial [0\ 1] M(x_0, v_0)}{\partial v_0} \end{bmatrix} \\ &= -\begin{bmatrix} \left.\dfrac{\partial \varphi}{\partial t}\right|_{t=T-\tau_0} \dfrac{\partial \tau_0}{\partial x_0} & \left.\dfrac{\partial \varphi}{\partial t}\right|_{t=T-\tau_0} \dfrac{\partial \tau_0}{\partial v_0} \\ \left.\dfrac{\partial \phi}{\partial t}\right|_{t=T-\tau_0} \dfrac{\partial \tau_0}{\partial x_0} & \left.\dfrac{\partial \phi}{\partial t}\right|_{t=T-\tau_0} \dfrac{\partial \tau_0}{\partial v_0} \end{bmatrix} + \begin{bmatrix} \dfrac{\partial \varphi}{\partial x_{1a-}} & \dfrac{\partial \varphi}{\partial v_{1a-}} \\ \dfrac{\partial \phi}{\partial x_{1a-}} & \dfrac{\partial \phi}{\partial v_{1a-}} \end{bmatrix} \begin{bmatrix} \dfrac{\partial r}{\partial x_0} & \dfrac{\partial r}{\partial v_0} \\ \dfrac{\partial s}{\partial x_0} & \dfrac{\partial s}{\partial v_0} \end{bmatrix}. \end{aligned} \tag{9}$$

Now, derivative of the function P is given by next equation depending on the initial value.

$$\begin{bmatrix} \dfrac{\partial r}{\partial x_0} & \dfrac{\partial r}{\partial v_0} \\ \dfrac{\partial s}{\partial x_0} & \dfrac{\partial s}{\partial v_0} \end{bmatrix} = \begin{bmatrix} \left.\dfrac{\partial r}{\partial t}\right|_{t=\tau_0} \dfrac{\partial \tau_0}{\partial x_0} & \left.\dfrac{\partial r}{\partial t}\right|_{t=\tau_0} \dfrac{\partial \tau_0}{\partial v_0} \\ \left.\dfrac{\partial s}{\partial t}\right|_{t=\tau_0} \dfrac{\partial \tau_0}{\partial x_0} & \left.\dfrac{\partial s}{\partial t}\right|_{t=\tau_0} \dfrac{\partial \tau_0}{\partial v_0} \end{bmatrix} + \begin{bmatrix} \dfrac{\partial x_{1a-}}{\partial x_0} & \dfrac{\partial x_{1a-}}{\partial v_0} \\ \dfrac{\partial v_{1a-}}{\partial x_0} & \dfrac{\partial v_{1a-}}{\partial v_0} \end{bmatrix}. \tag{10}$$

Furthermore,

$$\begin{bmatrix} \dfrac{\partial x_{1a-}}{\partial x_0} & \dfrac{\partial x_{1a-}}{\partial v_0} \\ \dfrac{\partial v_{1a-}}{\partial x_0} & \dfrac{\partial v_{1a-}}{\partial v_0} \end{bmatrix} = \begin{bmatrix} \left.\dfrac{\partial \varphi}{\partial t}\right|_{t=\tau_0} \dfrac{\partial \tau_0}{\partial x_0} & \left.\dfrac{\partial \varphi}{\partial t}\right|_{t=\tau_0} \dfrac{\partial \tau_0}{\partial v_0} \\ \left.\dfrac{\partial \phi}{\partial t}\right|_{t=\tau_0} \dfrac{\partial \tau_0}{\partial x_0} & \left.\dfrac{\partial \phi}{\partial t}\right|_{t=\tau_0} \dfrac{\partial \tau_0}{\partial v_0} \end{bmatrix} + \begin{bmatrix} \dfrac{\partial \varphi}{\partial x_0} & \dfrac{\partial \varphi}{\partial v_0} \\ \dfrac{\partial \phi}{\partial x_0} & \dfrac{\partial \phi}{\partial v_0} \end{bmatrix}. \tag{11}$$

We should remark that the function

$$q(\tau_0(x_0, v_0); x_0, v_0, \boldsymbol{\lambda}) = 0 \tag{12}$$

is differentiable for $\boldsymbol{x}_0$. Hence, $\dfrac{\partial \tau_0}{\partial x_0}$ and $\dfrac{\partial \tau_0}{\partial v_0}$ can be obtained as

$$\frac{\partial \tau_0}{\partial x_0} = \frac{-\left(\dfrac{\partial q}{\partial x}\dfrac{\partial \varphi}{\partial x_0} + \dfrac{\partial q}{\partial v}\dfrac{\partial \phi}{\partial x_0}\right)}{\dfrac{\partial q}{\partial x}\left.\dfrac{\partial \varphi}{\partial t}\right|_{t=\tau_0} + \dfrac{\partial q}{\partial v}\left.\dfrac{\partial \phi}{\partial t}\right|_{t=\tau_0} + \left.\dfrac{\partial q}{\partial t}\right|_{t=\tau_0}}, \tag{13}$$

$$\frac{\partial \tau_0}{\partial v_0} = \frac{-\left(\dfrac{\partial q}{\partial x}\dfrac{\partial \varphi}{\partial x_0} + \dfrac{\partial q}{\partial v}\dfrac{\partial \phi}{\partial x_0}\right)}{\dfrac{\partial q}{\partial x}\left.\dfrac{\partial \varphi}{\partial t}\right|_{t=\tau_0} + \dfrac{\partial q}{\partial v}\left.\dfrac{\partial \phi}{\partial t}\right|_{t=\tau_0} + \left.\dfrac{\partial q}{\partial t}\right|_{t=\tau_0}}. \tag{14}$$

2.2 Derivation method of bifurcation curve

A fixed point of the Poincaré map is given by

$$\boldsymbol{x}_0 - M(\boldsymbol{x}_0) = \begin{bmatrix} x_0 - [1\ 0]\, M(x_0, v_0) \\ v_0 - [0\ 1]\, M(x_0, v_0) \end{bmatrix} = \mathbf{0}. \tag{15}$$

The characteristic equation for the fixed point is expressed

$$\chi(\mu) = \det\left|\mu \boldsymbol{I}_2 - DM(\boldsymbol{x}_0)\right|. \tag{16}$$

Therefore, simultaneous equation is written as

$$F(x, v, \lambda_a) = \begin{bmatrix} x_0 - [1\ 0]\, M(x_0, v_0) \\ v_0 - [0\ 1]\, M(x_0, v_0) \\ \chi(\mu) \end{bmatrix} = \mathbf{0}. \tag{17}$$

Eq. (17) can be calculated for the unknown variables, x_0, v_0, and a bifurcation parameter λ by using Newton's method. Then, the Jacobian matrix of F is

$$DF(\boldsymbol{x}_0, \lambda) = \begin{bmatrix} \dfrac{\partial M}{\partial x_0} - 1 & \dfrac{\partial M}{\partial v_0} & \dfrac{\partial M}{\partial \lambda} \\ \dfrac{\partial M}{\partial x_0} & \dfrac{\partial M}{\partial v_0} - 1 & \dfrac{\partial M}{\partial \lambda} \\ \dfrac{\partial \chi(\mu)}{\partial x_0} & \dfrac{\partial \chi(\mu)}{\partial v_0} & \dfrac{\partial \chi(\mu)}{\partial \lambda} \end{bmatrix}. \tag{18}$$

The characteristic equation and the Poincaré map can be differentiated in a similar way.

3 Example of the application

3.1 A rigid overhead wire-pantograph system

We apply the method to a rigid overhead wire-pantograph system shown in Fig. 2 [7]. The basic element of the pantograph model is composed of a spring, damper and mass, respectively. The mass of the pantograph model impacts the oscillating stopper. The considered model can be described by the following differential equation

$$\begin{cases} \dfrac{dx}{dt} = v \\ \dfrac{dv}{dt} = -x - 2\zeta v \end{cases}, \tag{19}$$

where a damping ratio, the displacement, and the velocity in the pantograph model are expressed in ζ, x, and v. The normalized equation of the overhead wire model is given by

$$S(t) = \varepsilon \sin \Omega t + 1, \tag{20}$$

where the displacement of rigid overhead wire, the amplitude, and the angular frequency are expressed in $S(t)$, ε, and Ω here. When $x(t)$ reaches to $S(t)$, the velocity of mass changes as follows:

$$v_+ = -\alpha v_- + (1 + \alpha)\frac{dS(t)}{dt}. \tag{21}$$

Note that v_+ is the velocity after the impact, and v_- is the previous velocity. Also, α is a coefficient of restitution between the pantograph model and the overhead wire model.

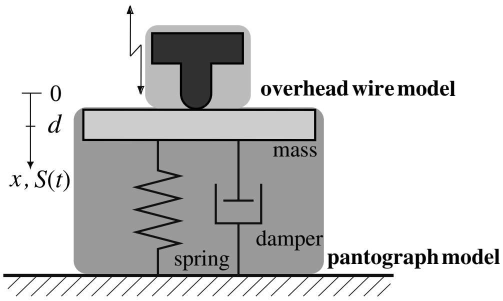

Fig. 2. A rigid overhead wire-pantograph system.

3.2 Application result

Figure 3 shows the numerical results with various Ω. The point in the phase plane of Fig. 3 indicates the periodic solution. By calculating Fig. 3, we can confirm period doubling bifurcation between Ω = 5.64 and Ω = 5.65. Figure 4 shows the one-dimensional bifurcation diagram about x and Ω. Also, we can verify the bifurcation in Fig. 4.

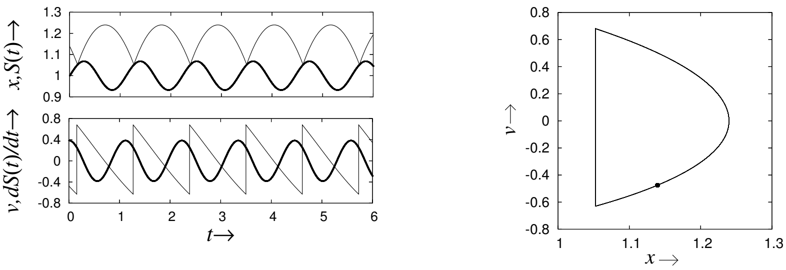

(a) Period-1 solution (Ω = 5.64)

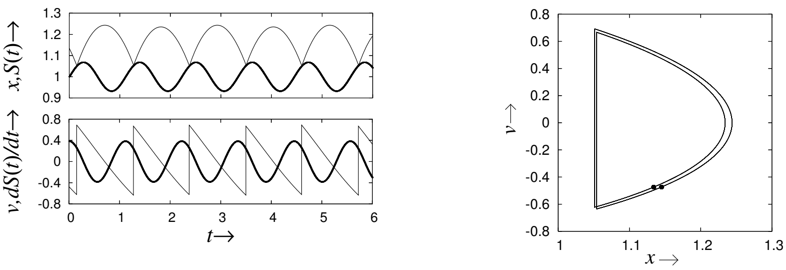

(b) Period-2 solution (Ω = 5.65)

Fig. 3. Solutions and phase plane (α = 0.5, ε = 0.068, ζ = 0.1).

Table 1. Calculation of the fixed point and characteristic multiplier with Ω (α = 0.5, ε = 0.068, ζ = 0.1).

Ω	μ_1	μ_2	x	v	Remarks
5.64000	-0.20420	-0.97974	1.13916	-0.47575	Stable
5.64400	-0.20246	-0.98832	1.13920	-0.47511	Stable
5.64800	-0.20076	-0.99687	1.13923	-0.47446	Stable
⋮	⋮	⋮	⋮	⋮	⋮
5.64947	-0.20014	-1.00000	1.13925	-0.47422	Period-doubling bifurcation
⋮	⋮	⋮	⋮	⋮	⋮
5.65000	-0.19992	-1.00114	1.13925	-0.47414	Unstable

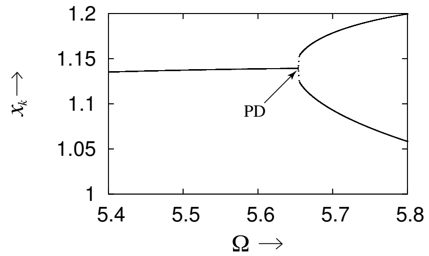

Fig. 4. One-dimensional bifurcation diagram (α = 0.5, ε = 0.068, ζ = 0.1).

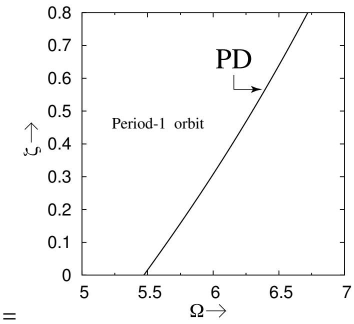

Fig. 5. Two-dimensional bifurcation diagram (α = 0.5, ε = 0.068).

Table. 1 shows the fixed point and the characteristic multiplier. This table can be calculated by solving Eq. (15), (16). The fixed point exists stable until Ω = 5.64950. After this value, the fixed point become unstable because of period-doubling bifurcation. Next, Figure 5 shows the two-dimensional bifurcation diagram for various of Ω and ζ. In this figure, the curve indicates the bifurcation point of period-doubling bifurcation from period-1 solution to period-2 solution. We found this curve by calculating Eq. (17). Therefore, the method can effectively obtain the region of the bifurcation point of period-1 solution.

4 Conclusion

In this paper, we have proposed a calculation method of the bifurcation point for an impact oscillator with periodic function. First, we defined the Poincaré map and showed the derivative of the map. Next, we expressed the fixed point and the characteristic equation by using the Poincaré map and its derivative. Finally, we applied this method for a rigid overhead wire-pantograph system, and we could confirm the validity of this method. The future work is establishment of the method which is capable of adapting various subharmonic solution.

Acknowledgment

This research is partially supported by the Aihara Innovative Mathematical Modelling Project, the Japan Society for the Promotion of Science (JSPS) through the "Funding Program for World-Leading Innovative R&D on Science and Technology (FIRST Program)," initiated by the Council for Science and Technology Policy (CSTP).

References

1. Barbara Blazejczyk-Okolewska. Analysis of an impact damper of vibrations. *Chaos, Solitons and Fractals*, Vol. 12, No. 11, pp. 1983–1988, 2000.
2. J. Park, S. Wang, and M. J. Crocker. Mass loaded resonance of a single unit impact damper caused by impacts and the resulting kinetic energy influx. *Journal of Sound and Vibration*, Vol. 323, No. 3-5, pp. 877–895, 2009.
3. Y. D. Sato and M. Shiino. Generalization of coupled spiking models and effects of the width of an action potential on synchronization phenomena. *Phys. Rev. E*, Vol. 75, 011909, 2007.
4. E. M. Izhikevich. Simple model of spiking neurons. *IEEE Trans. Neural Netw.* , Vol. 14, No. 6, pp. 1569–1572, 2003.
5. S. Maggi and S. Rinaldi. A second-order impact model for forest fire regimes. *Theoretical Population Biology*, Vol. 70, No. 2, pp. 174–182, 2006.
6. S. Hirashima, S. Karube and T. Kousaka. Numerical Calculation Method of Characteristic Multiplier for the Fixed Point in a Rigid Overhead Wire-Pantograph System. *Proc. NOLTA2010*, pp. 249-252, 2010.
7. S. Kawamura, K. Kitajo, S. Horita and M. Yoshizawa. Fundamental Study on Impact Oscillations of Rigid Trolley-Pantograph System. *The Japan Society of Mechanical Engineers, Series C*, Vol. 73, No. 728, pp. 974–981, 2007(In Japanese).

Proceedings, 5th Chaotic Modeling and Simulation International
Conference, 12 – 15 June 2012, Athens Greece

Chaos and its regularization in the stellar wind

Alexander F. Kholtygin[1]

Astronomical Institute, Saint-Petersburg University, 198504, Universitetskii pr., 28, Russia
(E-mail: afkholtygin@gmail.com)

Abstract. It is well known that the power stellar wind of OB and Wolf-Rayet (WR) stars consist of the numerous dense inhomogenuities (clumps) and more rarefied homogeneous interclump medium. Clumps are randomly distributed in the whole volume of stellar wind and have arbitrary sizes and fluxes. Formation of the clumps appears to be the chaotic process connected with internal instability of the radiation dominated stellar wind. Our modelling of the line profiles in spectra of OB and WR stars with clumped wind show that initially chaotic ensemble of the clumps can be regularized. As a result of that regularization the clusters of clumps which manifest themselves as strong bumps on the line profiles cam be developed.
Keywords: chaos, stellar wind, clumps, regularization.

1 Introduction

Twenty-first-century theoretical physics is coming out of the chaos revolution [2]. Astrophysics, as a part of physics is also a field for an application of the chaos theory [21].

Chaotic structures can be found in the Solar System [5], in the arrays of orbits of exoplanets [18] and in the atmospheres of the late-types AGB and post-AGB stars [6,7].

Atmospheres of early-type stars quite a long time were considered as homogeneous spherically symmetric flows [13]. In the beginning of 80th the first indications of the presence of high density regions (blobs or clumps) in the atmospheres (winds) of the early-type (hot) stars both from the theory and the observations were revealed [1,4].

This inhomogeneous wind were described in the *clump model* [1]. In this model a stellar wind is proposed to be composed of the numerous dense clumps and low density interclump medium. Total number of the clumps can exceeds 10^3. The ions of the low and moderate ionization stages are located dominantly in the clumps while the interclump medium seems to be strongly ionized.

A separate clump forms a small detail in the line profiles in the spectrum of early-type stars. All ensembles of the clumps in the winds of these stars form a stochastic line profile variability (LPV) in the stellar spectra. A stochastic character of the LPV allows us to conclude that clumps born and dissipate chaotically. A chaotic ensemble of clumps in the atmosphere may be described in the framework of the Stochastic clump model proposed by Kostenko & Kholtyhin [11] and Kudryashova & Kholtygin [12] and close to the model of discrete wind emission elements proposed by Lepine & Moffat [14].

Spectral observations of Wolf-Rayet (WR) and OB stars show that together with dissipative processes in the stellar atmospheres resulting in a chaotization of the stellar wind and a formation a stochastic wind structure, some kinds of a regularization processes leading to the formation of quasi-regular structures in the wind can be also effective. In the present paper we consider these evidences of the wind regularizations.

2 Chaos in stellar wind: stochastic clump ensemble

In our stochastic clump model [11,12] we suppose that there is no way to know where in the wind, when and how the next clump can appear. Ith means that one can only say about the probability for clump to born in the fixed wind volume and has a determined values of the mass, size, fluxes in the lines and other parameters. For each clump these values are defined through the distribution function $N_{\rm cl}(M_{\rm cl}, R_{\rm cl}, \theta, \varphi)$ of clumps on masses $M_{\rm cl}$, sizes $R_{\rm cl}$ and other parameters. Here $M_{\rm cl}$ is a mass of the clump, $R_{\rm cl}$ is its radius, θ is an angle between the direction of the clump motion and line of sight and φ is an azimuthal angle of the clump in the coordinate system where the origin of coordinates is located in the center of star and the Z-axis coincides withy the line of sight.

The total flux in the line formed by a clumped atmosphere in a frequency interval $[\nu, \nu + d\nu$ can be presented as

$$F(\nu)\nu = F^{\rm icl}(\nu)\nu + F^{\rm cl}(\nu)\nu + F^{\rm cl-icl}(\nu)\nu\,. \tag{1}$$

Here the value of $F^{\rm icl}(\nu)$ is the part of the line flux formed by the homogeneous interclump medium only, $F^{\rm cl}(\nu)$ is the clumps contribution and $F^{\rm cl-icl}(\nu)$ refers to the contribution of the clump - interclump medium interactions to the line profile.

Due to of the large velocity gradients in the stellar wind the contributions of the separate clumps into the total line flux can be considered independently and a part of the total line flux formed by clumps

$$F^{\rm cl}(\nu) = \sum_i F^i_\nu = \int_{(4\pi)} \int_{M_{\rm min}}^{M_{\rm max}} \int_{R_*}^{R_{\rm wind}} N_{\rm cl}(M_{\rm cl}, R_{\rm cl}, \theta, \varphi) F^i_{\rm cl}(\nu)\, d\Omega\, dM_{\rm cl}\, dR_{\rm cl}\,, \tag{2}$$

where $M_{\rm min}$ and $M_{\rm max}$ are the minimal and maximal masses of the clumps in the ensemble. A function $F^i_{\rm cl}(\nu)d$ describes a flux, which a clump with a number i emits in the frequency interval $[\nu, \nu + d\nu]$ in the solid angle $d\Omega = 2\pi sin\theta\, d\theta\, d\varphi$. R_* is a stellar radius and $R_{\rm wind}$ is the wind radius.

As it was shown by Kostenko & Kholtygin [11] the contribution of the interclump medium into the total intensity of most of the lines in the early-type star spectra (e.g. lines of ions CIII, HeI-II, etc.) is small. The interaction of clumps with the interclump medium gives contribution mainly in the X-ray region and weakly impacts on the profiles of optical and UV lines considered. It means that the intensity of these lines are mainly determined by chaotic clumps in the wind.

Studies of LPV for O and WR stars (Kaper et al. [15], Lépine & Moffat [14]) specify that clumps are mainly formed in a narrow area of an atmosphere near the stellar core. It means that distribution of clumps on distances from the stellar core, masses and directions can be considered independently:

$$N_{\rm cl}(M_{\rm cl}, R_{\rm cl}, \Omega) = N_m(M_{\rm cl})\, N_r(R_{\rm cl})\, N_{\rm cl}(\Omega). \tag{3}$$

Early-type stars are the powerful sources of X-Ray emission (e.g., Oskinova et al. [20]). For explanation both the UV optical an X-Ray spectra of these stars Kholtygin at al. [8] propose the *3-phase model* of the early-type star winds. In this model is supposed that wind can be in 3 phase states: homogeneous warm wind with a mean temperature $\approx 10^5\,K$, cold clumps with $T \approx 10^4\,K$ and hot clumps (hot zones with a temperature T up to 10^8 K. Warm wind and cold clumps emit in an optical and UV range, whereas a radiation of hot zones are mainly in a X-Ray region.

For WR stars clumps give the *main contribution* in the line emission, but for OB stars clumps give the smaller one. There exist a phase transitions between hot and cold phases. Cold clumps can be heated by shocks up to 10^8 K (Bychkov & Aleksandrova [3]), whereas hot zones cool very fast with cooling time is less than 1 min and the hot clumps became th cold clumps again soon after their heating. The agreement of the characteristic times of optical and X-Ray variability supports the *3-phase model* (see Oskinova et al. [19] and reference therein for details).

3 Modelling the clump ensemble

To model the chaotic distribution of clumps in the stellar winds we need to know the distributions $N_m(M_{\rm cl})$, $N_r(R_{\rm cl})$ and $N_{\rm cl}(\Omega)$.

We present a distribution of clumps on masses in atmospheres of early-type stars as $N_m(M_{\rm cl}) \sim (M_{\rm cl})^{-\gamma}$ and adopt the values of $\gamma \approx 2.0$ (see arguments presented by Kudryashova & Kholtygin [12]).

For modelling the distribution $N_r(R_{\rm cl})$ we suppose that clumps are born randomly near the stellar core, the total clump number in the atmosphere is constant and their distribution on radius R is determined by a relation $R^2 N_r(R)(R) V_{\rm cl}(R) = const$. For a dependence of the clump velocity $V_{\rm cl}(R)$ on the distance R from the center of star we adopt standard β-law:

$$V_{\rm cl}(R) = V_0^{\rm cl} + (V_\infty^{\rm cl} - V_0^{\rm cl}) \left(1 - \frac{R_*}{R}\right)^{\beta} . \tag{4}$$

Here $V_0^{\rm cl}$ is the formal clump velocity at a level $R = R_*$, $V_\infty^{\rm cl}$ is the terminal clump velocity at $R \gg R_*$, and a typical value of a parameter $\beta = 0.5 - 1$.

We use mainly the spherical-symmetric distribution $N_{\Omega}(\Omega)$ of directions of clumps.

We assume that each clump forms a detail of the line profile (subpeak) with gauss distribution of intensity. Dependencies of a total flux in the different lines formed by separate clump at the distance R to star were calculated by Kostenko & Kholtygin [11]. As in a paper by Lépine ([16]) we suppose that the full fluxes of subpeaks $F_i \propto \sigma_i^2$, where σ_i^2 is a velocity dispersion inside a clump with number i.

Follow Kudryashova & Kholtygin [12] we suppose that mean clump *lifetime* is determined via a relation

$$T^{\rm cl} = T_{\rm cl}^{\rm max}\,(F_{\rm cl}^{\rm max}/F_{\rm cl})^{\gamma}\,, \qquad (5)$$

where $T_{\rm cl}^{\rm max}$ is a *lifetime* of a clump wich have a maximal flux $F_{\rm cl}^{\rm max}$of the considered line and $\gamma \approx 1$ (see Lépine [16] for details. The *lifetime* of a clump is an interval between two moments of times. The first one is a moment when a clump is formed an emit in the line. The second is a moment when the clump can exists by does not emit in the considered line. It means that in a common case the *lifetime* of clump depends of the line whic we consider.

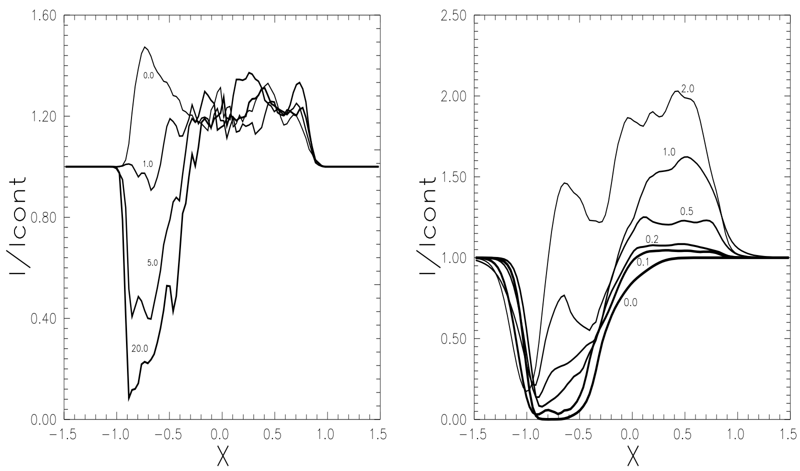

Fig. 1. Left panel: a typical mean line profiles in a dependence on $\tau_{\rm cl}^{\rm max}$ = 0.0, 1.0, 5.0 and 20.0 and for $\zeta = 0.5$. **Right panel**: the same as in the left panel, but for a value of the parametr $\zeta = 0.0$, $0.1\,0.2\,0.5, 1.0$ and 2.0 for $\tau_{\rm cl}^{\rm max}$=10.

The resonance lines of ions of the most elements in the atmospheres of the early-type stars have the strong absorption components. This absorption can appear when a large clump is on the line of sight and screen the emission of the stellar core. We use the next procedure to take into account the absorption of the stellar emission by clumps. Suppose that there are a number of clumps which on the line of sight can absorb the radiation of the stellar photosphere and the and a total optical depth for absorption of the continuum radiation can be presented as a sum of all optical depths of all such clumps.

To calculate an optical depth $\tau_i(\nu)$ of a clump with a number i in the central frequency of the line we use the scaled relations

$$\tau_i(0) = \tau_{\rm cl}^{\rm max}(F_i/F_{\rm max})^{\mu_\tau},$$

where $\tau_{\rm cl}^{\rm max}$ is an optical depth of a clump with a maximal line flux $F_{\rm max}$. From calculations by Kostenko & Kholtygin [11] of the ionization structure of the early-type stars we conclude that parameter $\mu_\tau \approx 2$.

4 Line profile calculations for the clumped wind

For the sake of the simplicity hereinafter will plot the calculated line profile in the dimensionless frequencies

$$x = (\nu - \nu_0)/\Delta\nu_\infty\,, \tag{6}$$

where $\Delta\nu_\infty = \nu_0(V_\infty/c)$ is the total line width, c is the light velocity, ν_0 is the central frequency of the line.

It should me mention that the relation (2) gives us the *instantaneous* line profile only, whereas the observed line profiles are the mean of all instantaneous profiles over the whole interval of the observations. For evaluating the *quasi-observed* line profile we average all *instantaneous* line profiles over the typical time of observations of one line profile ΔT. The typical values of $\Delta T = 10 - 30\,\mathrm{min}$.

Main parameters of the stochastic model are σ_{max}, a velocity dispersion in a clump with a maximal flux, ε, a ratio of a minimal and a maximal fluxes of line formed by an ensemble of clumps and τ_{cl}^{max}, the optical depth of a clump with the maximal flux. To normalize the line profile at the level of the continuum we introduce a parameter $\zeta = F_{\rm line}/F_{\rm cont}$, where $F_{\rm line}$ is the total flux emiited in the emission component of the line and $F_{\rm cont}$ is the flux in the continuum within the frequencies of the line.

For example we plot a dependence of mean model line profile versus $T_{\rm cl}^{\rm max}$ in Fig. 1 for a resonance doublet CIV λ 1548,1550.

The LPV can be clearly seen in the case of using the difference line profiles (individual profiles minus mean line profile). For obtaining the difference model profile we calculate the averaged *quasi-observed* line profiles over the whole period of observation $T_{\rm obs}$. For an illustration we plot the typical difference line profiles in the stochastic clump model in Fig. 2. The dashed lines show the displacement of subpeaks on the line profiles from the center to the wings of the line.

This displacement reflects the acceleration of the clumps in the wind and can be seen in Fig. 3 where we plot the dynamical spectra for line CIV λ 1548,1550 LPV for typical parameters of a clump ensemble at a total duration $T^{\rm full} = 10^h$ of *quasi-observations*.

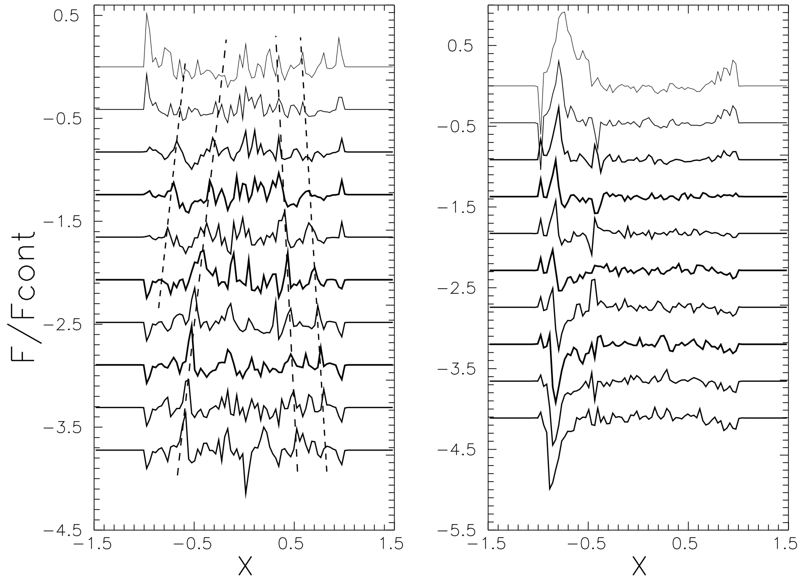

Fig. 2. Left panel: difference line profiles for the pure emission line ($\tau_{\max} = 0$) for the stochastic clump model with parameters $\varepsilon = 10^{-5}$ and $\sigma_{\max} = 0.20$.The time interval between the successive profiles is 30 min. **Right panel**: the same as in the left panel but for opaque clumps with $\tau_{\max} = 25$.

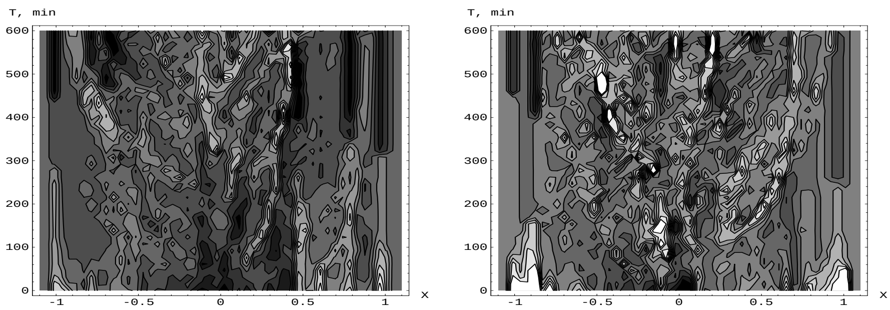

Fig. 3. Left panel: dynamical spectra in the Stochastic Clump Model for parameters $\sigma_{max} = 0.20$, $\varepsilon = 10^{-3}$ and a parameter $\tau_{\rm cl}^{\max} = 0$ and for 10^h of total time of "quasi-observations". **Right panel**: the sam as in the left panel, but for $\tau_{\rm cl}^{\max} = 0$.

5 Using wavelets for testing clumps

For OB stars the clump contribution, connected with small-scale structures in the stellar wind, in the total line profile variations is not so significant as for WR ones. For this stars the share of the regular variations of the line profiles, connected with the large-scale structures in the stellar wind, is significant. It means that we have to use the more effective methods for testing a clump contribution in the LPV.

The most convenient tool for a decomposition the clump contribution in the LPV is the wavelet analysis. The wavelet transform of the analyzed function $f(x)$ (in our case it is a difference line profile) is

$$W(s,u) = \frac{1}{s}\int\limits_{-\infty}^{\infty} f(x)\psi\left(\frac{x-u}{s}\right)dx \;=\; \int\limits_{-\infty}^{\infty} f(x)\,\psi_{su}(x)dx\,. \tag{7}$$

where $\psi(x)$ is the mother wavelet, s is a scale. In our case the most suitable is the so-called MHAT wavelet $\psi(x)$=$(1-x^2)\exp(-x^2/2)$, which has a narrow energy spectrum. The MHAT wavelet is proportional to the second derivative of a Gaussian and can be used to select the gauss-like features in the differential line profiles.

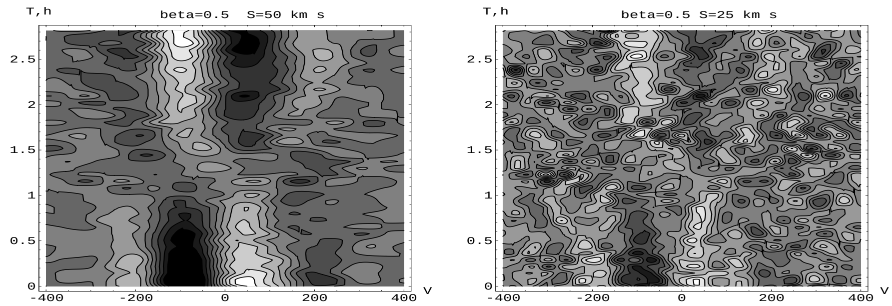

Fig. 4. Left panel: dynamical wavelet spectra for line HeII $\lambda\,4686$ in a spectra of star δ Ori A for the scale $S = 50$ km/s. **Rightt panel**: the same as in the left panel, but for $S = 25$ km/s

Kholtygin et al. ([9]) described a obtaining the *dynamical wavelet spectra* for lines in spectra of early-type stars. Those spectra are the wavelet transform of the difference spectra for the analyzed line in the velocity V space in a dependence of the time of observation t and for the fixed scale s. In this case, the scale variable s is expressed in km/s.

In Fig. 4 we plot the dynamical wavelet spectra for line HeII $\lambda\,4686$ in spectra of O star δ Ori A for the scales $S = 50$ and 25 km/s. Details of our observations are described by Kholtygin et al. [9]).

For small scales in an interval $S = 1 - 5$ km/s the dynamical wavelet spectra is determined by the noise contribution mainly and do not plot in the Fig. 4. In the same time for large scale $S = 50$ km/s mainly regular variations in the *dynamical wavelet spectra* can be detected, as it can be seen in Fig. 4 (left panel). For intermediate values of the scales S we can detect in the dynamical wavelet spectra both the stochastic variations connected with clumps and regular variations induced by the large scale structures. Both types of variations are seen in Fig. 4 (right panel).

6 Regularization of the chaotic clump ensemble

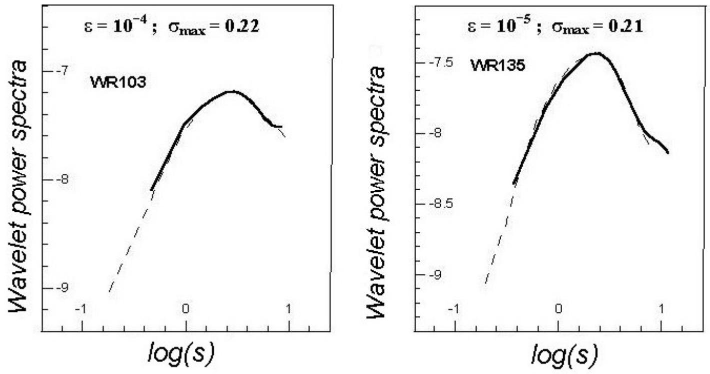

Fig. 5. Left panel: mean wavelet power spectra for lines CIII λ 5696 and HeII λ 5511 in a spectra of star WR 103 as a function of a scale S (solid line) in a comparison with wavelet power spectra for mean model profiles of these lines (dashed lines). **Right panel**: the same as in the left panel, but for WR 135.

To study what is a real structure of the clumps in the wind of early-type stars we compare the wavelet power spectra of the difference line profile in the spectra of selected WR stars with calculated for model profiles in the stichastic clump model. The methodic how to calculate the wavelet power spectra is described by Kudryashova and Kholtygin [12] and by Kholtygin [10].

The wavelet power spectra for 8 WR stars were taken from a paper by Lépine et al. [17]. The quality of the fit of the model and obtained from the real line profiles wavelet power spectra is good as it can be see in Fig. 5.

Table 1. Parameters of the clump ensembles for selected WR stars

Star	Sp. Class	ζ	V_∞(km/s)	ε	$\sigma_{\max}$
WR 103	WC9	17.0	1190	10^{-4}	0.22
WR 111	WC5	1.7	2415	10^{-5}	0.25
WR 134	WN6	2.0	1905	10^{-3}	0.20
WR 135	WC8	10.0	1405	10^{-5}	0.21
WR 136	WN6	2.3	1605	10^{-5}	0.20
WR 137	WC7+OB	2.5	2550	10^{-5}	0.22
WR 138	WN5+OB	0.4	1345	10^{-5}	0.23
WR 140	WC7+O4-5	1.25	2900	10^{-4}	0.035

The parameters of the stochastic clump model which provide the best fit are presented in the Table 1. It should be mention that the values of $\sigma_{\max}$ for all WR stars excluding the binary system WR 140 are very close. It means that the parameters of the clump ensembles and their structure are also close.

The velocity dispersion $\sigma_{\rm max}$ in the clumps are rather large as it can be sin from the Table 1. For typical for WR stars terminal velocities $v_\infty = 1500 - 2000$ km/s the value of $\sigma_{\rm max}$=200-600 km/s for clumps with the maximal fluxes in the considered line. The sizes of such clumps can be as large as $4R_*$ as it follows from the simple estimations.

It may be concluded that the detai;ls of the line profiles with very large velocity dispersion can not be formed by a separate clump but by cluster of the smaller clumps with close values of the radial velocities and probably with close locations in the wind. It means, in turn, that the initially chaotic ensemble of the clumps can be regularized and the regular structure of clumps can appear.

7 Conclusion

From an analysis the structure of winds of the early-type stars we can conclude:

1. The line profiles in spectra of early-type stars and their variations can be descibed in the *stochastic clump model*.

2. The initially stochastic clump ensemble does not remain totally chaotic. The large cluster of clumps which forms the large details of the line profiles are formed in the wind.

Acknowledgements. The author is grateful for the support provided by a Saint-Petersburg University project 6.38.73.2011.

References

1.I. I. Antokhin, A. F. Kholtygin, A. M. Cherepashchuk. Ionization State and Possible Floccular Structure of the Atmospheres of Wolf-Rayet Stars. *Soviet Astronomy*, 32:285-290, 1988.

2.M. Baranger. Chaos, Complexity, and Entropy A physics talk for non-physicists. MITCTP-3112, http://necsi.org/projects/baranger/cce.pdf

3.K.V. Bychkov, O.A. Aleksandrova. The Probable Role of Cloudy Wind Structure in the X-ray Emission of the Binary HD 193793. *Astronomy Reports*, 44:781–789, 2000.

4.A. M. Cherepashchuk, Kh. F. Khaliullin, J. A. Eaton. Ultraviolet photometry from the Orbiting Astronomical Observatory. XXXIX - The structure of the eclipsing Wolf-Rayet binary V444 Cygni as derived from light curves between 2460 A and 3. 5 microns. *Astrophysical Journal*, 281:774-788, 1984.

5.R. Greenberg, G. V. Hoppa, B. R. Tufts, P. Geissler, J. Riley. Chaos on Europa. *Icarus*, 141:263286, 1999.

6.V. Icke. Quasiperiodicity and chaos in post-AGB stars. In C. Sterken, editor *Interplay of Periodic, Cyclic and Stochastic Variability in Selected Areas of the H-R Diagram*, ASP Conf. Ser. 292:357, 2003.

7. M. J. Ireland. Extended Atmospheres of AGB Stars: Modeling and Measurement. In F. Kerschbaum, T. Lebzelter, R.F. Wing, editors, *Why Galaxies Care about AGB Stars II: Shining Examples and Common Inhabitants*, Proc. Conf. held at University Campus, Viena, Austria, 16-20 August 2010. San Francisco: Astronomical Society of the Pacific, 2011., p.83
8. A.F. Kholtygin, J.C. Brown, J.P. Cassinelli et al. Structure and variability of hot star winds. *Astron. Astroph. Trans.*, 22:499-512, 2003.
9. A. F. Kholtygin, T. E. Burlakova, S. N. Fabrika, G. G. Valyavin, M. V. Yushkin. Microvariability of line profiles in the spectrum of OB stars III: supergiant δ Ori A. *Astronomy Reports*, 50:887-901 2006.
10. A. F. Kholtygin. Modelling the induced clumping stochastic line profile variability. In W.-R. Hamann, A. Feldmeier, L.M. Oskinova, editors, *Clumping in hot-star winds* Proc. of an international workshop held in Potsdam, Germany, 18- 22. June 2007.
11. F. V. Kostenko, A. F. Kholtygin. Ionization structure of the atmospheres and line profiles in the spectra of Wolf-Rayet stars. *Astrophysics*, 41:280–299, 1999.
12. N. A. Kudryashova, A. F. Kholtygin. Modeling of Rapid Variability in the Spectral Line Profiles of Wolf-Rayet Stars, *Astronomy Reports*, 45:287–293, 2001.
13. N. Langer. Standard models of Wolf-Rayet stars. *Astronomy and Astrophysics*, 210:93-113, 1989.
14. S. Lépine, A. F. J. Moffat. Wind Inhomogeneities in Wolf-Rayet Stars. II. Investigation of Emission-Line Profile Variations. *Astrophysical Journal*, 514:909–931, 1999.
15. L. Kaper, H. F. Henrichs, J. S. Nichols. Long- and short-term variability in O-star winds. II. Quantitative analysis of DAC behaviour. *Astronomy and Astrophysics*, 344:231–262, 1999.
16. S. Lepine. Wavelet analysis of Wolf-Rayet emission line variability: Evidence for clumping. *Astrophysics and Space Science*, 221:371–382, 1994.
17. S. Lépine, A. F.J. Moffat, R. N. Henriksen. Wind Inhomogeneities in Wolf-Rayet Stars. I. Search for Scaling Laws Using Wavelet Transforms. *Astrophysical Journal*, 466:392-403, 1996.
18. V. Makarov. Stability, chaos and entrapment of stars in very wide pairs. *Monthly Notices of the Royal Astronomical Society*, 421:L11-L13, 2012.
19. L.M. Oskinova, D. Clarke, A. M. T. Pollock. Rotationally modulated X-ray emission from the single O star ζ Ophiuchi *Astronomy and Astrophysics*, 378:L21–L24, 2001.
20. L.M. Oskinova, A. Feldmeier, W.-R. Hamann. High-resolution X-ray spectroscopy of bright O-type stars. *Monthly Notices of the Royal Astronomical Society*, 372:313–326, 2006.
21. O. Regev. Chaos and Complexity in Astrophysics. Cambridge University Press, 2006.

Synergistic approach to amphibian aircraft nonlinear adaptive regulator design: Harmonic disturbance observers

Prof. Kolesnikov A.A.*, PhD. Nguyen Phuong**

* Tagangog Technological University, Southern Federal University, Russia
E-mail: anatoly.kolesnikov@gmail.com
** University of Technical Education, Hochiminh City, Vietnam
E-mail: phuongn@fit.hcmute.edu.vn

Abstract: Aircraft amphibian (SA), as a control object, has an extremely complex structure consisting of a set of subsystems including exchange processes of force, energy, matter and information. This control object operates in the complex environments as atmosphere as well as adjoining surface of water and air.
The problem is to design a regulator that to control the flight modes with impact on the surrounding environment. Requirement to designed regulator is quick responsibility to adapt to the impact of chaotic disturbances of environments. In this report we consider a method synthesis nonlinear control system of aircraft amphibian motion with state observers of harmonic disturbances based on synergetic approach in modern control theory
Keywords: Synergistic, system's synthesis, regulator design, chaotic disturbances, aircraft amphibian, nonlinear dynamic modeling.

1. Introduction

The solution of the various control tasks based on using of a control object state vector. In real conditions of full state vector measurement for one reason or another is not feasible. For this purpose, the control system introduces a subsystem of state estimation - a state observer.
For linear systems, it is distinguished full-order state observers (Kalman Observer), which have a dimension of the state vector as same as that of the control object, reduced order observers (Luenbergera Observer) and observers of increased order (adaptive observers) [1, 2]
Proposed in this article, the nonlinear observer can be referring to the reduced order observers. Even more challenging is a problem of estimating the unmeasured external disturbances. The basic idea of perturbation estimation is as follows: To construct a model of external influences, which is in the form of a homogeneous differential equation system with known coefficients and unknown initial conditions. The model is combined with the perturbation model and with this received enhanced system observer is constructed. Obtained with it estimates include the estimates of object state variables, and evaluation of external influences.
The asymptotic observer design methods are applicable for a wide class of nonlinear systems proposed in [3, 4, 5]. In this work, a new version of an amphibian control methods and problems, which are solved by the dynamic synergistic regulators to such observers, is described. These observers have

carried out a unmeasured harmonic external disturbance evaluation effecting on the amphibian. The nonlinear external perturbation observers (NEPO) consist of a monitoring contour and a control circuit that operates in parallel.

2. The Problem Statement

Suppose that the control object's behavior and an external disturbances effecting on it could be described by the differential equations system:

$$\dot{x} = g(x, z, u);$$
$$\dot{z} = h(x, z, u).$$

Where n vector x и m vector z – components of state vector; u – a control vector; $g(.)$ и $h(.)$ – continuous nonlinear functions. Vector x is assumed observable, and vector z – unobservable.

Then the observer synthesis problem can be formulated as follows. Need to synthesize NEPO with form:

$$\dot{w}(t) = R(x, w);$$
$$\hat{z}(t) = K(x, w),$$

where w – observer state vector; $\hat{z}$ – unmeasured external disturbances evaluation vector.

In this case, NEPO must provide:

- a closed system asymptotic stability;
- stabilization of the pitch angle, altitude and flight speed;
- assessment of unobserved external perturbations;
- compensation of external disturbances.

The NEPO synthesis procedure is divided into three stages:

a) Synthesis of control laws u_i to ensure implementation of the required technological problem (in this case assume that all control object state variables are observable);
b) Synthesis of an observer for the unobservable state variables and unmeasured disturbances.
c) Replacement of unobservable variables in the synthesized controls by their evaluations.

3. The synergistic procedure of the control laws for the longitudinal motion with harmonic disturbances

a). Synergistic synthesis procedure of control laws u_i

Common model of SA's space movement is present by 12[th] order differential equations system through Euler angles. In SA's movement on water or in taking off, it's rational to consider longitudinal motion model:

$$\begin{cases} \dot{x}_1(t) = b_1 x_3 x_2 - g\sin x_5 + a_1\left(P_x - F_{ax} - F_{hx}\right) + M_1(t); \\ \dot{x}_2(t) = b_2 x_2 x_3 - g\cos x_5 + a_2\left(P_y + F_{ay} + F_{hy}\right) + M_2(t); \\ \dot{x}_3(t) = a_3\left(M_z^a + M_z^h\right) + M_3(t); \\ \dot{x}_4(t) = x_1 \sin x_5 + x_2 \cos x_5; \\ \dot{x}_5(t) = x_3; \\ \dot{x}_6 = x_1 \cos x_5 - x_2 \sin x_5; \end{cases} \quad (1)$$

Where: x_1, x_2 – the projections of velocity vector V_x, V_y on corresponded the intertwined coordinate system axes; x_3 – longitudinal angular velocity ω_z; x_4 , x_6 – projections coordinate SA's center of gravity y_c, x_c on corresponded axes Oy and Ox; x_4 – pitching angle ϑ; m – SA's weight; $m_x = (1+\lambda_1)m,\ m_y = (1+\lambda_2)m$ – SA's «attached» weights; F_{ax}, F_{ay} – projections total vector of aerodynamic forces on corresponded intertwined coordinate system axes Ox and Oy; F_{hx}, F_{hy} – projections total vector of hydrodynamic and hydrostatic forces on corresponded intertwined coordinate system axes Ox and Oy; Oy; M_z^a, M_z^h – longitudinal aerodynamic moment and longitudinal moment formed by hydrodynamic and hydrostatic forces; $M_i(t)$ – disturbances;

$$a_1 = m_x^{-1};\ a_2 = m_y^{-1};\ a_3 = I_z^{-1};\ b_1 \frac{m_y}{m_x};\ b_2 = -\frac{m_x}{m_y}.$$

In control the SA's longitudinal motion elevator, flaps and engine thrust control lever are the active control organs. Technical solutions that provide basing and operation of the aircraft on the water surface, effectively determine its shape - the seaplane aerodynamic scheme. Consequently, controls in the model (2) will be the engine thrust, depending on the deviation of the engine thrust control lever; the total aerodynamic forces and the total longitudinal moment, depending on changes in the flaps and elevator deflection.

For control the SA's longitudinal motion there are some strategies: controlling individual channels or all channels simultaneously. Of course that the vector strategy requires a more complex algorithmic structure of the regulator, but it allows more flexible three-channel control of SA.

The problem of controlling the longitudinal motion is finding the control vector. $u = \left\lfloor F_x\left(\delta_{p.y.}, \delta_{p.в.}, \delta_з\right),\ F_y\left(\delta_{p.y.}, \delta_{p.в.}, \delta_з\right),\ M_z\left(\delta_{p.y.}, \delta_{p.в.}, \delta_з\right) \right\rfloor$ as a coordinate function of the system states, which provides SA's longitudinal short-period movement (2) at a given speed V_0, height H_0 and pitching angle ϑ_0, i.e. the following invariants:

$$x_1 = V_0;\ x_4 = H_0;\ x_5 = \vartheta_0 \quad (2)$$

Rewriting the mathematic model of the control object following:

$$
\begin{cases}
\dot{x}_1(t) = b_1 x_3 x_2 - g \sin x_5 + a_1 u_1; \\
\dot{x}_2(t) = -b_2 x_1 x_3 - g \cos x_5 + a_2 u_2 \ ; \\
\dot{x}_3(t) = a_3 u_3; \\
\dot{x}_4(t) = x_1 \sin x_5 + x_2 \cos x_5; \\
\dot{x}_5(t) = x_3; \\
\dot{x}_6(t) = x_1 \cos x_5 - x_2 \sin x_5;
\end{cases}
\tag{3}
$$

where $u_1 = P_x - F_{xa} - F_{xг}$, $u_2 = P_y + F_{ya} + F_{yг}$, $u_3 = M_{za} + M_{zг}$ – are control acts.

For model (3), the goal is implementation of desired invariants (2), we formulate the first set of macro-variables ψ_1, ψ_2, ψ_3,

$$
\begin{aligned}
&\psi_1 = x_1 - V_0; \\
&\psi_2 = x_2 - \varphi_1(x_4, x_5, z_1, z_2, z_3); \\
&\psi_3 = x_3 - \varphi_2(x_4, x_5, z_1, z_2, z_3),
\end{aligned}
\tag{4}
$$

which must satisfy the solution of following functional equations:

$$T_i \dot{\psi}_i(t) + \psi_i = 0, \quad T_i > 0, \quad i = 1 \ldots 3,; \tag{5}$$

At the intersection of invariant manifolds, $\psi_i = 0, i = 1, \ldots, 3$, there is a dynamic “phase space compression”, and the dynamics of closed-loop system will be described by decomposed model:

$$
\begin{cases}
\dot{x}_4(t) = V_0 \sin x_5 + \varphi_1 \cos x_5; \\
\dot{x}_5(t) = \varphi_2; \\
\dot{x}_6(t) = V_0 \cos x_5 - \varphi_1 \sin x_5;
\end{cases}
\tag{6}
$$

Now to introduce a second set of macro variables

$$\psi_4 = x_4 - H_0; \ \psi_5 = x_5 - \vartheta_0 . \tag{7}$$

The set of macro variables introduced by (7) must satisfy solutions of functional equation systems:

$$T_i \dot{\psi}_i(t) + \psi_i = 0, \quad T_i > 0, \quad i = 4,5 . \tag{8}$$

And to solve jointly equations from (6) to (8) for determining “inner” controls φ_1, φ_2 in form of functions depending on state variables:

$$\varphi_1 = -\frac{T_4 V_0 \sin x_5 + x_4 - H_0}{T_4 \cos x_5}; \ \varphi_2 = \frac{-x_5 + \vartheta_0}{T_5}. \tag{9}$$

Further external control vectors u_i is found by solving simultaneously functional equation systems (4) and equation model (1):

$$u_1 = \frac{1}{a_1}\left(g\sin x_5 + \frac{-x_1 + V_0}{T_1} - z_1 \right);$$
$$u_2 = Ax_1 + Bx_2 + Cx_3 + Dx_4 - \frac{1}{a_2} z_2 + E; \qquad (10)$$
$$u_3 = -\frac{1}{T_3 T_5 a_3}\left((T_3 + T_5)x_3 + x_5 - \vartheta_0 \right) - \frac{z_3}{a_3}.$$

Where indicated: $A = -\dfrac{\sin x_5}{T_4 a_2 \cos x_5}$; $B = -\dfrac{T_2 + T_4}{a_2 T_2 T_4}$;

$C = -\dfrac{x_4 \sin x_5}{a_2 T_4 \cos^2 x_5} + \dfrac{H_0 \sin x_5 - T_4 V_0}{a_2 T_4 \cos^2 x_5}$;

$D = \dfrac{-1}{a_2 T_2 T_4 \cos x_5}$; $E = \dfrac{H_0 - T_4 V_0 \sin x_5}{a_2 T_2 T_4 \cos x_5} + \dfrac{g \cos x_5}{a_2}$.

Whereas synthesized control laws, u_1, u_2, u_3, of object (1), provide implementation required technological problems, it is necessary to move to description of the observer synthesis procedure.

b) The observer synthesis procedure

According to the method of Analytical Design of Aggregated Regulators, in synergistic synthesis procedure of observers it should be used following an extended system model (11) [3, 4]:

$$\begin{cases} \dot{x}_1(t) = -g\sin x_5 + a_1 u_1 + z_1; \\ \dot{x}_2(t) = -g\cos x_5 + a_2 u_2 + z_2; \\ \dot{x}_3(t) = a_3 u_3 + z_3; \\ \dot{x}_4(t) = x_1 \sin x_5 + x_2 \cos x_5; \\ \dot{x}_5(t) = x_3; \\ \dot{x}_6(t) = x_1 \cos x_5 - x_2 \sin x_5; \\ \dot{z}_1(t) = s_1;\ \dot{s}_1(t) = -\sigma_1^2 z_1; \\ \dot{z}_2(t) = s_2;\ \dot{s}_2(t) = -\sigma_2^2 z_2; \\ \dot{z}_3(t) = s_3;\ \dot{s}_3(t) = -\sigma_3^2 z_3; \end{cases} \qquad (11)$$

Where σ_i – harmonic disturbance angular frequencies, z_1, z_2, z_3 – the projections of indignant linear, longitudinal and angular accelerations respectively.

The last six equations in system (11) is dynamic model of harmonic disturbances, and $z_i, s_i, \; i = \overline{1..3}$ are state variables.

The state variable observer design is based on the synergistic approach principles in the control theory, videlicet on the ADAR method, which is described in works [3, 4]. In particular case, when $\dim \psi(t) = 1$, the expression

$$\dot{\psi}(t) = L(y)\psi \tag{12}$$

Could be present in following form:

$$\dot{\psi}_i(t) + L_i \psi_i = 0, \quad L_i > 0. \tag{13}$$

To conduct the synthesis of the observers for the object (1), let $y = [x_i], \; i = 1,...,5$, $v = \lfloor z_j, s_j \rfloor, \; j = 1,2,3$. To determine the assessments of the state variables z_1, s_1, choosing forms of ψ_1, ψ_2:

$$\begin{aligned} \psi_1 &= \beta_{11}(z_1 - \hat{z}_1) + \beta_{12}(s_1 - \hat{s}_1), \\ \psi_2 &= \beta_{21}(z_1 - \hat{z}_1) + \beta_{22}(s_1 - \hat{s}_1). \end{aligned} \tag{14}$$

Where $\beta_{ij} \neq 0$ – constants, $\beta_{11}\beta_{22} - \beta_{12}\beta_{21} \neq 0$. In this the valuations $\hat{z}_1, \hat{s}_1$ of the state variables z_1, s_1 could be formed by

$$\begin{aligned} \hat{z}_1 &= f_1\ (x_1) + w_1, \\ \hat{s}_1 &= f_2\ (x_1) + w_2. \end{aligned} \tag{15}$$

where $f_1(x_1), f_2(x_1)$ – unknown functions. Then to put (14) into the equation in formed (13):

$$\begin{aligned} \dot{\psi}_1(t) + L_1\psi_1 = 0,\ L_1 > 0; \\ \dot{\psi}_2(t) + L_2\psi_2 = 0,\ L_2 > 0, \end{aligned} \tag{16}$$

while subject to the equations (15), receiving

$$\begin{aligned} &\beta_{11}\left(\frac{dz_1}{dt} - \frac{\partial f_1(x_1)}{x_1}\frac{dx_1}{dt} - \frac{d(w_1)}{dt}\right) + \beta_{12}\left(\frac{ds_1}{dt} - \frac{\partial f_2(x_1)}{x_1}\frac{dx_1}{dt} - \frac{d(w_2)}{dt}\right) + \\ &+ L_1[\beta_{11}(z_1 - f_2(x_1) - w_1) + \beta_{12}(s_1 - f_2(x_1) - w_2)] = 0, \\ &\beta_{21}\left(\frac{dz_1}{dt} - \frac{\partial f_1(x_1)}{x_1}\frac{dx_1}{dt} - \frac{d(w_1)}{dt}\right) + \beta_{22}\left(\frac{ds_1}{dt} - \frac{\partial f_2(x_1)}{x_1}\frac{dx_1}{dt} - \frac{d(w_2)}{dt}\right) + \\ &+ L_2[\beta_{21}(z_1 - f_1(x_1) - w_1) + \beta_{22}(s_1 - f_2(x_1) - w_2)] = 0. \end{aligned} \tag{17}$$

With the equations (17) subject to the object equations (11) , receiving:

$$
\begin{aligned}
&\beta_{11}\left(s_1-\frac{\partial f_1(x_1)}{x_1}\left(-g\sin x_5+a_1u_1+z_1\right)-\frac{dw_1}{dt}\right)+\\
&\beta_{12}\left(-\sigma_1{}^2 z_1-\frac{\partial f_2(x_1)}{x_1}\left(-g\sin x_5+a_1u_1+z_1\right)-\frac{dw_2}{dt}\right)\\
&+L_1\left[\beta_{11}\left(z_1-f_1(x_1)-w_1\right)+\beta_{12}\left(s_1-f_2(x_1)-w_2\right)\right]=0;\\
&\quad\beta_{21}\left(s_1-\frac{\partial f_1(x_1)}{x_1}\left(-g\sin x_5+a_1u_1+z_1\right)-\frac{dw_1}{dt}\right)+\\
&\quad\beta_{22}\left(-\sigma_1{}^2 z_1-\frac{\partial f_2(x_1)}{x_1}\left(-g\sin x_5+a_1u_1+z_1\right)-\frac{dw_2}{dt}\right)\\
&\quad+L_2\left[\beta_{21}\left(z_1-f_1(x_1)-w_1\right)+\beta_{22}\left(s_1-f_2(x_1)-w_2\right)\right]=0.
\end{aligned}
\tag{18}
$$

In the equations of the observer (18) must not be present at unobserved coordinators z_1, s_1. In order to exclude them out of system, choosing

$$
\begin{aligned}
f_1(x_1)&=\frac{\beta^2{}_{12}\beta^2{}_{21}-\beta^2{}_{22}\beta^2{}_{11}}{\beta_{12}\beta_{22}\left(\beta_{11}\beta_{22}-\beta_{12}\beta_{21}\right)}x_1,\\
f_2(x_1)&=\left(\frac{\beta_{21}\beta_{22}\beta^2{}_{11}-\beta_{11}\beta_{12}\beta^2{}_{21}}{\beta_{12}\beta_{22}\left(\beta_{11}\beta_{22}-\beta_{12}\beta_{21}\right)}-\sigma_1^2\right)x_1,\\
L_1&=-\frac{\beta_{11}}{\beta_{12}}>0,\ \ L_2=-\frac{\beta_{21}}{\beta_{22}}>0
\end{aligned}
\tag{19}
$$

Subject to (19), to solve the system of equations (18), finding

$$
\begin{aligned}
\dot{w}_1&=-\left[\left(\frac{\beta_{11}}{\beta_{12}}\right)^2+\sigma_1^2+\frac{\beta_{21}\beta_{11}}{\beta_{22}\beta_{12}}+\left(\frac{\beta_{21}}{\beta_{22}}\right)^2\right]x_1+\\
&\quad+\left(\frac{\beta_{11}}{\beta_{12}}+\frac{\beta_{21}}{\beta_{22}}\right)\left(w_1+a_1u_1-g\sin x_5\right)+w_2;\\
\dot{w}_2&=\left(\frac{\beta_{21}\beta_{11}{}^2}{\beta_{22}\beta_{12}{}^2}+\frac{\beta_{11}\beta_{21}{}^2}{\beta_{12}\beta_{22}{}^2}\right)x_1+\left(\frac{\beta_{11}\beta_{21}}{\beta_{22}\beta_{12}}\right)\left(g\sin x_5-a_1u_1-w_1\right)+\\
&\quad+\sigma_1^2\left(a_1u_1-g\sin x_5\right).
\end{aligned}
\tag{20}
$$

And the valuations $\hat{z}_1, \hat{s}_1$ of the state variables z_1, s_1 are

$$\begin{aligned}
\hat{z}_1 &= \frac{\beta^2{}_{12}\beta^2{}_{21} - \beta^2{}_{22}\beta^2{}_{11}}{\beta_{12}\beta_{22}\left(\beta_{11}\beta_{22} - \beta_{12}\beta_{21}\right)} x_1 + w_1, \\
\hat{s}_1 &= \left(\frac{\beta_{21}\beta_{22}\beta^2{}_{11} - \beta_{11}\beta_{12}\beta^2{}_{21}}{\beta_{12}\beta_{22}\left(\beta_{11}\beta_{22} - \beta_{12}\beta_{21}\right)} - \sigma_1^2 \right) x_1 + w_2.
\end{aligned} \tag{21}$$

Similarly, to define the estimations $\hat{z}_2, \hat{s}_2$, $\hat{z}_2, \hat{s}_2$ of the state variables z_2, s_2, z_2, s_2, choosing following the macro variables

$$\begin{aligned}
\psi_3 &= \beta_{33}\left(z_2 - \hat{z}_2\right) + \beta_{34}\left(s_2 - \hat{s}_2\right); \\
\psi_4 &= \beta_{43}\left(z_2 - \hat{z}_2\right) + \beta_{44}\left(s_2 - \hat{s}_2\right); \\
\psi_5 &= \beta_{55}\left(z_3 - \hat{z}_3\right) + \beta_{56}\left(s_3 - \hat{s}_3\right); \\
\psi_6 &= \beta_{65}\left(z_3 - \hat{z}_3\right) + \beta_{66}\left(s_3 - \hat{s}_3\right),
\end{aligned}
\quad \text{where} \quad
\begin{aligned}
&\beta_{33}\beta_{44} - \beta_{34}\beta_{43} \neq 0; \\
&\beta_{55}\beta_{66} - \beta_{56}\beta_{65} \neq 0;. \\
&\beta_{ij} \neq 0.
\end{aligned} \tag{22}$$

The assessments of state variables z_2, s_2, z_2, s_2 can be defined

$$\begin{aligned}
\hat{z}_2 &= f_3(x_2) + w_3, \quad \hat{s}_2 = f_4(x_2) + w_4, \\
\hat{z}_3 &= f_5(x_3) + w_5, \quad \hat{s}_3 = f_6(x_3) + w_6,
\end{aligned} \tag{23}$$

The macro variables (22) must be satisfy functional equations

$$\dot{\psi}_i(t) + L_i\psi_i = 0, \; L_i > 0, \; i = 3,...,6. \tag{24}$$

With received equations formed by putting (22) in to (16) object to model (11), we need to choose functions $f_3(x_2), f_4(x_2), f_5(x_3), f_6(x_3)$, L_i, $i = 3,...,6$ so that the expressions of the observers must not consist in itself the unobserved state variables. Choosing

$$\begin{aligned}
f_3(x_2) &= \frac{\beta^2{}_{34}\beta^2{}_{43} - \beta^2{}_{44}\beta^2{}_{33}}{\beta_{34}\beta_{44}\left(\beta_{33}\beta_{44} - \beta_{34}\beta_{43}\right)} x_2; \\
f_4(x_2) &= \left(\frac{\beta_{43}\beta_{44}\beta^2{}_{33} - \beta_{33}\beta_{34}\beta^2{}_{43}}{\beta_{34}\beta_{44}\left(\beta_{33}\beta_{44} - \beta_{34}\beta_{43}\right)} - \sigma_2^2 \right) x_2;
\end{aligned} \tag{25}$$

$$L_3 = -\frac{\beta_{33}}{\beta_{34}} > 0, \; L_4 = -\frac{\beta_{43}}{\beta_{44}} > 0$$

$$\begin{aligned}
f_5(x_3) &= \frac{\beta^2{}_{56}\beta^2{}_{65} - \beta^2{}_{66}\beta^2{}_{55}}{\beta_{56}\beta_{66}\left(\beta_{55}\beta_{66} - \beta_{56}\beta_{65}\right)} x_3; \\
f_6(x_3) &= \left(\frac{\beta_{65}\beta_{66}\beta^2{}_{55} - \beta_{55}\beta_{56}\beta^2{}_{65}}{\beta_{56}\beta_{66}\left(\beta_{55}\beta_{66} - \beta_{56}\beta_{65}\right)} - \sigma_3^2 \right) x_3.
\end{aligned} \tag{26}$$

$$L_5 = -\frac{\beta_{55}}{\beta_{56}} > 0,\ L_6 = -\frac{\beta_{65}}{\beta_{66}} > 0$$

Consequently the equations of the observer is formed

$$\begin{aligned}
\dot{w}_3(t) &= -\left[\left(\frac{\beta_{33}}{\beta_{34}}\right)^2 + \sigma_2^2 + \frac{\beta_{43}\beta_{33}}{\beta_{44}\beta_{34}} + \left(\frac{\beta_{43}}{\beta_{44}}\right)^2\right]x_2 + \\
&\quad + \left(\frac{\beta_{33}}{\beta_{34}} + \frac{\beta_{43}}{\beta_{44}}\right)\left(w_3 + a_2u_2 - g\cos x_5\right) + w_4; \\
\dot{w}_4(t) &= \left(\frac{\beta_{43}\beta_{33}{}^2}{\beta_{44}\beta_{34}{}^2} + \frac{\beta_{33}\beta_{43}{}^2}{\beta_{34}\beta_{44}{}^2}\right)x_2 + \left(\frac{\beta_{33}\beta_{43}}{\beta_{44}\beta_{34}}\right)\left(g\cos x_5 - a_2u_2 - w_3\right) + \\
&\quad + \sigma_2^2\left(a_2u_2 - g\cos x_5\right).
\end{aligned} \tag{27}$$

$$\begin{aligned}
\dot{w}_5(t) &= -\left[\left(\frac{\beta_{55}}{\beta_{56}}\right)^2 + \sigma_3^2 + \frac{\beta_{65}\beta_{55}}{\beta_{66}\beta_{56}} + \left(\frac{\beta_{65}}{\beta_{66}}\right)^2\right]x_3 + \left(\frac{\beta_{55}}{\beta_{56}} + \frac{\beta_{65}}{\beta_{66}}\right)\left(w_5 + a_3u_3\right) + w_6; \\
\dot{w}_6(t) &= \left(\frac{\beta_{65}\beta_{55}{}^2}{\beta_{66}\beta_{56}{}^2} + \frac{\beta_{55}\beta_{65}{}^2}{\beta_{56}\beta_{66}{}^2}\right)x_3 + \left(\frac{\beta_{55}\beta_{65}}{\beta_{66}\beta_{56}}\right)\left(-a_3u_3 - w_5\right) + \sigma_3^2 a_3u_3.
\end{aligned}$$

And expressions of state variable evaluations z_2, z_3, s_2, s_3 is described

$$\begin{aligned}
\hat{z}_2 &= \frac{\beta^2{}_{34}\beta^2{}_{43} - \beta^2{}_{44}\beta^2{}_{33}}{\beta_{34}\beta_{44}\left(\beta_{33}\beta_{44} - \beta_{34}\beta_{43}\right)}x_2 + w_3, \\
\hat{s}_2 &= \left(\frac{\beta_{43}\beta_{44}\beta^2{}_{33} - \beta_{33}\beta_{34}\beta^2{}_{43}}{\beta_{34}\beta_{44}\left(\beta_{33}\beta_{44} - \beta_{34}\beta_{43}\right)} - \sigma_2^2\right)x_2 + w_4; \\
\hat{z}_3 &= \frac{\beta^2{}_{56}\beta^2{}_{65} - \beta^2{}_{66}\beta^2{}_{55}}{\beta_{56}\beta_{66}\left(\beta_{55}\beta_{66} - \beta_{56}\beta_{65}\right)}x_3 + w_5, \\
\hat{s}_3 &= \left(\frac{\beta_{65}\beta_{66}\beta^2{}_{55} - \beta_{55}\beta_{56}\beta^2{}_{65}}{\beta_{56}\beta_{66}\left(\beta_{55}\beta_{66} - \beta_{56}\beta_{65}\right)} - \sigma_3^2\right)x_3 + w_6;
\end{aligned} \tag{28}$$

Thus, combining equations (20) and (27), we obtain a nonlinear state observer for the external harmonic wave disturbances. Note that the unobserved variable z_1, z_2, z_3 in the synthesized controls (10) should be replaced by its estimates $\hat{z}_1, \hat{z}_2, \hat{z}_3$ (15) and (28).

4. Simulation

The results of computer simulation of closed-loop system (11) with the synthesized NEPO are shown in figure 1 to figure 17.

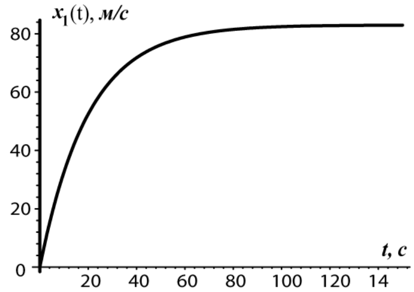

Fig. 1 Transient process relatively horizontal speed V_x

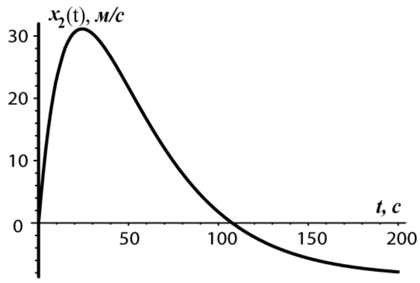

Fig. 2 Transient process relatively vertical speed V_y

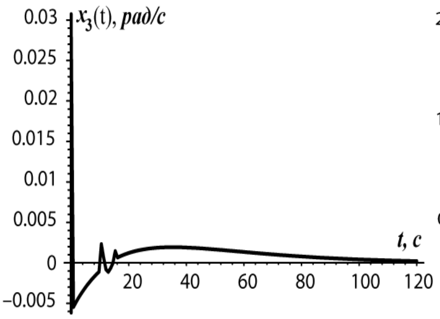

Fig. 3 Transient process relatively angular speed ω_z

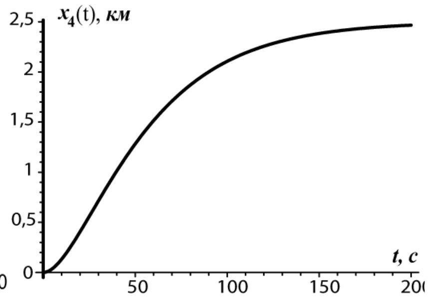

Fig. 4 Transient process relatively flight height H

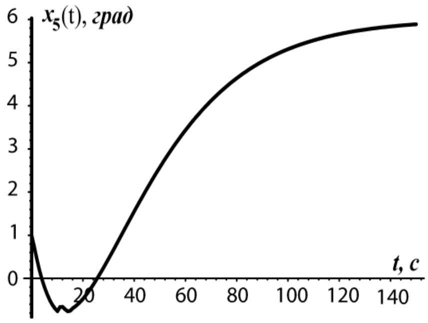

Fig. 5 Transient process relatively pitch angular speed ϑ

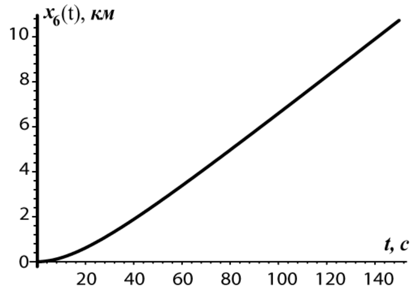

Fig. 6 Transient process relatively flight distance X

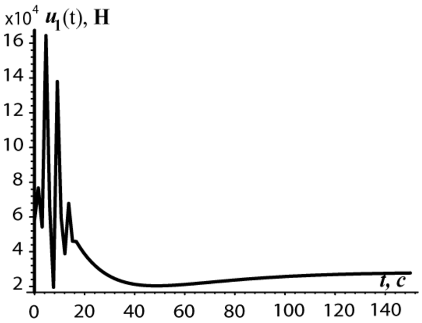

Fig. 7 Transient process relatively control u_1

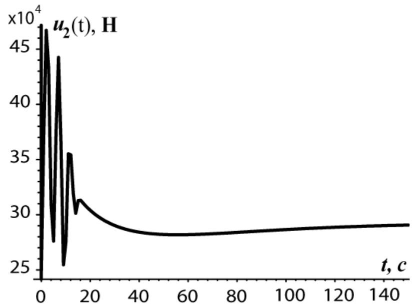

Fig. 8 Transient process relatively control u_2

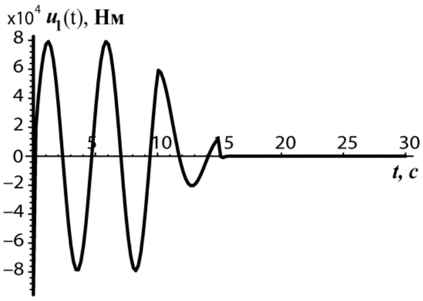

Fig. 9 Transient process relatively control u_3

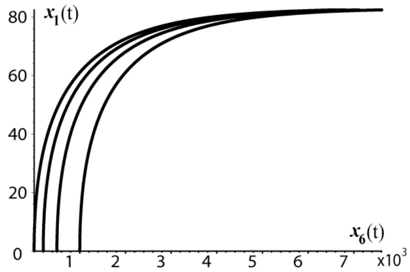

Fig. 10 Projection of system phase trajectory on surface $x_1(t)$ & $x_6(t)$

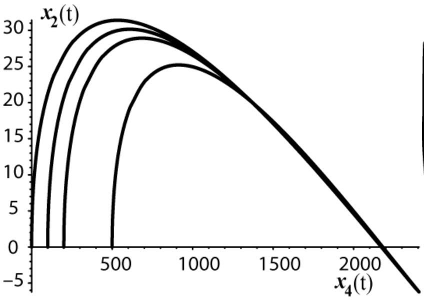

Fig. 11 Projection of system phase trajectory on surface $x_2(t)$ & $x_4(t)$

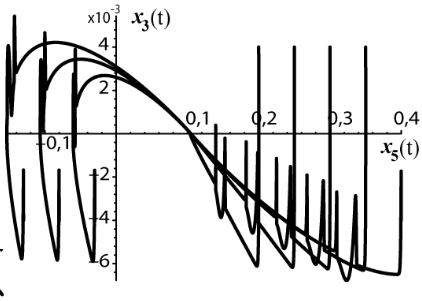

Fig. 12 Projection of system phase trajectory on surface $x_3(t)$ & $x_5(t)$

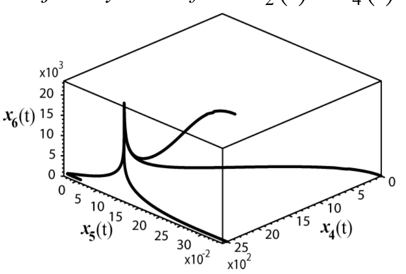

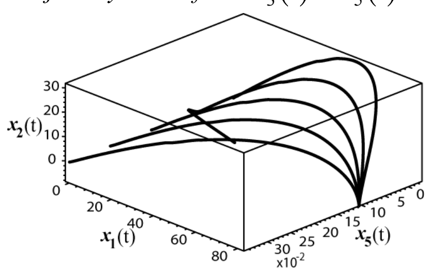

Fig. 13 Phase portrait in space $x_4(t), x_5(t), x_6(t)$

Fig. 14 Phase portrait in space $x_5(t),\ x_1(t),\ x_2(t)$

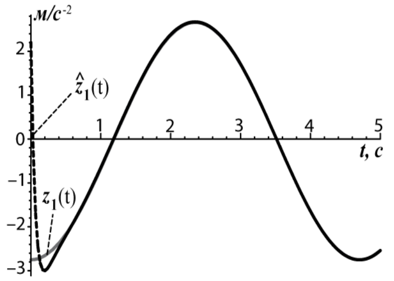

Fig. 15 Transient process relatively disturbance $z_1(t)$ *and its estimation*

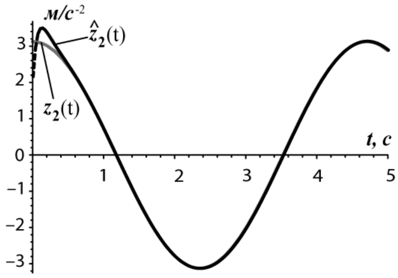

Fig. 16 Transient process relatively $z_2(t)$ *and its estimation*

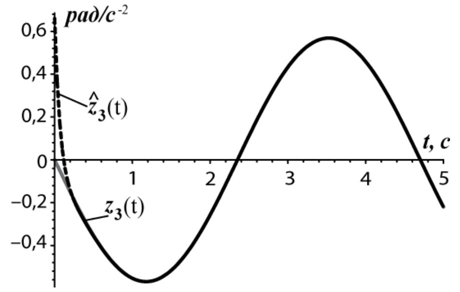

Fig. 17 Transient process relatively $z_3(t)$ *and its evaluation*

5. Conclusion

This work is described the synergistic approach to problem of synthesis of effective correlated control laws of longitudinal motion SA under sea wave conditions, particularly in taking off process from water surface.

In conducting the simulation showed that the SA's longitudinal motion control objectives are achieved and using synthesized control laws can significantly improve motion performance: decreasing pitch angle oscillation, angular rate fluctuations and SA's gravity center oscillation. The observers estimate the unobserved disturbances with high measurement accuracy (fig.15-fig.17).

Thus, using synergetic control theory enable to create new classes of SA's motion control systems.

Reference

1. *Андриевский Б.Р., Фрадков АЛ.* Избранные главы теории автоматического управления с примерами на языке MATLAB. С.-Петербург: Наука, 1999.
2. *Фомин В.Н., Фрадков А.Л., Якубович В.А.* Адаптивное управление динамическими объектами. – М.: Наука, 1981.
3. *Колесников А.А.* Синергетическая теория управления. Таганрог: ТРТУ, М.: Энергоатомиздат, 1994. 344 с.

4. Современная прикладная теория управления: Синергетический подход к теории управления / под ред. А.А. Колесникова. – Таганрог: Изд-во ТРТУ, 2000. – Ч II.

5. *Колесников А.А., Веселов Г.Е., Кузьменко А.А.* Новые технологии проектирования современных систем управления процессами генерации электроэнергии. – М.: 2009. 323 с.

On-off intermittency in the Ising model with temperature randomly varying in time

A. Krawiecki

Warsaw University of Technology, Koszykowa 75, PL-00-662 Warsaw, Poland
(E-mail: akraw@if.pw.edu.pl)

Abstract. Ferromagnetic Ising model is investigated by means of Monte Carlo simulations, with temperature randomly varying in time, which assumes randomly values above and below the critical temperature in the consecutive simulation steps. It is known that for mean-field coupling on-off intermittency and attractor bubbling can be then observed, characterized by the sequence of laminar phases, during which the magnetization is almost zero, and chaotic bursts, during which the system becomes abruptly ordered. At the intermittency threshold distribution of the values of magnetization obeys a power scaling law. Here, possibility of the occurrence of analogous phenomena is studied in the Ising model on d-dimensional square lattices and on small-world networks which are obtained from the square ones by random rewiring of edges (corresponding to non-zero exchange integrals) with probability p. For the models on square lattices ($p = 0$) intermittent sequences of laminar phases and bursts of magnetization are observed only for $d \geq 4$; also only for $d \geq 4$ the distributions of values of magnetization exhibit power-law tails. For the models on small-world networks ($p > 0$) such distributions occur for $d \geq 2$. Thus, time series with certain properties of on-off intermittency can be observed close to the phase transition point in the above-mentioned generic models of statistical physics.
Keywords: on-off intermittency, attractor bubbling, Ising model.

On-off intermittency (OOI) appears in chaotoc systems in which the observed signal forms a sequence of laminar phases, during which it is almost constant and close to zero (the "off" phase) and chaotic bursts ("on" state) [1,2]. The system can stay in the laminar phase for a long time, after which the burst can appear, i.e., rapid departure from, and return to, the "off" state. OOI occurs in systems which posses a chaotic attractor contained within an invariant manifold with dimension smaller than that of the phase space. As a control parameter is varied, this attractor can lose transverse stability as a result of a supercritical blowout bifurcation [3], and a new attractor is formed which encompasses that contained within the invariant manifold. Just above the bifurcation threshold the phase trajectory spends most of the time in the vicinity of the invariant manifold and only occassionally departs from it, which results in the sequence of the laminar phases and bursts. In turn, if during the laminar phases instead of approaching zero the signal shows fluctuations with amplitude small in comparison with that of chaotic bursts, the corresponding phenomenon is called attractor bubbling (AB) [2,4]. AB appears in systems with OOI under the influence of the internal or external noise, which amplifies local transverse inastabilities in the attractor contained within the invariant manifold [2]. This results in the appearance of intermittent bursitng below the blowout bifurcation threshold. OOI and AB were observed in many nonlinear dynamical systems, e.g., in model maps with time-dependent control parameter [1], in systems of coupled chaotic oscillators close to the synchronization threshold, where the invariant manifold is the synchronization manifold [5], in chaotic dynamics of spin waves [6], microscopic models of financial markets [7,8], etc.

It is interesting to note that OOI and AB can occur in many-body systems of statistical physics, e.g., in the Ising and Ising-like models [8-10] or electroconvection of nematic liquid crystals [11], under the influence of random variation of external parameters (the temperature or the elecric voltage in the two above-mentioned cases, respectively). In particular the ferromagnetic Ising model with temperature randomly varying in time can switch intermittently between the paramagnetic and ordered phase, which results in the sequence of the laminar phases and bursts in the time series of magnetization, treated as the signal. In the latter case OOI and AB have been observed so far in the Ising model with mean-field (MF) coupling [9]. The purpose of this paper is to show that these phenomena can appear also if the MF approximation is not exact, e.g., in the d-dimesnional Ising model with $d = 2, 3, 4 \ldots$ and, possibly, a small fraction of random connections corresponding to long-range exchange interactions between distant spins. It should be emphasized that the Ising model is a stochastic one (Glauber thermal bath dynamics is used in the Monte Carlo (MC) simulations), and the intermittency typical of dynamical systems appears in it as a result of interactions among a large number of stochastic units (spins). Thus the name "emergent" OOI and AB can be given to this kind of intermittent phenomena.

The model investigated in this paper is the ferromagnetic Ising model on a network which can be either a usual d-dimensional square lattice, with $d \geq 2$, or a small-world network obtained from the d-dimensional square lattice by random cutting and rewiring of edges [12]. For the latter purpose, each edge of the square lattice is cut with probability p and rewired so that one (randomly selected) end remains attached to an old node while the other one is attached to a new node, chosen randomly from among all nodes in the network. Multiple connections between nodes, self-connections and cutting edges once rewired are forbidden. The probability p controls the degree of randomness in the network: in particular, for $p = 0$ the network is the d-dimensional square lattice, and for $p = 1$ it is a random graph. The spins σ_i, $i = 1, 2, \ldots N$, $N = L^d$, where L is the size of the original square lattice and N is the number of spins, have two possible orientations, $\sigma_i = \pm 1$, and are located in the nodes of the network. The exchange integral between the spins σ_i, σ_j is $J_{ij} = J > 0$ if there is an edge between nodes i, j, and $J_{ij} = 0$ otherwise; hence, for $p > 0$ a certain fraction of long-range interactions between spins is present. The Hamiltonian for the model is

$$H = -\sum_{i,j=1}^{N} J_{ij}\sigma_i\sigma_j. \tag{1}$$

MC simulations of the above-mentioned model are performed with temperature randomly varying in time, $T(t) = T_0 - T_1\xi(t)$, where the discrete time steps t are equivalent to the consecutive MC simulation steps (each step corresponding to asynchronous updating of all N spins), $\xi(t)$ is a random variable with uniform distribution on the interval $(0,1)$, and T_0, T_1 are constants. The model obeys the Glauber thermal-bath dynamics, with the transition rates between two spin configurations which differ by a single flip of one spin, e.g., that in the node i, in the form

$$w_i(\sigma_i, t) = \frac{1}{2}\left[1 - \sigma_i \tanh\left(\frac{I_i}{T(t)}\right)\right], \tag{2}$$

where

$$I_i = J\sum_{j\in\mathcal{K}_i} \sigma_j \tag{3}$$

is a local field acting on the spin i, and the sum in Eq. (3) runs over all neighbors of the node i (in particular, in the case of the d-dimensional square lattice, corresponding to $p = 0$, there are $z = 4, 6, 8\ldots$ nearest neighbors for $d = 2, 3, 4\ldots$, where z is the coordination number). Let us emphasize that the transition rates (2) depend on time due to the time dependence of the temperature $T(t)$.

For $T_1 = 0$ the models under study with $d = 2, 3, 4\ldots$ show ferromagnetic phase transition for $p \geq 0$, and the critical temperature T_c for given d is an increasing function of p. The order parameter is, of course, the magnetization $M = N^{-1}\sum_{i=1}^{N}\sigma_i$. Henceforth in the MC simulations it is always assumed that $T_0 > T_c$ for given d, p and the network size N. For $T_1 > 0$ the magnetization cannot be treated as the (static) order parameter since it can become dependent on time, in particular if $T_0 - T_1 < T_c$. Instead, the statistical properties of the time series $M(t)$ can be analyzed to search for the occurrence of the OOI or AB.

In the MF approximation, and in the thermodynamic limit, the equation for the time dependence of the magnetization becomes

$$M(t+1) = \tanh\left(\frac{J\langle z\rangle}{T(t)}M(t)\right) \approx \frac{J\langle z\rangle}{T(t)}M(t), \tag{4}$$

where $\langle z\rangle$ is the average coordination number ($\langle z\rangle = z = 4, 6, 8\ldots$ for $p = 0$ and $d = 2, 3, 4\ldots$), and the approximate equality is valid for $M \approx 0$. For $T_1 = 0$ and $T(t) = T_0 =$ const the magmetization $M(t)$ for $t \to \infty$ converges to zero if $T_0 > T_c^{(mf)} = \langle z\rangle J$, i.e., above the MF critical temperature, which corresponds to the paramagnetic phase, and to a non-zero value if $T_0 < T_c^{(mf)}$, which corresponds to the ordered phase. For $T_1 > 0$ Eq. (4) can be treated as a one-dimensional map describing the evolution of the magnetization $M(t)$ in discrete time t. This map possesses an invariant manifold $M(t) \equiv 0$, corresponding to the paramegnetic phase, and the temperature $T(t)$ is a (random) variable describing the dynamics of the two-dimensional system $(M(t), T(t))$ within this manifold. The map (4) belongs to a general class of systems $x_{t+1} = f(x_t, \eta_t)$ which after linearization in the vicinity of the invariant manifold $x_t \equiv 0$ have a form of multiplicative noise, $x_{t+1} = \eta_t x_t$, where η_t is a random variable. As the strength of the noise η_t rises the manifold $x_t \equiv 0$ loses stability via supercritical blowout bifurcation and OOI in the time series of x_t is observed; in Eq. (4), since $T_0 > T_c^{(mf)}$, this happens as T_1 is increased. In fact, OOI was observed in Eq. (4) as well as in the time series of magnetization obtained from MC simulations of the Ising model with temperature randomly varying in time and with MF coupling [9], where Eq. (4) is strict for $N \to \infty$, as T_1 was increased above the threshold value for the blowout bifurcation. Besides, in the MC simulations AB was also observed, i.e., chaotic bursts of magnetization which occurred for $T_1 < T_0 - T_c$, below the intermittency threshold, due to thermal fluctuations (internal noise) which destabilize the invariant manifold (the paramagnetic state) in finite-size systems.

In the cases studied in this paper neither OOI nor AB occur in the two- and three-dimensional Ising model on square lattices (for $p = 0$ and $d = 2, 3$, $T_0 > T_c$ and $0 < T_1 < T_c$): the magnetization exhibits only small fluctuations around zero (Fig. 1(a,c)). However, addition of even a small fraction of rewired edges ($p > 0$) leads to the occurrence of chaotic bursts in the time series of $M(t)$ typical of AB for large enough T_1 in the models with $d = 2, 3$ (Fig. 1(b)). In contrast, in the four-dimensional Ising model bursts in the time series of $M(t)$ occur both for $p = 0$ (the square lattice, Fig. 1(d)), if T_0 is slightly above T_c and T_1 is large enough, and for $p > 0$ (the small-world network, Fig. 1(e,f)), in a much wider range of the parameters T_0, T_1.

A characteristic feature of OOI is the distribution of lengths τ of laminar phases at the intermittency threshold, $P(\tau) \propto \tau^{-3/2}$ [1]; in the case of AB, due to the presence of noise, long laminar phases are less probable to occur and the tail of the distribution becomes exponential [4]. In the models studied in this paper, even for $N \simeq 10^4$, the thermal fluctuations were too strong to observe the power scaling law, and even for short laminar phases the distribution $P(\tau)$ decreased exponentially. Another characteristic feature of AB is the distribution of the values of the measured signal which exhibits power-law tails [13,14]. In the two- and three-dimesional Ising model on square lattices (for $p = 0$ and $d = 2, 3$, $T_0 > T_c$ and $0 < T_1 < T_c$) the distributions $P(M)$ have exponential rather than power-law tails (Fig. 2(a,b)), which confirms that no AB occurs. In contrast, in the Ising model on small-world networks with $d = 2, 3$ and $p > 0$ the tails of the distributions of magnetization obey

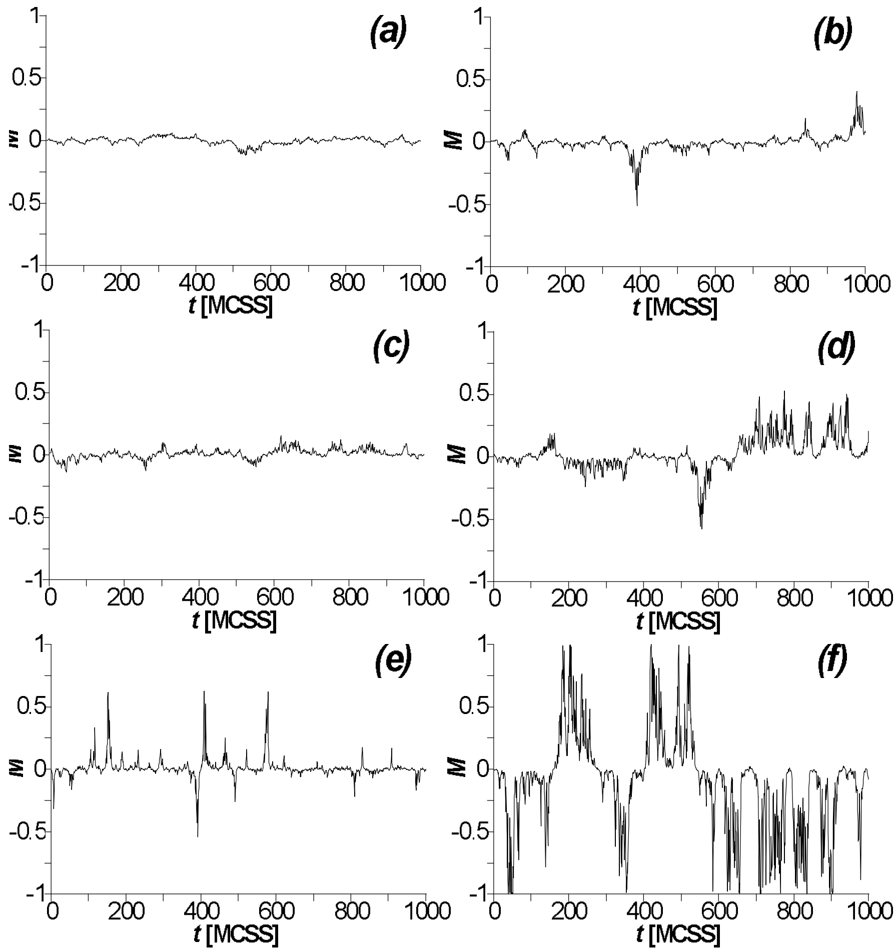

Fig. 1. Time series of magnetization $M(t)$ for the models with (a) $d = 2$, $L = 256$, $p = 0$ (two-dimensional square lattice), $T_0 = 2.45$, $T_1 = 2.44$; (b) $d = 2$, $L = 256$, $p = 0.2$ (small-world network obtained from the two-dimensional square lattice), $T_0 = 3.25$, $T_1 = 3.24$; (c) $d = 3$, $L = 40$, $p = 0$ (three-dimensional square lattice), $T_0 = 4.60$, $T_1 = 4.59$; (d) $d = 4$, $L = 16$, $p = 0$ (four-dimensional square lattice), $T_0 = 6.75$, $T_1 = 6.74$; (e) $d = 4$, $L = 16$, $p = 0.2$ (small-world network obtained from the four-dimensional square lattice), $T_0 = 10.0$, $T_1 = 9.99$; (f) $d = 4$, $L = 16$, $p = 0.2$, $T_0 = 7.35$, $T_1 = 7.34$.

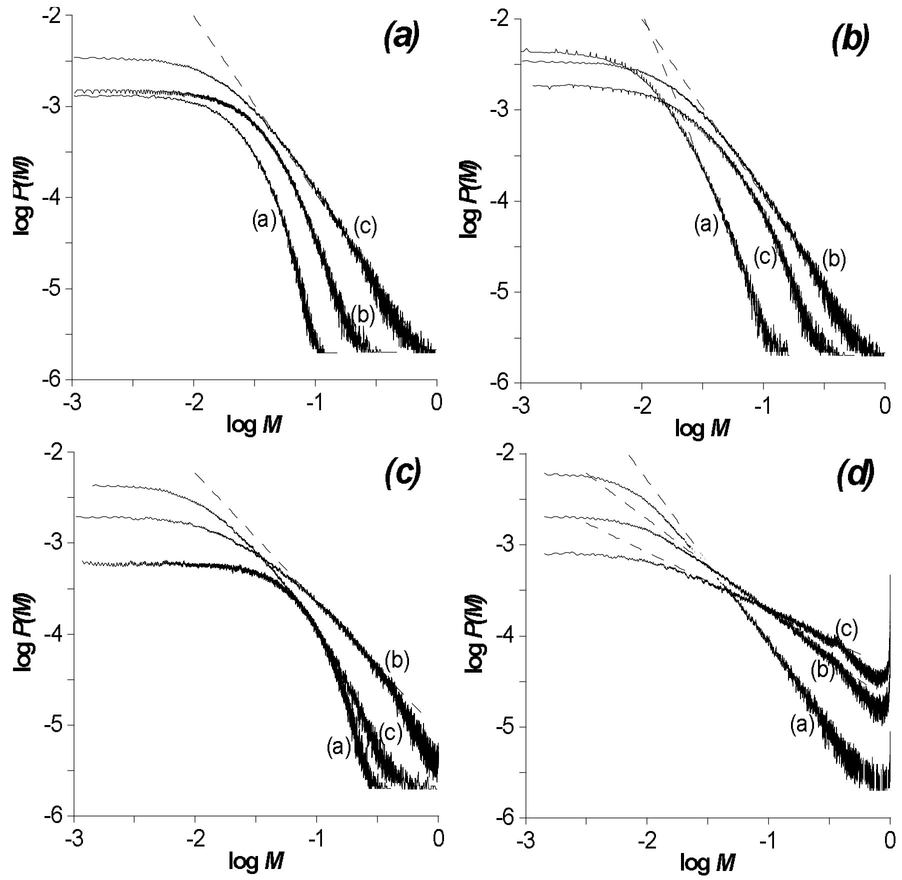

Fig. 2. Distributions of the magnetization $P(M)$ (solid lines) and possible fits of the power scaling laws to the tails of the distributions (dashed lines) for the models with (a) $d = 2$, $L = 256$ and $p = 0$, $T_0 = 2.45$, $T_1 = 2.44$ (curve (a)), $p = 0.2$, $T_0 = 3.25$, $T_1 = 1.00$ (curve (b)), $p = 0.2$, $T_0 = 3.25$, $T_1 = 3.24$ (curve (c)); (b) $d = 2$, $L = 256$ and $p = 0.2$, $T_0 = 4.25$, $T_1 = 4.24$ (curve (a)), $d = 2$, $L = 100$ and $p = 0.2$, $T_0 = 3.25$, $T_1 = 3.24$ (curve (b)), $d = 3$, $L = 40$ and $p = 0.0$, $T_0 = 4.60$, $T_1 = 4.59$ (curve (c)); (c) $d = 4$, $L = 16$, $p = 0$ and $T_0 = 6.75$, $T_1 = 1.0$ (curve (a)), $T_0 = 6.75$, $T_1 = 6.74$ (curve (b)), $T_0 = 7.75$, $T_1 = 7.74$ (curve (c)); (d) $d = 4$, $L = 16$, $p = 0.2$ and $T_0 = 10.0$, $T_1 = 9.99$ (curve (a)), $T_0 = 8.0$, $T_1 = 7.99$ (curve (b)), $T_0 = 7.35$, $T_1 = 7.34$ (curve (c)).

the power scaling law, $P(M) \propto M^{-\alpha}$, $\alpha > 0$, for a certain range of $T_0 > T_c$ and large enough T_1 (Fig. 2(a,b)). In the four-dimensional Ising model on the square lattice ($d = 4$, $p = 0$) for T_0 just above T_c and large enough T_1 the distribution $P(M)$ obeys the power scaling law on a narrow interval; otherwise, $P(M)$ has exponential tails (Fig. 2(c)). For $d = 4$ and the small-world networks with $p > 0$ the tails of the distribution of the magnetization obey a power scaling law $P(M) \propto M^{-\alpha}$ for a wide range of the parameters T_0, T_1 (Fig. 2(d)). These results confirm that the occurrence of bursts in the time series of magnetization shown in Fig. 1 (b,d,e,f) for the cases $d = 2, 3$, $p > 0$ and $d = 4$, $p \geq 0$ can be attributed to AB. In general, if the power scaling law $P(M) \propto M^{-\alpha}$ is observed the exponent $\alpha > 0$ decreases as T_0 approaches T_c from above and as T_1 is increased (Fig. 2(b,d)), since this leads to stronger and more frequent bursts in the time series of magnetization (Fig. 1(e,f)).

The above-mentioned results show that if the temperature varies randomly in time within a certain interval AB can be observed in the Ising model on small-world networks obtained from the two- and three-dimensional square lattices by cutting and rewiring edges with probability $p > 0$. Due to the presence of shortcuts the interactions between spins have a MF character to some degree, but only for $p = 1$ the network becomes a random graph and the MF approximation, Eq. (4) becomes exact. Thus, AB can occur even if the MF approximation is not strict. In the four-dimensional Ising model AB can be observed both in the case of square lattice and the small-world network. Thus, the critical dimension for the occurrence of AB in the Ising model on a square lattice, with temperature randomly varuing in time, is $d = 4$.

It should be mentioned that a class of models similar to the ones considered in this paper was used in Ref. [10] to simulate the time series of price returns in the stock market. The two possible orientations of spins (agents) corresponded to the decisions to sell or to buy stocks, and instead of temperature varying randomly in time, exchange integrals between pairs of interacting agents varied randomly in time around the average which was also a random function of time. The agents were placed on a two-dimensional square lattice, and interactions with the first, second, third, etc. nearest neighbors were taken into account; then, small-world networks were also constructed by randomly cutting and rewiring edges with probability p. Parallel updating of the states of all agents was performed. Such Ising-like multi-agent models based on the social impact theory [15] are often used to reproduce so-called "stylized facts", or universal properites of the fluctuations of the stock prices [16]. In particular, the probability distributions of the stock price returns obtained from MC simulations, proportional to the magnetization, could exhibit power-law tails for $p > 0$, which is typical of the empirical distributions of returns. Also the time series of returns (magnetization) exhibited the empirically observed "volatility clustering", i.e., a sequence of quiescent (laminar) phases and bursts.

The results of the present paper as well as these of Refs. [8-11] confirm that "emergent" OOI and AB are ubiquitous phenomena in many-body systems of statistical physics. In the Ising model studied in this paper the appearance of OOI in the time series of magnetization can be easily understood within the MF approximation: as the amplitude of the stochastic variation of the external parameter (temperature) increases the invariant manifold $M = 0$, corresopnding to the paramagnetic phase, loses transverse stability as a result of the blowout bifurcation; in finite-size systems the occurrence of chaotic bursts of magnetization is facilitated due to interal noise (thermal fluctuations) and AB is observed. However, the results of the MC simulations show that similar intermittent phenomena occur even if the MF approximation is not exact.

References

1.N. Platt, E. A. Spiegel, and C. Tresser, *Phys. Rev. Lett.* 70:279, 1993; J. F. Heagy, N. Platt, and S. M. Hammel, *Phys. Rev. E* 49:1140, 1994; S. C. Venkataramani et al., *Physica D* 96:66, 1996.
2.P. Ashwin, J. Buescu, and I. N. Stewart, *Phys. Lett. A* 193:126, 1994.
3.E. Ott and J. Sommerer, *Phys. Lett. A* 188:39, 1994.
4.N. Platt, S. M. Hammel, and J. F. Heagy, *Phys. Rev. Lett.* 72:3498, 1994; S. C. Venkataramani et al., *Phys. Rev. Lett.* 77:5361, 1996.
5.A. Čenys et al., *Phys. Lett. A* 213:259, 1996.
6.F. Rödelsperger, A. Čenys, and H. Benner, *Phys. Rev. Lett.* 75:2594, 1995; A. Krawiecki and A. Sukiennicki, *Acta Phys. Polonica A* 88:269, 1995.
7.T. Lux and M. Marchesi, *Nature* 297:498, 1999;
8.A. Krawiecki, J. A. Holyst, and D. Helbing, *Phys. Rev. Lett.* 89:158701, 2002.
9.L. Stepień and A. Krawiecki, *Phys. Stat. Solibi (b)* 236:511, 2003.
10.A. Krawiecki, *Int. J. Modern Phys. C* 19:1035, 2008.
11.T. John, R. Stannarius, and U. Behn, *Phys. Rev. Lett.* 83:749, 1999.
12.D. J. Watts and S. H. Strogatz, *Nature* (London) 393:440, 1998.
13.S. C. Venkataramani, T. M. Antonsen Jr., E. Ott, and J. C. Sommerer, *Phys. Lett. A* 207:173, 1995, *Physica D* 96:66, 1996.
14.P. Ashwin and E. Stone, *Phys. Rev. E* 56:1635, 1997.
15.B. Latané, *Am. Psychol.* 36:343, 1981; W. Weidlich, *Phys. Rep.* 204:1, 1991; D. Helbing, *Quantitative Sociodynamics* (Kluwer Academic, Dordrecht, 1995)
16.R. N. Mantegna and H. E. Stanley, *An Introduction to Econophysics: Correlations and Complexity in Finance* (Cambridge University Press, Cambridge, UK, 1999); J.-P. Bouchaud and M. Potters, *Theory of Financial Risk* (Cambridge University Press, Cambridge, UK, 1999); H. Levy, M. Levy, and S. Solomon, *Microscopic simulations of financial markets* (Academic Press, New York, 2000); J. Voit, *The Statistical Mechanics of Financial Markets*, 2nd ed., (Springer, Heidelberg 2003).

THE PECULIARITIES OF THE CELLS METABOLISM DUE TO THE FLOW OF LIQUID THROW CELL MEMBRANE

O.I. Krivosheina, I.V. Zapuskalov,Y.I Khoroshikh, O.B.Zapuskalova
Siberian State Medical University, Tomsk, Russia
E-mail: oikr@yandex.ru

Abstract: A device is designed for *in vitro* modeling of the directed flow of a nutrient medium similar to the fluid flow in the eyeball. The primary culture of human fibroblasts was cultivated in the permanent directed flow of the medium for 24 and 48 h. Under dynamic conditions, an increase in the intracellular fermentative activity of cells of the fibroblastic population and the acceleration of the process of their differentiation into mature forms were observed.

Keywords: culture of human fibroblasts, the fluid flow, the intracellular fermentative activity, the process of the differentiation/

Implementation of morphofunctional capabilities of cells intermediating the initiation, development, and outcome of any pathological process depends significantly on the modulating influence of microenvironment factors. In the eyeball, the microenvironment consists of the interacting system of anatomico-physiological features and extrastromal regulation components. Anatomico-physiological features are determined by the presence of the directed flow of the intraocular fluid and by the fibrillar structure of the vitreous body. Extrastromal components are represented by cellular elements migrating into the vitreal cavity (cells of the retinal pigment epithelium, monocytes/macrophages, lymphocytes, etc.) and by humoral factors (cytokines, growth factors). Of particular interest, in our opinion, is the directed flow of fluid in the eyeball induced by the pressure gradient.

The aim of this work was to study the influence of the directed fluid flow on the morphofunctional state of human fibroblasts.

A device has been designed for the *in vitro* modeling of the flow of a nutrient medium similar to the fluid flow in the eyeball. The device is a closed system with a chamber equipped with a semipermeable filter. The system was first filled with the nutrient medium with the aid of a vessel. The nutrient medium contained 200.0 ml of the DMEM nutrient medium in the Iscove modification and the 4% gentamicin solution (0.02 ml gentamicin per 10.0 ml of the nutrient medium). For the study, we used the fibroblast culture of human lung after 3 to 4 passages in a concentration of $5 \cdot 10^4$ cells/ml.

The cellular material came to the chamber through a valve hole. The chamber was connected to the vessel containing the nutrient medium through a roller pump equipped with a maintaining valve.

The roller pump generated the uniform directed flow of the nutrient medium with a rate of 2.1-2.4 mm^3/min. The primary culture was incubated in the permanent flow of the nutrient medium under the cultivation conditions kept unchanged for 24 and 48 h. For control purposes, fibroblasts were cultivated on a semipermeable filter placed in a Petri dish with the nutrient medium at the strict observance of temperature conditions (37° C), CO_2 content (5-7%), and the humidity level (100%).
The cellular material was examined by cytochemical methods.

At the flow cultivation of fibroblasts, the following results were obtained.

Twenty four hours after the beginning of the experiment, the cytochemical analysis revealed the moderate activity of α-naphtylacetatesterase (22.56+/-0.90) and alkaline phosphatase (10.23+/-1.05) in cultivated cells. The area of the cell surface averaged 238.94+/-5.36.

Forty eight hours later, the activity of the both ferments in the described cells increased compared to the initial indices and to cells cultivated under standard conditions ($p_Z<0.01$). In this case, the level of α-naphtylacetatesterase was 26.98+/-0.87, while that of alkaline phosphatase was 14.67+/-1.21. The area of cell surface of fibroblasts averaged 179.43+/-7.81 ($p_Z<0.001$).

When fibroblasts were cultivated under standard (stationary) conditions, in the entire series of experiments the cytochemical analysis revealed the low activity of α-naphtylacetatesterase in cells. This activity increased gradually during the cultivation ($p_Z<0.05$). No alkaline phosphatase was observed in cultivated cells. The area of cell surface was 307.19+/-6.02 24 h later and 211.66+/-5.29 ($p_Z<0.001$) 48 h later.

The utmost discovery of the 19th century – the discovery of a cell in a living organism – stimulated the intense study of various pathologies from the position of the cellular structure of organs and tissues. R. Virchow in his classical paper "Die cellular Pathologie in ihrer Begrundung auf physiologische und pathologische Gewebelehre", systematizing voluminous experimental data, for the first time presented a complex organism as a system of cell or a "cell nation."

However, during the whole era of optical microscopy in morphology, a cell was thought to be a so stable component of a tissue and organ structure that its functional and morphological changes observable in an optical microscope seemed to be not related to the dynamics of cellular structures. The idea of a cell as a versatile and unchangeable unit of tissues and organs dominated.

Only new methods of morphological investigations, first of all, electronic microscopy, changed radically the idea of a cell and dynamics of its changes. The cell culture technique, which allows cells to be studied in their living state, actual action, and interaction with the microenvironment, has helped significantly in the understanding of the integration and interpenetration of the structure and functions. Intracellular structures and biochemical processes occurring in them, as well as the permanent energy flow in a cell are in a deep and close relation with each other, and together they complete the integral pattern of the united structural-functional system, namely, a cell.

One of the main functions of the cell surface and the plasmatic membrane is the perception and transfer of external regulatory signals into a cell. Just this function is responsible, to a great extent, for the interaction between the function of the cell membrane, its permeability, and the activity of intracellular metabolism processes. Now a significant progress is achieved in the understanding of molecular mechanisms of information reception, processing, and transfer from the plasmalemma to intracellular organelles. It is established that modulating factors of the extracellular medium act as exogenous regulatory signals contacting with receptors of the cell surface. Under the conditions of our experiments, the permanent directed flow of the nutrient medium and the extracellular matrix can be such an exogenous signal for fibroblasts adhesed to the filter.

We can assume that after the interaction of the external signal with cell receptors, a cascade mechanism of certain intracellular processes is initiated. Thus, for example, changes occur in the structure of receptor-related membrane ferments, which catalyze the synthesis of endogenous regulatory molecules. As a result, their concentration changes, and the cell permeability changes too. Variations of the membrane potential also play an important role.

It should be emphasized that the plasmatic membrane not only serves a mechanic barrier, but also regulates the consecutive income of substances to a cell. Diffusion into tissue complies with Fick's law that reads as follows: as soon as differences in concentration of one or another substance appear in the medium, there is a flux of this substance leading to decrease in its concentration, which is proportionate to the concentration gradient.

This equation applies to describe movement of molecules as well as microparticles if their concentration is small.

Liposoluble low-molecular substances, first of all oxygen and carbon dioxide – also penetrate easily through endothelial cells.

All macromolecules, such as proteins, nucleic acids, polysaccharides, and lipoproteid complexes, come to a cell through the vesicle formation and joining process, that is, endocytosis. The higher is the speed of the directed fluid flow through a cell, the more intense is the endocytosis process, and, correspondingly, the greater amount of substances comes into the cell. This, in its turn, determines the degree of the metabolic activity of the cell, which is confirmed by the results of fibroblast cultivation under the flow conditions.

The speed of the movement of water molecules inside the cell is also caused by physical forces: gradients of the osmotic and hydraulic pressures on the both sides of a cell. The higher the gradient, the faster is the intracellular motion of water molecules and, correspondingly, transport vesicles, which transport nonliposoluble substances, moving from one compartment to other.

The directed movement of transport vesicles results in the reconstruction of cellular compartments and the cell surface, as well as the retention or destruction of intercellular units. One can assume that the content and components of the donor compartment would ultimately disappear in the process of transportation and the donor compartment (endoplasmic reticulum in this case) would decrease in size, while the size of the acceptor (Golgi complex) would, correspondingly, increase. However, this does not occur, because in the cell there homeostatic mechanisms, regulating and maintaining the composition of every organelle, for example, with the aid of the membrane return mechanism. As transport vesicles of the endoplasmic reticulum fuse with the acceptor membranes of the Golgi complex, certain proteins return from the Golgi back to the endoplasmic reticulum. This process is known as a retrograde transport. In contrast to it, at the anterograde transport, proteins continue to move along the secretory pathway, namely, intercisterna coated vesicles transport them through cisternae of the Golgi complex.

At the most part of the Golgi trans-network, proteins are sorted, and, leaving this compartment, they are distributed over primary lysosomes, constitutive vesicles, and secretory granules depending on their designation: in the plasma membrane, in the cell, or outside.

In addition, from indices of intracellular metabolism, it is possible to judge the state of cells and the direction and intensity of their activity. Thus, for example, every stage of differentiation is intimately connected with the activation of additional ferment systems and the formation of new biosynthesis mechanisms. The data of cytochemical investigations of fibroblasts cultivated under the flow conditions compared to indices under the stationary conditions indicate that the activity of both specific (alkaline phosphatase) and nonspecific (α-naphtylacetatesterase) ferment systems increases, which is indicative of the acceleration of the cell differentiation process. This is confirmed by the more significant (compared to the stationary case) decrease in the area of cell surface of fibroblasts cultivated under the flow conditions as a reflection of the degree of fibroblast mature.

Thus, at the cultivation of human fibroblasts *in vitro* under the conditions of the directed nutrient flow, the increased intracellular fermentative activity of fibroblasts is observed. Under the modulating influence of microenvironment factors (directed fluid flow, extracellular matrix), the process of cell differentiation into mature forms accelerates.

The data obtained extend the idea of the microenvironment influence on the morphofunctional state of cells of a fibroblast population and allow cellular mechanisms of development of fibrovascular proliferation in the eyeball to be studied from new positions.

Shadow Prices and Lyapunov Exponents

Ilknur Kusbeyzi Aybar

Yeditepe University, Istanbul,Turkey
Department of Computer Education and Instructional Technology
E-mail: ikusbeyzi@yeditepe.edu.tr

Abstract: A relation between the optimal solution of the optimization problem and the stability and bifurcation properties of the corresponding dynamical system is suggested in this work. There exists a relation between the optimal solution of an optimization problem and an equilibrium point of a dynamical system. In this sense stability properties, Lyapunov exponents and bifurcations of the resulting dynamical systems can be studied.
Keywords: Dynamical systems, Optimization, Lyapunov exponents.

1. Introduction:

Shadow price is the unit change in the objective function of the optimal solution of an optimization problem. The shadow price is equivalent to the Lagrange multiplier at the optimal solution in the nonlinear scenario. It is also referred to as the dual variable considering the Lagrangian is the dual problem of the original optimization problem. The gradient of the objective function is a linear combination of the constraint function gradients with the weights equal to the Lagrange multipliers. Investigations on various linear optimization problems can be formulated as dynamical systems [4]. Stability analysis, Lyapunov exponents and bifurcation patterns of the resulting dynamical systems can be studied in a localized manner [2]. There is a relation between the global optimum value of the optimization problem to the local stability analysis of the corresponding dynamical system. The bifurcation properties and Lyapunov exponents of the corresponding dynamical system can be studied. The aim is to compare these invariant parameters of the dynamical systems to the shadow prices of the optimization problem. The motivation for this is the fact that to calculate a Lyapunov exponent, each dynamical variable is given a small variation and the corresponding hypercube is allowed to evolve in time [1]. Let us start by defining an optimization problem as

$$\max\{f(x,y): ax + by = c\}$$

Then the Lagrangian function is given by (in the two variable case)

$$L(x,y,\lambda) = f(x,y) + \lambda(c - ax - by)$$

(with obvious generalization to higher dimensions) and by solving this function for its saddle point we obtain the shadow prices and the maximal utility, x^*, y^*, λ^*, given by the following formula:

$$\lambda^* = \frac{\frac{\partial f(x^*, y^*)}{\partial x}}{a} = \frac{\frac{\partial f(x^*, y^*)}{\partial y}}{b}$$

On the other hand, shadow prices are found by observing the change in the optimal solution under a similar variation on the constraint of the direct problem by relaxing the constraint or alternatively, varying the corresponding parameter of the objective function in the dual problem. The definitions for the Lyapunov exponents and shadow prices are thus related to a change due to a variation. The former is a familiar element of the theory of dynamical systems. The route to chaos leads to Lyapunov exponents and this work introduces a new point of view for shadow prices as chaos search in dynamical systems [3]. Under the assumption that f be differentiable and $y_0 \neq 0$ the variational equation is:

$$y_{t+1} = \frac{df(x_t)}{dx} y_t$$

Then the Lyapunov exponent is defined to be

$$\lambda(x_0, y_0) = \lim_{n \to \infty} \frac{\ln \left| \frac{y_n}{y_0} \right|}{n}$$

A negative Lyapunov exponent indicates a stable equilibrium point and a positive Lyapunov exponent indicates chaos. So Lyapunov exponents are studied numerically to see if the given system shows chaos for certain parameter values. It has been proven that discrete-time dynamical systems are used in optimization algorithms. We also know that a discrete-time dynamical system can be transformed into a continuous dynamical system, i.e. system of differential equations by Euler's method. Both proofs depend on Lyapunov stability theory.

2. Optimization problem and corresponding dynamical system

Theorem 2.1: For the optimization problem

$$\max f(x, y) = x^k + y^k$$

$$\text{with respect to } g(x, y) = 1 - x - y$$

the extremum values are $(x^*, y^*) = (\frac{1}{2}, \frac{1}{2})$ and the general term of each Lagrange multiplier is $\lambda^* = -\frac{k}{2^{k-1}}$.

Proof:

$$\nabla f = \{kx^{k-1}, ky^{k-1}\}$$

$$\nabla g = \{-1, -1\}$$

$$k\begin{bmatrix} x^{k-1} \\ y^{k-1} \end{bmatrix} = \lambda^* \begin{bmatrix} -1 \\ -1 \end{bmatrix}$$

$$\lambda^* = -k\begin{bmatrix} x^{k-1} \\ y^{k-1} \end{bmatrix}$$

$$x^{k-1} = \frac{1}{2^{k-1}}$$

$$\lambda^* = -\frac{k}{2^{k-1}}$$

3. Bifurcation analysis:

The optimization problem discussed in the previous section can be considered as the corresponding dynamical system according to the Euler scheme:

$$\dot{x} = x^k + y^k - x$$

$$\dot{y} = 1 - ax - by - y$$

Investigating the bifurcation analysis of this system around the trivial equilibrium point, two different bifurcation patterns are achieved according to the value of *k* being odd or even. The first case where *k* is even (*k*=2,4,…) and *a* is chosen as the bifurcation indicates a limit point (LP) and a Bogdanov-Takens (BT) bifurcation point as given in Figure 2.1. When *b* is varied another case where a subcritical Hopf bifurcation point and a transcritical bifurcation point are observed as given in Figure 2.2. The second case where *k* is odd (*k*=1,3,…) and *a* is chosen as the bifurcation indicates two limit point (LP), a Bogdanov-Takens (BT) and a cusp (CP) bifurcation points as given in Figure 2.3. When *b* is varied another case where a subcritical Hopf bifurcation point and a transcritical bifurcation point are observed as given in Figure 2.4.

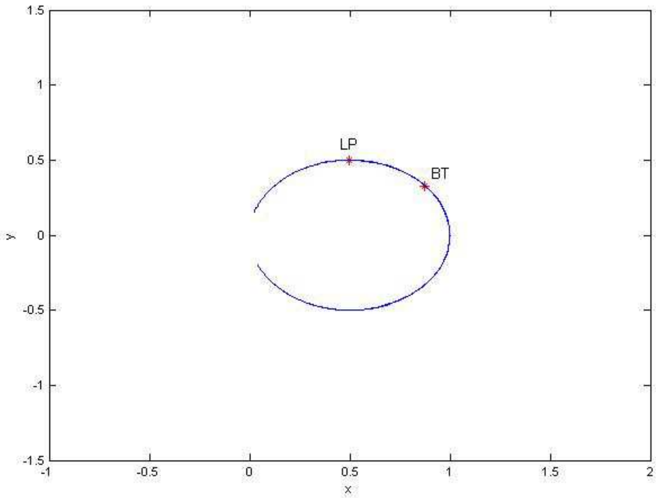

Figure 2.1. For even *k* (*k*=2,4,…) and arbitrary *a*

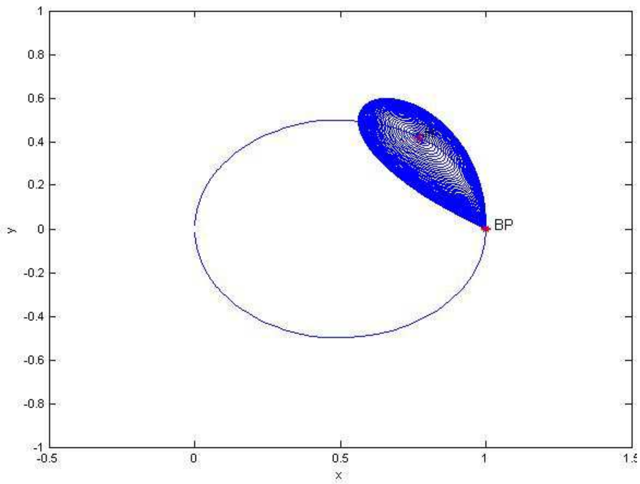

Figure 2.2. For even *k*(*k*=2,4,…) and arbitrary *b*

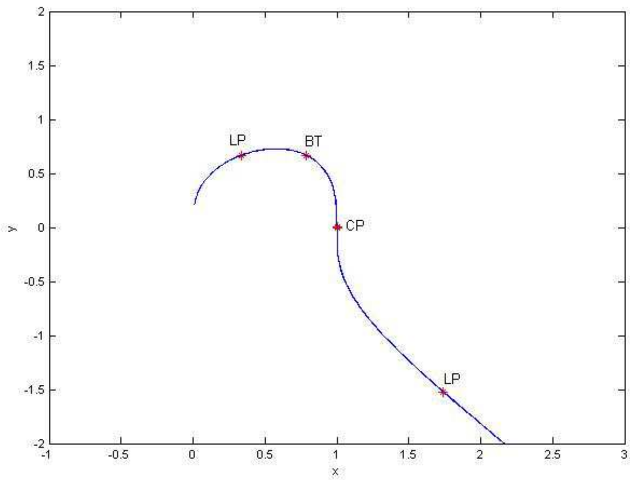

Figure 2.3. For odd *k* (*k*=3,5,…) and arbitrary *a*

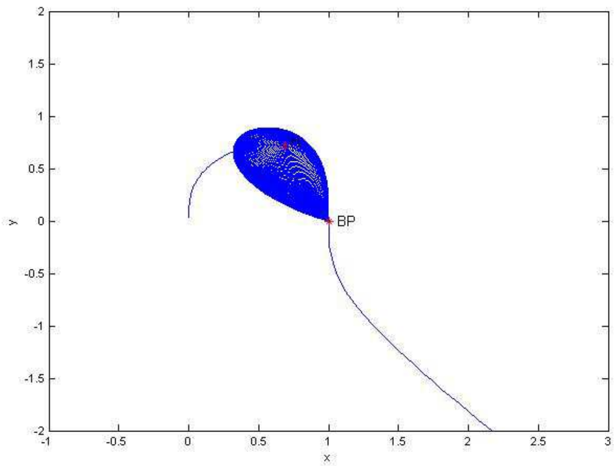

Figure 2.4. For odd *k* (*k*=3,5,…) and arbitrary *b*

4. Conclusion

The parameter b in our model indicates subcritical Hopf bifurcation for both even and odd cases of k. Bogdanov-Takens bifurcation is observed in all of the cases. Cusp bifurcation is observed for odd values of k. The higher nonlinearity for x and y does not affect the bifurcation phenomena. There are two different bifurcation patterns for odd and even values of k. Real values are taken into consideration in order to study real world situations.

References

1. A. Wolf, J.B. Swift, H.L. Swinney, J.A. Vastano. Determining Lyapunov exponents from a time series, *Physica D*,16, 285–317, 1985.
2. F. Verhulst. *Nonlinear Differential Equations and Dynamical Systems*. Second Edition Springer, 1939.
3. M. Sano and Y. Sawada. Measurement of the Lyapunov Spectrum from a Chaotic Time Series. *Physical Review Letters,* 55, 1082-1085, 1985.
4. U. Helmke. Balanced realizations for linear systems: a variational approach. *SIAM J. Control Optim,*. 31, 1–15, 1993.

Proceedings, 5th Chaotic Modeling and Simulation International Conference, 12 – 15 June 2012, Athens Greece

Acoustic metrology: from atmospheric plasma to solo percussive Irish dance

V J Law[1]*, Mick Donegan[1] and Breege Creaven[2]

[1]Surface Engineering Group, School of Mechanical and Materials Engineering, University College Dublin, Belfield, Dublin 4, Ireland
*(e-mail: victor.law@ucd.ie)
[2]School of Nursing, Midwifery & Health System, University College Dublin, Belfield, Dublin 4, Ireland

Abstract: LabVIEW software is used to decode step sequences generated by Irish light and hard shoes and bare feet. To remove the low frequency reverberation of the floor a Savitzky-Golay digital filter is used to de-convolute the percussion sound of the step sequences. Floor types and foot apparel are compared.

Keywords: Irish step dance, LabVIEW software deconvolution.

1. Introduction

In the last 5 years acoustic metrology [1, 2, 3 and 4] as a means of controlling an atmospheric pressure plasma-surface manufacturing processes has been developed. The origins of this metrology go back to W. Duddell's [5] and V. Paulson's [6] ionised gas sound production experiments at the turn of 19th - 20th century when radio technology was in its infancy. Today's atmospheric plasma metrology uses advanced digital time- and frequency-domain instrumentation linked to principal component analysis techniques to capture the interaction between the plasma and treated surface. This work extends this acoustic metrology into the world of solo step dance, in particular the examination and comparison of Irish hard shoe, Irish light shoe and bare feet. The percussion plates on Irish hard shoes are constructed from fibreglass or fibreglass composites. These are constructed in a solid piece and are fixed to the base of the front of the shoe with glue and to the heels with nails/screws. American tap shoes use plates constructed from a thin piece of steel and are loosely fixed to the shoe using screws. This difference in material and shoe/plate bonding results in a very different sound signature between the two shoe types. The Irish shoe gives a deep 'woody' sound when struck, while the loosely fixed steel plates of the American tap shoe has a hollow 'tinny' sound. The loose bonding of the American percussive plates result in a distinctive double tap per strike while the tightly adhered Irish plates result in a single tap per strike. These two distinctive toe and heel tap styles are universally used in record attempts in speed dancing. We use sound recording software that was developed to capture and analyse atmospheric pressure plasma acoustics. To evaluate the techniques we sample and compare bare feet and Irish light shoes, and Irish hard shoes striking a ceramic tiled floor and a wooden surface.

2. LabVIEW software

The sound recording and deconvolution analysis used in this study uses National instrument LabVIEW 20011 software program running on a Dell laptop. The recordings where made using a standard sampling rate of 44100 S/s and a 24 Bit depth. Decoding of recorded time-series dance rhythms and an Irish traditional dance sequence, danced to the tune of 'Abe's axe', a reel from Gráda's Natural Angle album (Compass Records), are used to demonstrate how a Savitzky-Golay (SG) moving window digital filter [3, 6] can be used to piece-by-piece de-convolve the low frequency reverberation response of the floor surface (wood and tile) as the dancers shoes (and bare feet) strike the floor surface. The SG filter uses a least square minimisation operation with a polynomial function (m = 1). The windowing operation is expressed in the following form, where k is the ± sampled data points. The block diagram of the LabVIEW deconvolution software is shown in Fig 1.

$$2k + 1 \qquad (1)$$

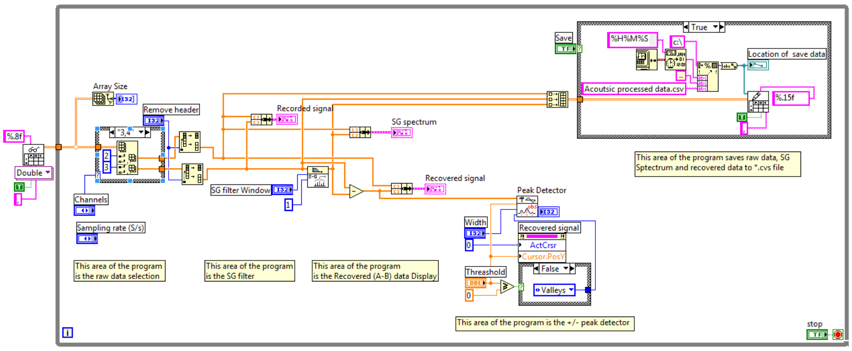

Figure 1: Block diagram of LabVIEW de-convolution software

2.1 Dance shoes

The Irish dance shoes used in this study are manufactured by Hullachan Pro. (Glasgow, Scotland). The Irish light shoes are the Hullachan H1 leather soled pumps while the Irish hard shoes are Hullachan HIJ Jig shoes with fibreglass composite percussion plates on the toes and polyurethane top on the heels.

3. Results

Three sets of dance recordings were made and the recordings analysed using the NI software program. The first and second set of recordings where taken of two subjects (one female and one male, having a European shoe size of 38 and 41, respectively) dancing to the rhythm of 'Abe's Axe'. In the first test the dancers were in bare feet and then the female dancer with Irish light shoes. Finally both wore the traditional Irish hard shoe. The floor surface was also changed from wood to ceramic tile. The sound recordings were taken at distance of 1 meter for the bare feet sequence and 3 meter for the shoe recordings. The third set of sound recordings where taken with the dancers wearing the Irish hard shoe and dancing to the rhythm of an Irish traditional step dance. Again a wooden floor and ceramic tiled floor were used. The results of the sound measurements and their de-convolution are set out in sections as follows: 3.1 surveys the four percussive impacts to the bar using bare feet and Irish light shoes; section 3.2 looks at the traditional Irish step dance. And section 4 provides the conclusion.

3.1. Bare feet and Irish light shoes

In this section the LabVIEW software is employed to decode a sequence of 4 percussive impacts to the musical bar, which is repeated for 8 bars. The foot timing is kept by the dancer listening (through an ear piece) to the tune of 'Abe's Axe'. The recording microphone is placed 1 meter in front of the dancer. The 4 percussive impact sequence, which is repeated 8 times, is:

1 = Right Toe
2 = Right Heel
3 = Left Toe
4 = Left Heel

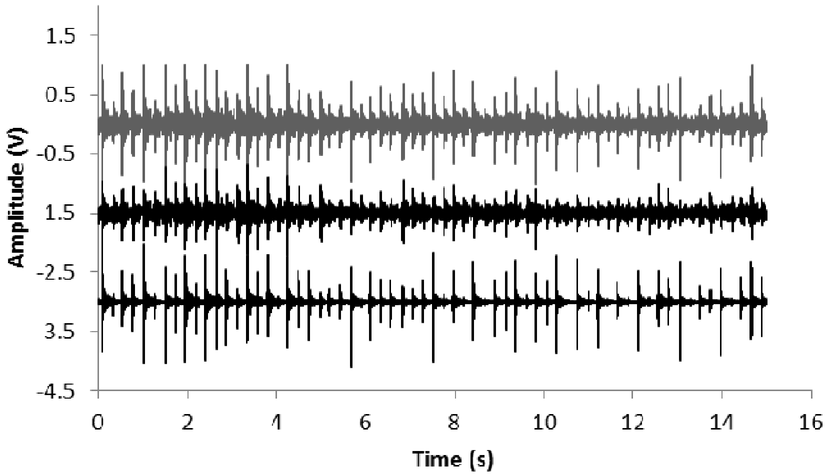

Figure 2: Bare foot recording and its de-convolution. Upper trace is the raw recording, middle the sythenic floor and lower trace depicts the step sequence.

Figure 2 shows a triplet of time-base traces, for clarity each trace is offset from each other. The upper trace is the raw sound recording of a male dancer performing the percussive sequence on a wooden floor surface; the middle trace is the synthetic floor that is produced by the SG window of ±10 samples; and the lower trace is the recovered (raw - synthetic floor) step sequence. A comparison of the three traces reveals that the recovered step sequence has the same amplitude as the raw data with an alternating high-low impulse sequence with a timing interval of 0.2 seconds. Given that human perception of loudness [8] is subjective, an objective measure would be the bandwidth of the impulse caused by the foot striking the floor. For this reason the acoustic signature are measured and used as a comparison with the hard shoe in section 3.2 Typically high impulses have an attack rise time of ~micro seconds, a sustain period of ~0.01seconds and decay a time of ~0.2 seconds to the zero-crossing point reference line. Figure 3 shows the dance percussion analysis (decoding) of the recovered step sequence discussed in Figure 2. The step sequence starts with the strike of the right toe (1) followed by the strike of the right heel (2) which has a reduced applied weight signature. The sequence continues with the toe (3) and heel (4) of the left foot and the completion of the first bar. From here the beats repeat to the end of the 8 bars and then repeat for second 8 bar sequence. The complete double sequence reveals 2 details of the male dancer. First, the dancer appears to reduce his applied weight in the beats of bars: 6, 7, and 8 bar of the first beats sequence. Second the dancer appears to be cognisant of the upping and coming end of the 8^{th} bar: this is illustrated by the added etherise (weight) to the start of second 8 bar sequence.

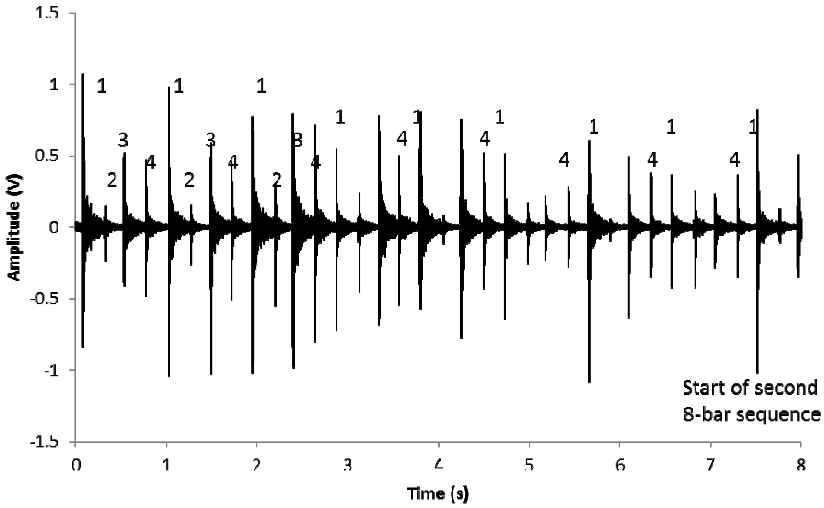

Figure 3: Decoding of the recovered male percussive impact sequence.

The required SG windowing to achieve minimum noise at the zero crossing point and linear time progression has been performed. The results of this analysis as a function floor type, male and female dancer and change to Irish light shoe for the female dancer is tabulated in table 1. The result shows that the necessary window is a constant ±10 samples across the matrix. Within these datasets the impulses amplitudes and beat timing are also constant, apart from were a momentary change in the dancer's balance generate an increase noise around the beats, see figure 4. In this example the dancer establishes balance in the first few bars of the dance sequence. However the recaptured composure is not sufficient to match the rhythm displayed in figure 3.

Table 1. SG window matrix for floor, sex with bare feet and soft shoe

Dancer	*Wooden floor bare feet*	*Title floor Bare feet*	*Wooden floors Soft shoes*	*Tile floor Soft shoes*
Male dancer	±10	±10		
Female dancer	±10	±10	±10	±10

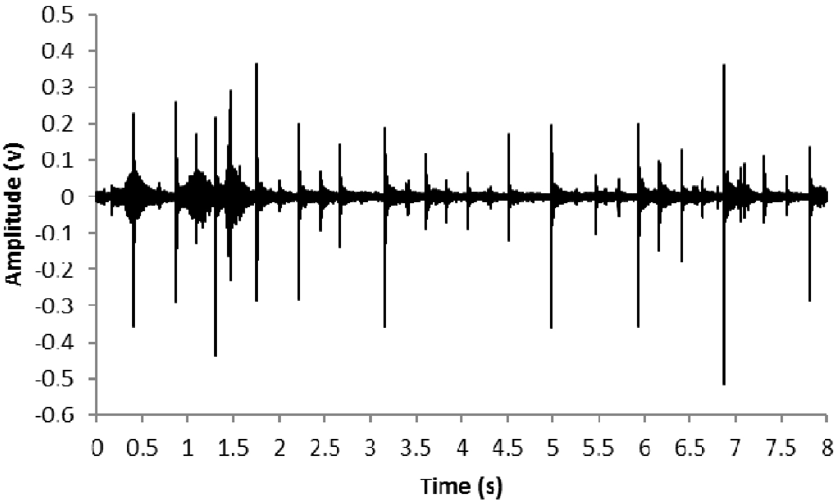

Figure 4: An example of dancer momentary weight imbalance.

3.2. Irish traditional step dance using a hard shoe

In this section a traditional step dance sequence is examined, again for two sequences. The acoustic signal is from the shoe impact on the floor producing a louder noise than that of the bare feet and Irish light shoe measurements, for this reason the microphone was placed some 3 meters away from the dancer and muffled. The tempo is set to produce a sequence of 8 bars two times over a 16 bar recording period. The sequence can be broken into 64 "beats" of equal duration. This 64 beats can be further broken into an 8 x 8 matrix. The dance sequence has 6 different types of percussive impacts and therefore 6 repeating sounds, the letters A, B, C, D, E & **F** (**F** being a heavy strike of the foot, and the silent gaps are represented with the letter P. In addition, letters that are underscored denote the left foot and the non-underscored letters denote the right foot. The full step sequence is shown in table 2. In table 2 the 2 letters **F** and **F** in the last line represents a double strike at the end of the first sequence. This is followed by a pause of duration 3 beats before the sequence is repeated. The repeat sequence leads with the "A" sound, which is made with the ball of the left foot. The foot movements of the letters are listed as follows:

Table 2.

Line	**Step 1**	**Step 2**	**Step 3**	**Step 4**	**Step 5**	**Step 6**	**Step 7**	**Step 8**
1	A	B	C	D	E	P	**F**	P
2	A	B	C	D	E	P	**F**	P
3	A	B	C	D	A	B	C	D
4	A	B	C	D	E	P	**F**	P
5	A	B	C	D	E	P	**F**	P
6	A	B	C	D	E	P	**F**	P
7	A	B	C	D	A	B	C	D
8	E	P	**F**	P	**F**	P	P	P

A = Ball of foot
B = Forward stroke
C = Backwards stroke
D = Hop (landing on ball of foot)
E = Ball of foot (similar to A but with less weight)
F = Strike with whole foot

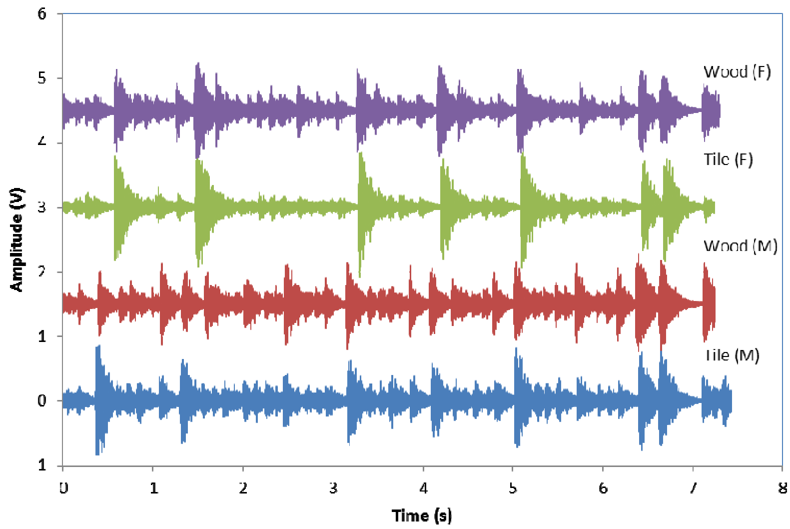

Figure 5: Comparison between male and female dancer performing the traditional Irish step dance on ceramic tile and wooden surface.

Four deconvolved acoustic time-series trace (synthetic floor removed: ±10 samples for the wooden floor and ± 22 sample points for the ceramic tile floor) of the traditional Irish step dance using the heavy shoes are shown in figure 5.

The traces are for both the female and male dancer on the ceramic tile and wooden floor, respectively. Each trace has been aligned to the double strike (**F**, **F**) and offset from each other to provide clear viewing. The traces provide an illustrative view of the individual step beats and their beat timing for both the wooden and ceramic tile floor. Note also the silent beats, in particular the triple silent gap at the end step sequence which allow the final F beat to exponentially decay before the start of the repeat step sequence. It is clear that there is a difference in emphasis on particular impacts for the two dancers. The female applies more weight to the F parts of the dance sequence when compared to the A, B, C, D & E sections of her sequence. The male dancer on the other hand delivers less variation in applied weight throughout his sequence. The result of this gives the female dancer the appearance of being lighter on her feet than the male, while the male appears louder overall. Figure 6 gives an analysis for the female dancer steps. In this sequence the F beats are stronger than the A beats as because of the area of the foot being used. However the A beats are stronger than the A beats, thus revealing a slight tendency to prefer the left foot. The figure also provides a qualitative comparison of loudness with the bare feet measurements. For example the sustain periods and decay periods are: typically 0.1 seconds and 0.5 seconds, respectively.

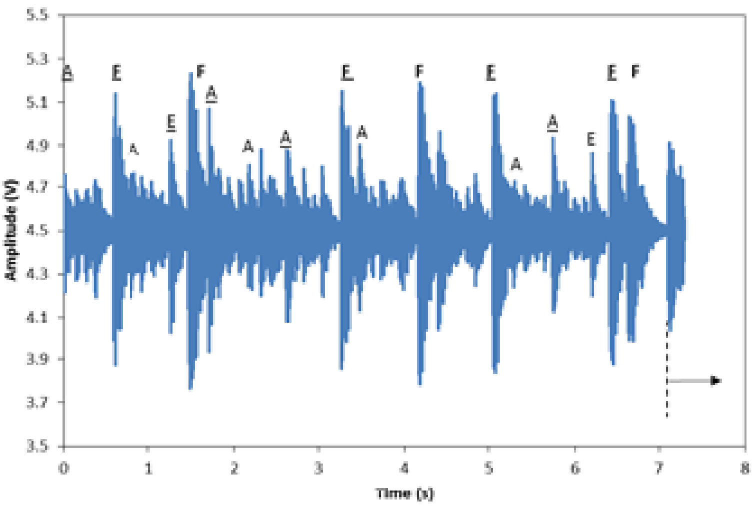

Figure 6: Percussive impact analysis of the female dancer performing the traditional Irish step on the wooden floor.

4. Conclusion

Acoustic recordings of two solo dancers performing the dance sequence and a traditional Irish step dance has been performed to the rhythm of ‘Abe’s Axe’. Shoe type (bare feet, Irish light shoes and Irish hard shoe) and floor type (ceramic tile and wooden floor) have been analysed. The analytical approach taken here has been to alter plasma diagnostic software that looks for periodic signals in stochastic noise, to that of one that subtracts low frequency reverberations from high frequency quasi-periodic impulses synchronised to the dancer's feet impacting on a dance floor. The deconvolution of these processes is performed using a SG digital filter with a moving window, $k = \pm 10$ for soft impact (bare feet and Irish light shoes) and $k = \pm 10$ to ± 22 for hard shoes.

The deconvolution process reveals that for bare feet and Irish light shoes the floor type does not have significant effect in the separation of the synthetic floor. A SG windowing of ±10 samples provides a clear deconvolution of the floor. For the hard shoe the ceramic tile and wooden floor respond differently to the foot impact: with wooden floor reverberating like an acoustic sounding board. Once the deconvolution process has been performed individual dance sequences within a rhythm can be identified and studied, including the recognition of left and right individual floor impacts. These software analysis attributes will make it possible to determine flaws during the performance of a dance piece. Discrepancies on dancers timing, applied weight, and overall dance sequence structure will be easily determined. It will also be possible to determine how a dancer performs using different equipment, for example a different pair of dance shoes and whether one shoe type suits a dancer over another. The software may help manufacturers of shoes to optimise the sound characteristics of different materials used in the making of the percussive plates as well as bench marking those currently on the market. In addition to Irish step dance, the step sequences in other distinctive percussive dances may be decoded, for example, but not exclusive to: the America Tap dance, Spanish Flamenco and the South America Tango.

References

1. J. Tynan, *et al*. Comparison of pilot and industrial scale atmospheric pressure glow discharge systems including a novel electro-acoustic technique for process monitoring. PSST, **19**, 015015, 2010.
2. V. J. Law, *et al*. Acoustic emission within an atmospheric helium discharge jet. *Chaos Theory: Modeling, Simulation and Applications*. 255-264. Eds: C. H. Skiadas, I. Dimotikalis and C. Skiadas. Publisher: World Scientific 2011).
3. V. J. Law, F. T. O'Neill and D. P. Dowling. Evaluation of the sensitivity of electro-acoustic measurements for process monitoring and control of an atmospheric pressure plasma jet system. PSST. **20**(3), 035024, 2011.
4. V. J. Law, *et al*. Decoding of atmospheric pressure plasma emission signals for process control. CMSIM **1**. 69-76. 2011.
5. J. Y. V. Music in electric arcs: an english physicist, with shunt circuit and keyboard, made them play tunes. The New York Times, 28 April, 7. 1901
6. A. N. Goldsmith. Modulation of the Poulsen arc. In: Radio Telephony 1918.
7. A. Savitzky & M. J. Golay. Smoothing and differentiation of data by simplified least squared procedures. *Analitical chemistr,* 36(8), 1627-2639, 1964.
8. H F Olson. The measurement of loudness. Audio. February, 18-22, 1972.

A Steganography Telecom System using a Chua Circuit Chaotic Noise Generator for data cryptography

Apostolos P. Leros (1,2) and Antonios S. Andreatos (2)

(1) Department of Automation, School of Technological Applications
Technological Educational Institute of Chalkis, 34400 Psachna, Evia, Greece
E-mail: lerosapostolos@gmail.com

(2) Div. of Computer Engineering & Information Science
Hellenic Air Force Academy, Dekeleia Air Force Base
Dekeleia, Attica, TGA-1010, Greece
E-mail: informatics.hafa@haf.gr, aandreatos@gmail.com

Abstract: This paper models an image steganography telecom system based on a Chua circuit chaotic noise generator. An unpredictable chaotic system based on a Master – Slave Chua circuit has been used as a random number generator. The whole system is modeled and simulated in Simulink. A continuous linear controller has been used to synchronize the two Chua circuits, with the same parameters at both the transmitter and the receiver. On the receiver side, usage of the same parameters with the Master circuit produce a similar chaotic signal via the Slave Chua circuit, synchronized to the Master by an analog controller, in order to produce the same noise (random sequence) as that of the Master circuit. After removing the noise from the received ciphertext, the original message is revealed. The proposed system presents advanced security features.
Keywords: Chua circuit, chaotic noise generator, image steganography, Master Chua circuit, Slave Chua circuit, LSB steganography, simulation, continuous linear controller.

1. Introduction

1.1 Random Number Generators

Traditionally, cryptography has been based on the generation of random numbers produced by hardware (true) random or pseudo-Random Number Generators (RNGs). Most pseudo-RNGs (PRNGs) are not suitable for cryptography for several reasons. First, while most pseudo-RNGs outputs appear random to assorted statistical tests, they do not resist determined reverse engineering. Specialized statistical tests that show the random numbers not to be truly random exist. Second, when the state of most PRNGs has been revealed, all past random numbers can be retrodicted, allowing an attacker to read not only future messages, but also, all past ones. This is not possible with a chaotic number generator; thus, Chua circuits resist this type of cryptanalysis. Furthermore, in our approach, even if the configuration circuit is revealed, it is still difficult to reproduce the crypto- signal since this also depends on the initial conditions and the tolerance of the components. The role of the continuous linear controller is to compensate for the component tolerance.

1.2 Steganography

Steganography is a technique for concealing data within pure or often encrypted or even random/ chaotic data. The data to be concealed is first encrypted and then used to overwrite part of a much larger block of encrypted data or random data or different kinds of (usually redundant) data such as images [10, 15, 16].

2. System Overview

In the proposed steganography telecom application, the message to be transmitted is first encrypted using chaotic noise produced by a standard Chua circuit [2, 4]; then, the encrypted sequence is concealed in an image using the LSB's method (Figure 1).

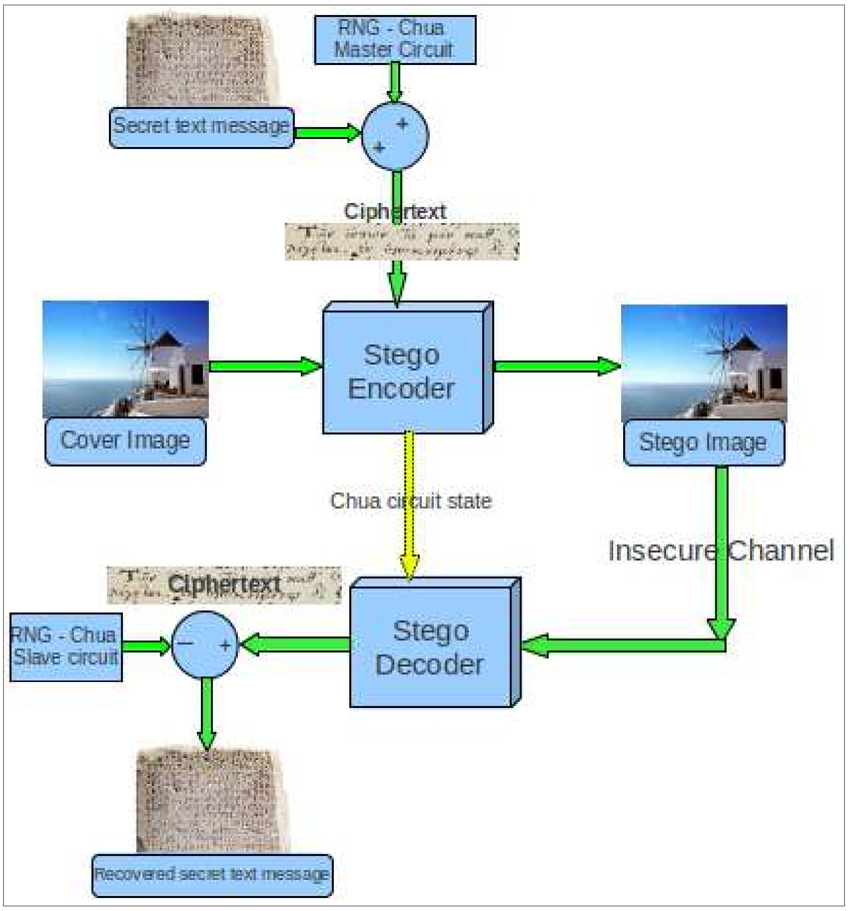

Fig. 1. Proposed steganography telecom application

The input message is in ASCII format; in order to be mixed with the chaotic noise, it is successively converted from ASCII characters to a binary string. For the sake of simplicity, conversions are not shown in Fig. 1. In the receiver the reverse process takes place, in order to remove the secret text from the image.

3. The Chaotic True Random Number Generator

The Chaotic True Random Number Generator (CTRNG) used by our circuit is based on the Standard Chua's circuit; the latter was invented back in 1983 by Prof. Leon O. Chua in Japan, in his effort to demonstrate chaos in an actual physical model and to prove that the Lorenz double-scroll attractor is chaotic [2, 4]. The electronic circuit suits the study of chaos well because one can precisely control its parameters and observe the results on an oscilloscope. The circuit became popular because it is easy to construct, and many people have built the circuit using off-the-shelf electronic components. In fact, one can model the circuit using only resistors, capacitors, inductors, diodes and op-amps [6].

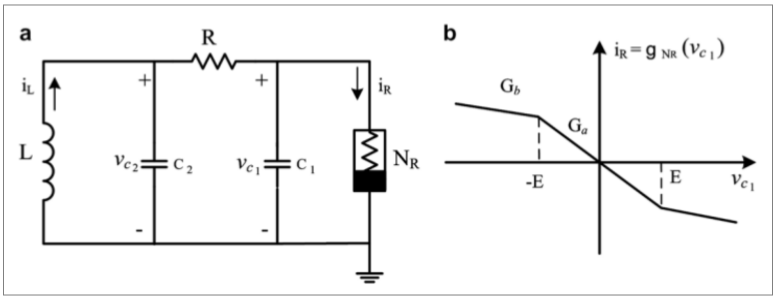

Fig. 2. (a) Standard Chua's circuit; (b) v–i characteristic of the nonlinear device Source: [4].

In Figure 2 V_{C1} and V_{C2} denote the voltages across the capacitors C_1 and C_2, respectively, i_L is the current through the inductor L, and $gN_R(V_{C1})$ is the nonlinear function which defines the v–i characteristic of the nonlinear device, represented by the piecewise-linear function of Fig. 2b [3]. By solving the above circuit we get the following differential equations (1- 4):

$$C_1 \frac{dVc_1}{dt} = \frac{1}{R}(Vc_2 - Vc_1) - g_{Nr}(Vc_1) \quad (1)$$

$$C_2 \frac{dVc_2}{dt} = \frac{1}{R}(Vc_1 - Vc_2) + i_L \quad (2)$$

$$L \frac{di_L}{dt} = -Vc_2 \quad (3)$$

$$g_{Nr}(Vc_1) = G_b Vc_1 + \frac{1}{2}(G_a - G_b)(|Vc_1 + E| - |Vc_1 - E|) \quad (4)$$

4. Simulink implementation

The whole telecom system was successfully implemented in Simulink [8]. In the following an overview of the system will be given; in addition, we shall present the implementation of some critical blocks.

4.1 Simulink implementation of the whole telecom system

The Simulink implementation of the cryptosystem was not as easy; several extra problems had to be solved starting from the input of the carrier image into Simulink; however, all problems were solved and finally the simulation works. The system overview is shown in Figure 3. Next the most important blocks will be briefly presented.

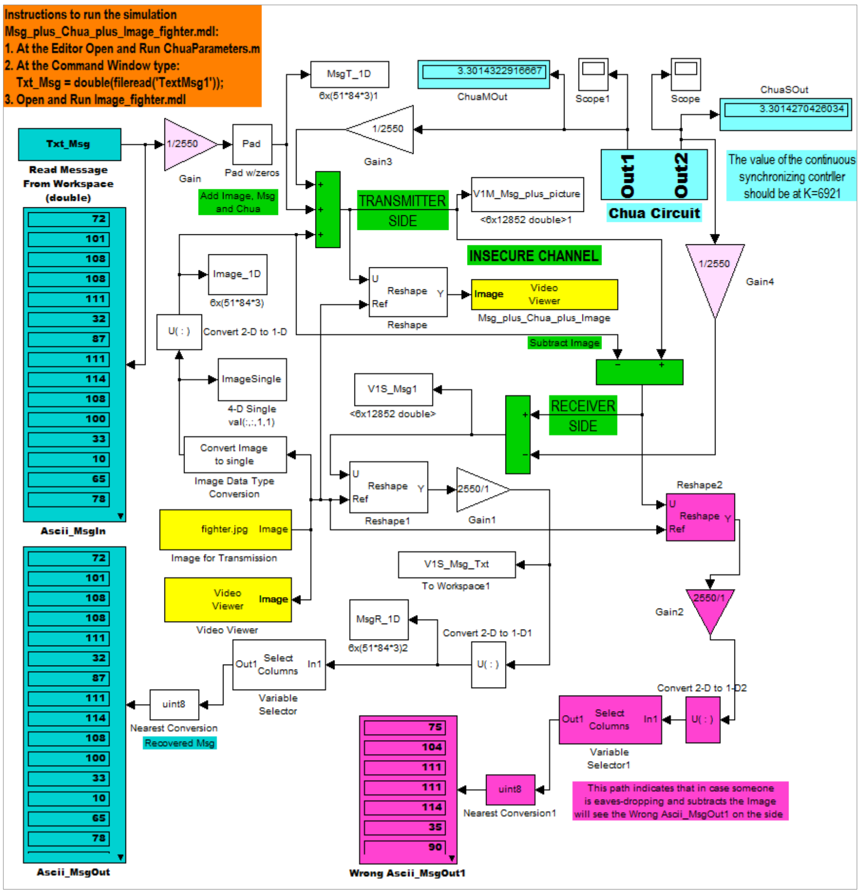

Fig. 3. Stego System overview in Simulink

The message to be encrypted appears on the left side (blue box with the indication Txt_Msg). The cover image for Transmission appears on the left side in the middle (yellow box named “Image for Transmission”). The Transmitter

occupies the top side of the diagram.
The summation element (in green) combines the image, the text message and the Chua chaotic noise, all properly formatted for compatibility. The image with the text message and the Chua chaotic value appears in the yellow box named **Msg_plus_Chua_plus_Image** below the Transmitter Side and it is also inserted into the channel.
The Chua circuits are on the top blue box with the indications Out1 and Out2 for the Master and Slave output values respectively. The value of the continuous linear controller which synchronized the two Chua circuits is **K=6921** as shown in the blue textbox (top right).
The receiver side occupies the bottom side of the diagram. In case an eavesdropper subtracts the image from the received information, he will see an invalid message (bottom right, in magenta).
Finally, at the bottom left side in the blue display with the indication **Ascii_MsgOut** the successfully recovered ASCII message appears.

4.2 Simulink implementation of Chua's circuits Figure 4 presents the Simulink implementation of Chua's circuit, based on the differential equations presented above. The Subsystem (bottom right) represents the nonlinear device.

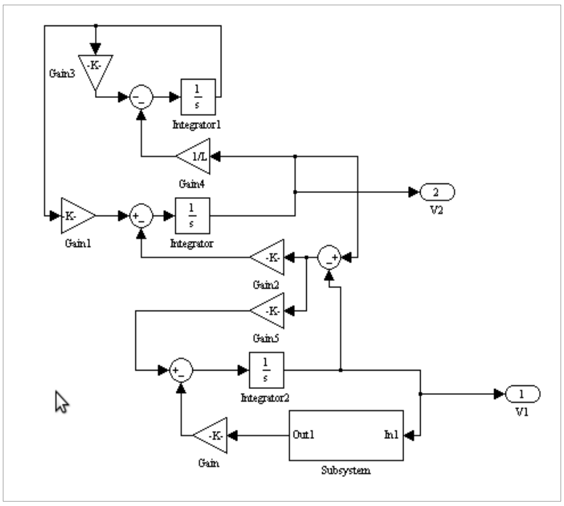

Fig. 4. Simulink implementation of Chua's circuit

4.3 Simulink implementation of the nonlinear device

Figure 5 presents the implementation of the nonlinear device with the v-i characteristic shown in Fig. 2b.

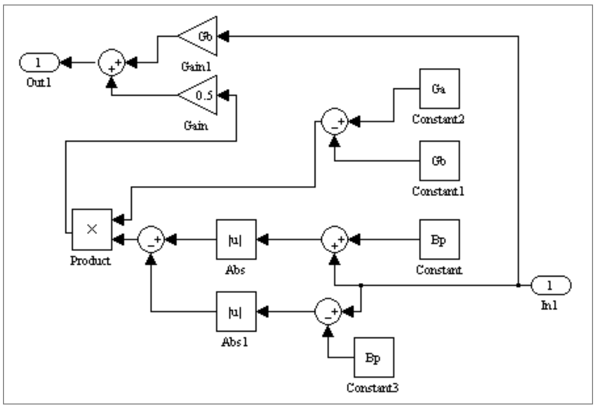

Fig. 5. Simulink implementation of the nonlinear device

5. Synchronization of the Master and Slave Chua circuits

5.1 The need for Master-Slave synchronization

Chaotic systems present an apparently infinite number of states. This characteristic, together with the dependence on the initial conditions as well as the tolerance of the Chua circuit components, make CTRNGs totally unpredictable and non-reproducible, hence ideal for cryptography. However, the receiver must be able to reproduce exactly the same chaotic noise in order to subtract it from the received signal (Figure 1). This becomes possible with synchronization between the two Chua circuits: through the use of specific controllers, we can guide the trajectory of chaotic systems to specific areas producing specific behavior. For this reason, the initial state of the Master Chua circuit [X0, Y0, Z0] has to be transmitted to the Slave Chua circuit via a secure channel (Fig. 6). In our implementation the initial conditions for the Master and Slave Chua circuits are: (Vc1=0, Vc2=1, I_L=0) and (Vc1=0, Vc2=1.1, I_L=0) respectively.

During the last two decades, the chaotic synchronization problem has received a tremendous interest [4]. This property is supposed to have interesting applications in different fields, especially in private and secure communication systems based on cryptography. The broadband and noise-like features of chaotic signals are seen as possibly highly secure media for communication. The cryptographic communication schemes usually consist of a chaotic system as transmitter along with an identical chaotic system as receiver; where the confidential information is embedded into the transmitted chaotic signal by direct modulation, masking, or another technique. At the receiver end, if chaotic synchronization can be achieved, then it is possible to extract the hidden information from the transmitted signal.

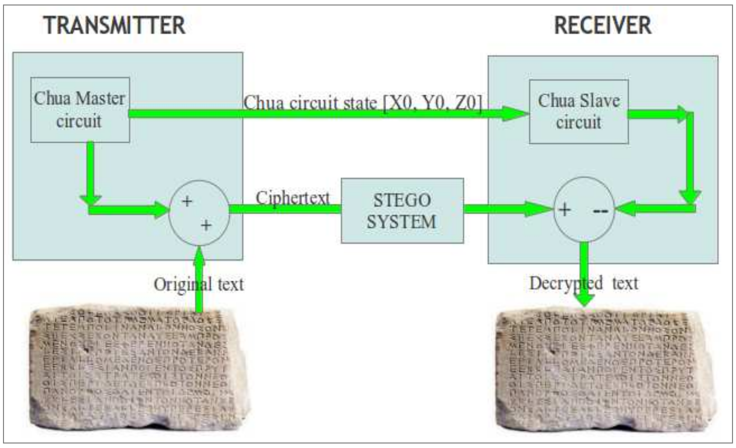

Fig. 6. Synchronization between Master and Slave Chua circuits

5.2 Master-Slave Synchronization circuit

For the synchronization between Master and Slave Chua circuits, Pyragas' continuous control method has been used [1, 3, 5, 7, 9, 11-14]. This method was chosen because it was relatively easy to implement. The synchronization circuit (simplified) is shown in Fig. 7.

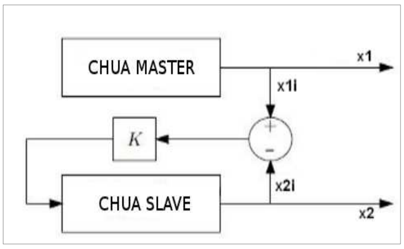

Fig. 7. Master-Slave Synchronization circuit

The Master and Slave Chua's circuits along with the Synchronization device are placed on the top-right side of Figure 4, in a block named Chua circuit. The interior of this block is shown in Figure 8 [6].

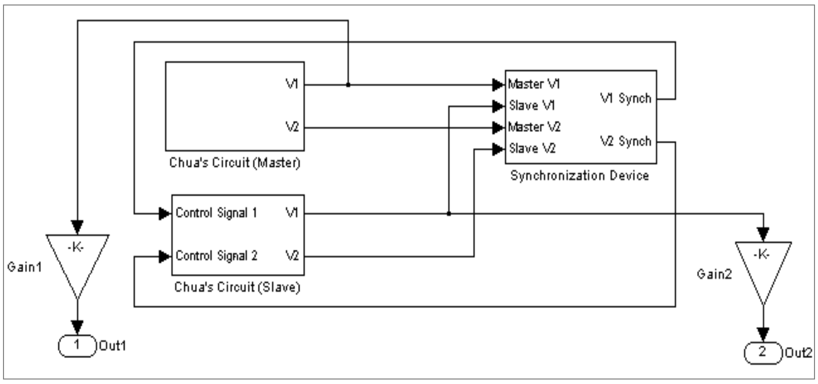

Fig. 8. Chua's circuits along with the synchronization device

6. Simulation results

Initial results show that the system works successfully. Using a small text message and the picture shown in Figure 9 as Cover image, the system produced the stego image of Figure 10.

Fig. 9. Cover image

Figure 10 contains the ciphertext, which is also shown (in ASCII) at the top left column of Figure 3. In this same Figure below we can see the decrypted message at the receiver. An eavesdropper with sufficient information about the image, even connected at a sensitive point of the receiver, won't be able to decode the message correctly, as shown at the bottom of Figure 3.

Fig. 10. Stego image

7. Security features of the proposed stegosystem

The security features of the proposed application are based on:

- ✓ the unknown Chua's circuit topology;
- ✓ the varying tolerance of components (which changes circuit behavior);
- ✓ the unknown initial conditions;
- ✓ the unknown type of the controller / compensator.

8. Conclusion

In this work we have proposed a Steganography Telecom System Based on a Chua Circuit Chaotic Noise Generator with advanced security features. In this system the text message is encrypted using a CTRNG and then the ciphertext is concealed in a cover image using the LSB insertion method. The system has been successfully simulated in Simulink and works with both grayscale and color images.

References

1. S. Boccaletti, C. Grebogi, Y.-C. Lai, H. Mancini, D. Maza, The Control of Chaos Theory and Applications. *Physics Reports*, Elsevier, 2000.
2. Leon O. Chua, Chua's circuit: ten years later. *IEICE Trans. Fundamentals*, vol. E77-A, no. 11, 1811-1822, Nov. 1994.
3. Alexander L. Fradkov and Robin J. Evans, Control of chaos: Methods and applications in engineering, *Annual Reviews in Control*, Elsevier B. V., 2005.

4. L. Gámez-Guzmán, C. Cruz-Hernández, R.M. López-Gutiérrez, E.E. García-Guerrero, Synchronization of Chua's circuits with multi-scroll attractors: Application to communication, *Commun. Nonlinear Sci. Numer. Simulat.* 14, 2765–2775, 2009.

5. J. Gonzalez, Synchronization and Control of Chaos, *An Introduction for Scientists and Engineers*. Covent Garden, London: Imperial College Press, 2004.

6. Nicholaos N. Grigoropoulos, *Chaotic Systems, Analysis and applications of Chua's circuit*. Diploma Thesis. Supervisor: Prof. A. P. Leros, Technological Institute of Chalkis, School of Technological Applications, 34400 Psachna, Evia, Greece, 2009.

7. T. Kapitaniak, *Controlling Chaos Theoretical and Practical Methods in non-linear Dynamics*. Elsevier Ltd., 1996.

8. Steven T. Karris, *Introduction to Simulink with Engineering Applications*. Orchard Publications, 2006.

9. F. L. Lewis, *Chaos in Automated Control.* Boca Raton, FL: Taylor & Francis Group, 2006.

10. T. Morkel, J.H.P. Eloff and M.S. Olivier, An Overview of Image Steganography, in *Proceedings of the Fifth Annual Information Security South Africa Conference* (ISSA2005), Sandton, South Africa, June/July 2005.

11. Louis M. Pecora, Thomas L. Carroll, Gregg A. Johnson, and Douglas J. Mar, Fundamentals of synchronization in chaotic systems, concepts, and applications. *American Institute of Physics*, 1997.

12. A. Pikovsky, Synchronization, *A universal concept in nonlinear sciences*. New York: Cambridge University Press, 2001.

13. K. Pyragas, Continuous Control of Chaos by Self Controling Feedback. *Physics Letters A*, 1992.

14. E. Schöll, *Handbook of Chaos Control*, 2nd Ed. Weinheim: Verlag GmbH & Co., 2008.

15. Mohit Kr. Srivastava, Sharad Kr. Gupta, Sushil Kushwaha and Brishket S. Tripathi, *Steganalysis of LSB Insertion Method in Uncommpressed Images Using Matlab*. Available online from: http://www.tutorialspoint.com/white-papers/124.pdf

16. Dr Ekta Walia and Payal Jain, An Analysis of LSB & DCT based Steganography, *Global Journal of Computer Science and Technology*, Vol. 10 Issue 1, 4-8, 2010.

Proceedings, 5th Chaotic Modeling and Simulation International Conference, 12 – 15 June 2012, Athens Greece

Newtonian and special-relativistic probability densities for a low-speed system

Shiuan-Ni Liang and Boon Leong Lan
School of Science, Monash University, 46150 Bandar Sunway, Selangor, Malaysia

Abstract. The Newtonian and special-relativistic predictions for the position and momentum probability densities of a model *low-speed* (i.e., much less than the speed light) dynamical system are compared. The Newtonian and special-relativistic probability densities, which are initially the same Gaussian, are calculated using an ensemble of trajectories. Contrary to expectation, we show that the predictions of the two theories can rapidly disagree completely. This surprising result raises an important fundamental question: which prediction is empirically correct?

INTRODUCTION

It is conventionally believed [1-3] that the predictions of special-relativistic mechanics for the motion of a dynamical system are well approximated by the predictions of Newtonian mechanics for the same parameters and initial conditions if the speed of the system v is *low* compared to the speed of light c ($v << c$). However, contrary to expectation, it was shown in recent numerical studies [4-8] that the Newtonian prediction for the trajectory of a low-speed dynamical system can rapidly disagree completely with the special-relativistic prediction.

In this paper, we extend the studies in [4-8] from the comparison of single-trajectory predictions to the comparison of the probability-density predictions calculated from an ensemble of trajectories. The model system we study here is the periodically delta-kicked system previously studied in [4]. Details of the model system and the probability-density calculations are presented next, followed by the results and concluding remarks.

MODEL SYSTEM

The periodically delta-kicked system [4] is a one-dimensional Hamiltonian system where a particle is subjected to a sinusoidal potential that is periodically turned on for an instant. The Newtonian equations of motion for this system are easily integrated exactly [9,10] to yield the well-known standard map, which maps the dimensionless scaled position X and dimensionless scaled momentum P from just before the nth kick to just before the (n+1)th kick:

$$P_n = P_{n-1} - \frac{K}{2\pi}\sin(2\pi X_{n-1}) \qquad (1)$$

$$X_n = (X_{n-1} + P_n) \mod 1 \qquad (2)$$

where n = 1,2,…, and K is a dimensionless positive parameter.

The special-relativistic equations of motion are also easily integrated exactly, producing a mapping known as the relativistic standard map [11,12] for the dimensionless scaled position X

and dimensionless scaled momentum P from just before the nth kick to just before the $(n+1)$th kick:

$$P_n = P_{n-1} - \frac{K}{2\pi}\sin(2\pi X_{n-1}) \tag{3}$$

$$X_n = \left(X_{n-1} + \frac{P_n}{\sqrt{1+\beta^2 P_n^2}} \right) \bmod 1 \tag{4}$$

where $n = 1,2, \ldots$, and β, like K, is a dimensionless positive parameter.

The initial probability density is a Gaussian for both position and momentum with means $<X_0>$ and $<P_0>$, and standard deviations σ_{X0} and σ_{P0}:

$$\frac{1}{2\pi\sigma_{X0}\sigma_{P0}} \exp\left[-\frac{(X_0 - <X_0>)^2}{2\sigma_{X0}^2} - \frac{(P_0 - <P_0>)^2}{2\sigma_{P0}^2} \right].$$

In each theory, the probability density is calculated using an ensemble of trajectories, where each trajectory is time-evolved using the map. The probability density is first calculated using 10^6 trajectories, where the accuracy of the double-precision calculation is determined by comparison with the quadruple-precision calculation. The probability density is then recalculated using 10^7 trajectories with the same accuracy determination. Finally, the accuracy of the probability density is determined by comparing the 10^6-trajectories calculation with the 10^7-trajectories calculation.

RESULTS

In the example presented here, the means and standard deviations of the initially Gaussian probability density are $<X_0> = 0.5$, $<P_0> = 99.9$ and $\sigma_{X0} = \sigma_{P0} = 10^{-10}$. The parameters of the maps are $K = 0.9$ and $\beta = 10^{-7}$.

Figures 1, 2 and 3 show that the Newtonian and special-relativistic position and momentum probability densities evolve approximately as Gaussians with increasing widths up to at least kick 114.

Figure 1 shows that, for both position and momentum, the Newtonian and special-relativistic probability densities are still close to one another on the whole at kick 80. The centers of the Newtonian and special-relativistic probability densities are displaced from each other in the figure because of the very small scale required for the horizontal axis to see the very narrow densities.

By kick 89, Figure 2 shows that, for both position and momentum, although the centers of the Newtonian and special-relativistic probability densities are still close, the Newtonian probability density is significantly wider and shorter than the special-relativistic probability density.

At kick 114, Figure 3 shows that not only are the widths and heights of the Newtonian and special-relativistic probability densities completely different for both position and momentum, the centers of the position probability densities are also completely different.

In summary, the three figures show that, although the mean speed of the system remains low, only 0.001% the speed of light, the Newtonian position and momentum probability densities disagree completely with the corresponding special-relativistic probability densities from kick 89 onwards.

CONCLUDING REMARKS

We have shown that, contrary to expectation, the Newtonian and special-relativistic probability-density predictions for a low-speed dynamical system can rapidly disagree completely.

Our result raises an important fundamental question: When Newtonian and special-relativistic mechanics predict completely different probability densities for a *low-speed* dynamical system, which of the two predictions is empirically correct? Since special relativity has survived many experimental tests in the high speed regime, it would be very strange indeed if the theory is invalid for low speed motion. If special relativity is also empirically correct at low speed as we expect, then it must be used, instead of the standard practice of using Newtonian theory, to correctly calculate the probability density for a low-speed dynamical system.

ACKNOWLEDGMENT

This study was supported by a Fundamental Research Grant Scheme, FRGS/2/2010/ST/MUSM/02/1.

REFERENCES

1. A. P. French, *Special Relativity* (Thomas Nelson & Sons, 1968), p. 167.
2. W. D. McComb, *Dynamics and Relativity* (Oxford University Press, 1999), preface.
3. J. B. Hartle, *Gravity: An Introduction to Einstein's General Relativity* (Addison-Wesley, 2003), p. 88.
4. B. L. Lan, Chaos **16**, 033107 (2006).
5. B. L. Lan, in *Topics on Chaotic Systems*, edited by C. H. Skiadas, I. Dimotikalis, and C. Skiadas (World Scientific, 2009), pp. 199-203.
6. B. L. Lan and H. Y. Cheng, Commun. Nonlinear Sci. Numer. Simulat. **15**, 2497 (2009).
7. B. L. Lan and F. Borondo, Phys. Rev. E **83**, 036201 (2011).
8. B. L. Lan, Chaos, Solitons and Fractals **42**, 534 (2009).
9. B. V. Chirikov, *Phys. Rep*. **52**, 263 (1979).
10. G. Casati, B. V. Chirikov, F. M. Izrailev, and J. Ford, in *Stochastic Behavior in Classical and Quantum Hamiltonian Systems*, edited by G. Casati and J. Ford (Springer, 1979), pp. 334–351.
11. A. A. Chernikov, T. Tél, G. Vattay, and G. M. Zaslavsky, *Phys. Rev. A* **40**, 4072 (1989).
12. Y. Nomura, Y. H. Ichikawa, and W. Horton, *Phys. Rev. A* **45**, 1103 (1992).

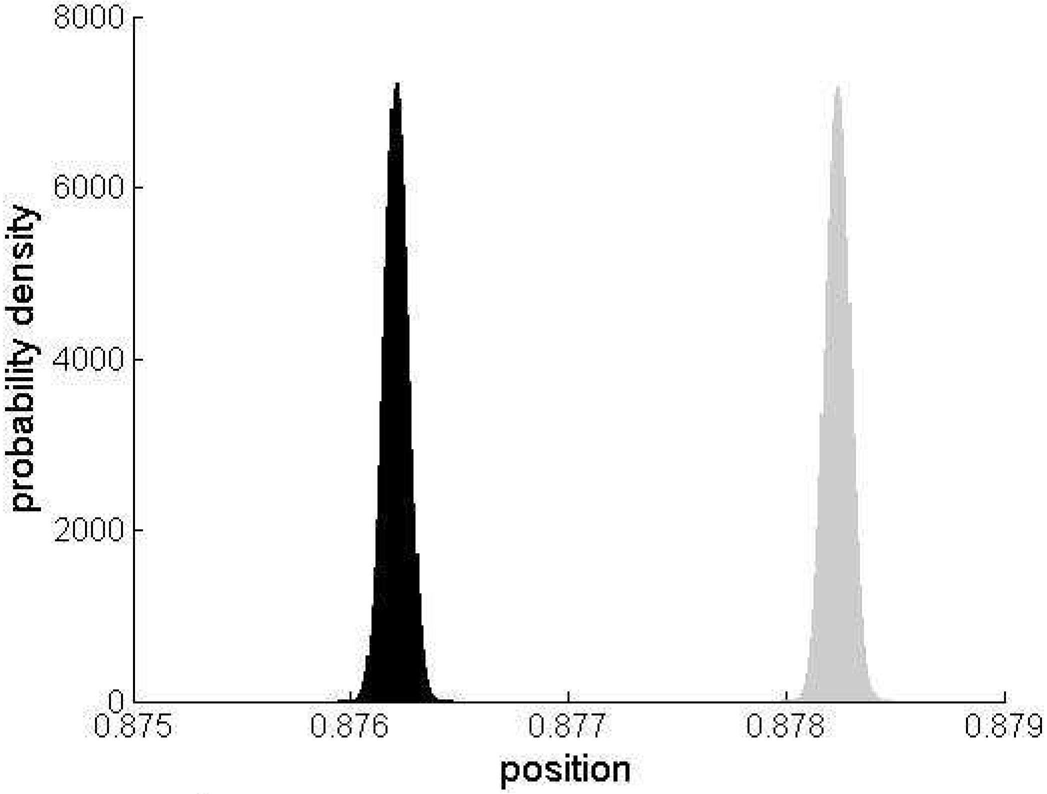

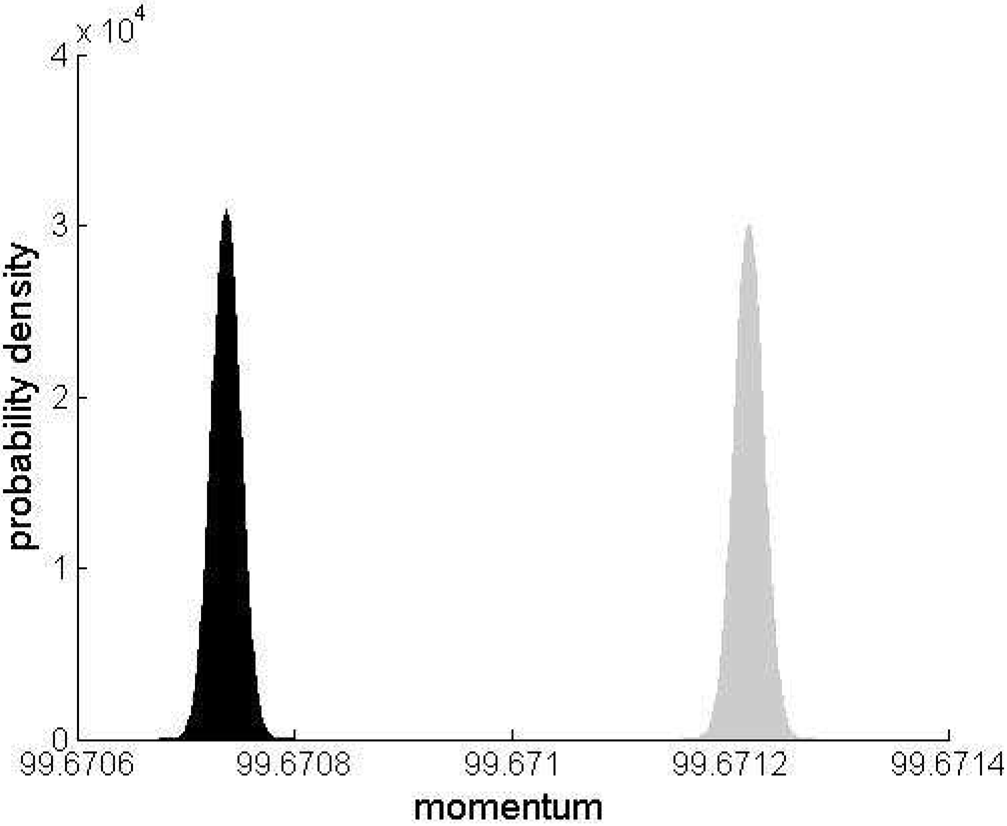

Figure 1. Comparison of Newtonian (grey) and special relativistic (black) position (top plot) and momentum (bottom plot) probability density for kick 80.

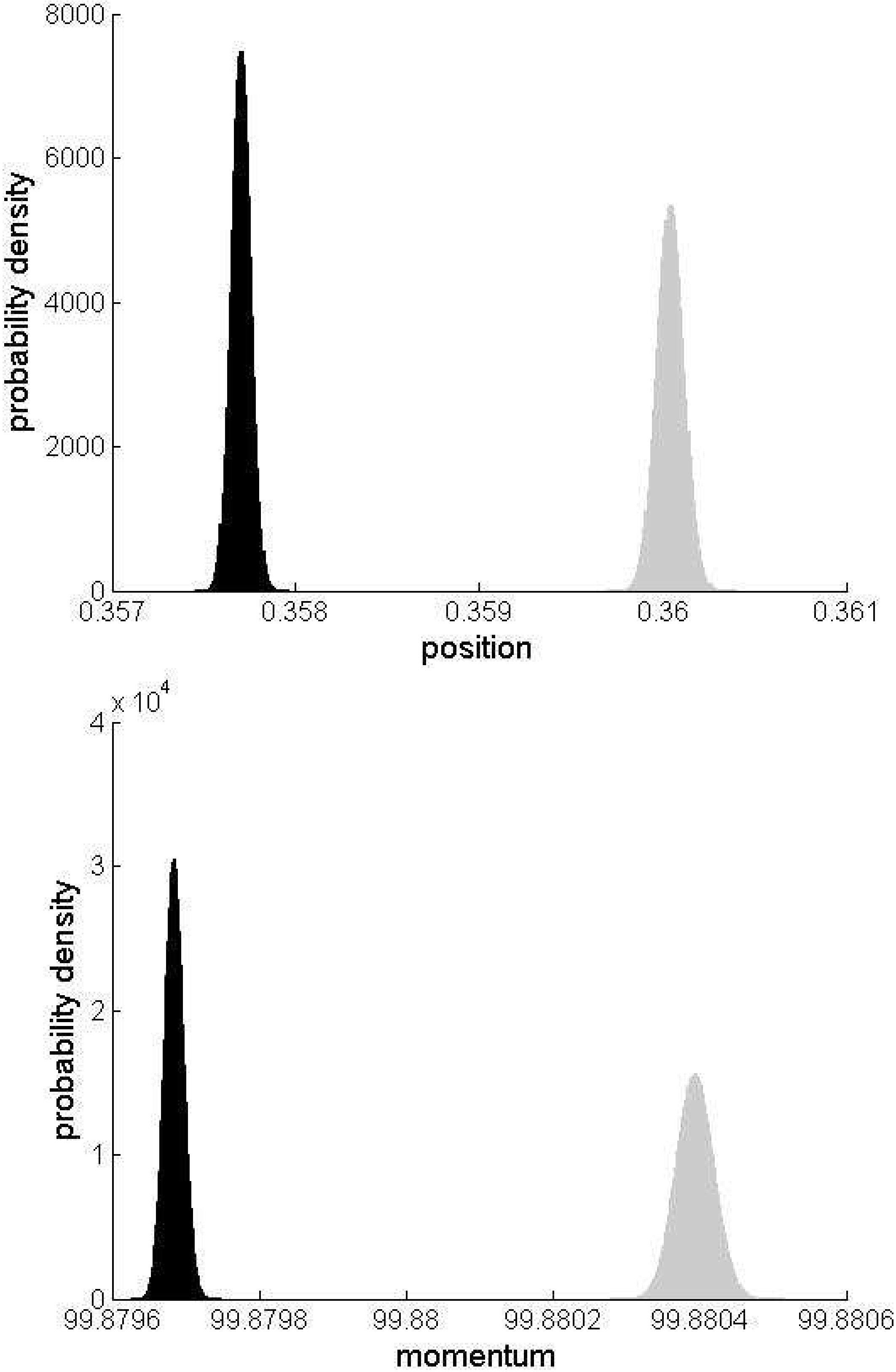

Figure 2. Comparison of Newtonian (grey) and special relativistic (black) position (top plot) and momentum (bottom plot) probability density for kick 89.

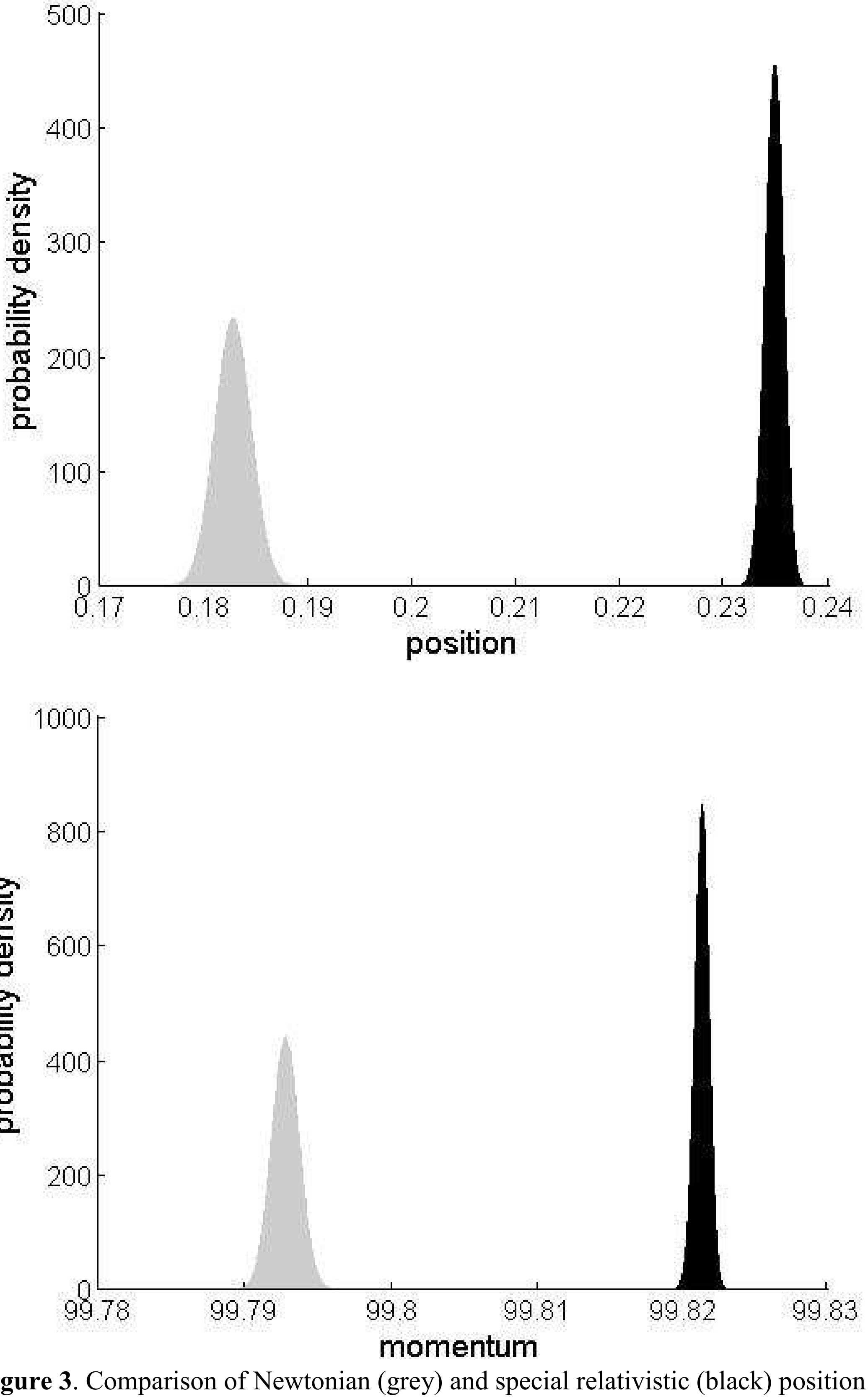

Figure 3. Comparison of Newtonian (grey) and special relativistic (black) position (top plot) and momentum (bottom plot) probability density for kick 114.

Proceedings, 5th Chaotic Modeling and Simulation International Conference, 12 – 15 June 2012, Athens Greece

Complex Dynamics and Phase Transitions Caused by Fuzzy Rationality

Ihor Lubashevsky[1] and Dmitry Parfenov[2]

[1] University of Aizu, Ikki-mach, Aizu-Wakamatsu, Fukushima, 965-8580, Japan (E-mail: `i-lubash@u-aizu.ac.jp`)
[2] General Physics Institute, Russian Academy of Sciences, Vavilov str. 38, Moscow, 119991, Russia
(E-mail: `narytyan@gmail.com`)

Abstract. The notion of dynamical traps is proposed to allow for effect caused by the bounded capacity of human cognition in ordering events or actions according to their preference. As a result, in the vicinity of an optimal behavior a decision-maker has no stimulus to change his current behavior. By way of example, one dimensional system of coupled oscillators with dynamical traps is studied numerically. The model assumes the dynamical traps to form a "low" dimensional region in the corresponding phase space where the system motion is stagnated. It is demonstrated that the dynamical traps and possible noise individually can cause the given system to exhibit complex dynamics and to undergo various phase transitions.
Keywords: Human behavior, Fuzzy rationality, Dynamical traps, Complex dynamics, Phase transitions.

1 Introduction

During the last decades there has been considerable progress in describing social systems based on physical formalism developed in statistical physics and applied mathematics (for a review see articles in Encyclopedia [1]). In particle, the notion of energy and the based on it master equation were employed to simulate opinion dynamics, the dynamics of culture and languages (e.g., [2–4]); the social force model inheriting the basic concepts from Newtonian mechanics was used to simulate traffic flow, pedestrian motion, the motion of bird flocks, fish schools, swarms of social insects (e.g., [2,5–7]). Continuing the list of examples, we note the application of the Lotka-Volterra model and the related reaction-diffusion systems to stock market, income distribution, population dynamics [8]. The replicator equations developed initially in the theory of species evolution were applied to the moral dynamics [9]. The notion of a fixed-point attractor as a stable equilibrium point in the system dynamics that corresponds to some local minimum in a certain potential relief, the collection of point type attractors forming a basin, the notion of latent attractors, periodic attractors representing limit cycles, and deterministic chaos are widely met in social psychology [10]. In addition, the concept of synchronization of interacting oscillators was used to model social coordination [11].

In spite of these achievements we have to note that the mathematical theory of social systems is currently at its initial stage of development. Indeed, animate beings and objects of the inanimate world are highly different in their basic features, in particular, such notions as willingness, learning, prediction, motives for action, moral norms, personal and cultural values are just inapplicable to inanimate objects. This enables us to pose a question as to what *individual* physical notions and mathematical formalism should be developed to describe social systems in addition to the available ones inherited from modern physics.

The present paper discusses one of such notions, namely, the fuzzy rationality [12] introduced here to describe the bounded capacity of human cognition in evaluating events, actions, etc. according to their preference. When, for example, two actions are close to each other in quality from the standpoint of a person making a decision their choice may be random because he ought to consider them equivalent. The notion of dynamical traps accounts for this feature. In particular, dealing with a dynamical system its stationary point $\mathbf{r}_{\text{st}}$ being initially stable is replaced by a certain neighborhood $\mathbb{Q}_{\text{tr}}$ called the dynamical trap region such that when the system goes into $\mathbb{Q}_{\text{tr}}$ its dynamics is stagnated. This mimics vain actions of an operator in directing the system motion towards the point $\mathbf{r}_{\text{st}}$ precisely. Indeed, when the system under the operator control gets any point in $\mathbb{Q}_{\text{tr}}$ the operator may consider the current situation perfect because he just does not "see" $\mathbf{r}_{\text{st}}$ and until the system leaves $\mathbb{Q}_{\text{tr}}$ he has no reason to keep the control active. The goal of the present work is to demonstrate that the fuzzy rationality can be responsible for complex emergent phenomena in such systems.

2 Lazy bead model

The following model captures the basic features of such human behavior. Let us consider a chain of N "lazy" beads (Fig. 1). Each of these beads can move in the vertical direction and its dynamics is described in terms of the deviation $x_i(t)$ from the equilibrium position and the motion velocity $v_i(t) = dx_i/dt$ depending on time t, here the bead index i runs from 1 to N. The equilibrium position $x_i = 0$ is specified assuming the formal initial $(i = 0)$ and terminal $(i = N + 1)$ beads to be fixed. Each bead i "wishes" to get the "optimal" middle position with respect to its nearest neighbors. So one of the stimuli for it to accelerate or decelerate is the difference

$$\eta_i = x_i - \frac{1}{2}(x_{i-1} + x_{i+1})$$

provided its relative velocity

$$\vartheta_i = v_i - \frac{1}{2}(v_{i-1} + v_{i+1})$$

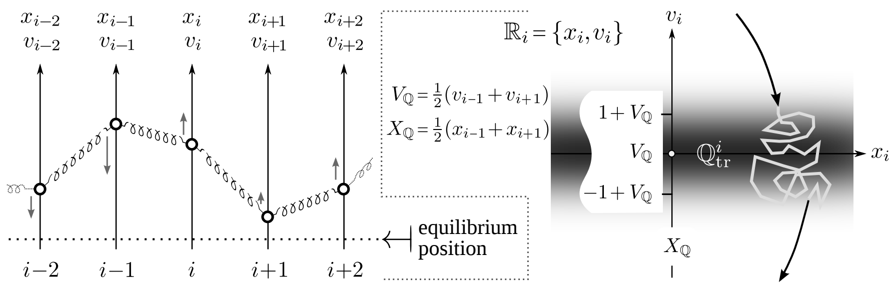

Fig. 1. The chain of N beads under consideration and the structure of their individual phase space $\mathbb{R}_i = \{x_i, v_i\}$ $(i = 1, 2, \ldots, N)$. The formal initial $i = 0$ and terminal $i = N + 1$ beads are assumed to be fixed, specifying the equilibrium bead position.

with respect to the pair of the nearest beads is sufficiently low. Otherwise, especially if bead i is currently located near the optimal position, it has to eliminate the relative velocity ϑ_i, representing the other stimulus for bead i to change its state of motion. The model to be formulated below combines both of these stimuli within one cumulative impetus $\propto (\eta_i + \sigma\vartheta_i)$, where σ is the relative weight of the second stimulus.

When, however, the relative velocity ϑ_i becomes less then a threshold θ, i.e., $|\vartheta_i| \lesssim \theta$, bead i is not able to recognize its motion with respect to the nearest neighbors. Since a bead cannot "predict" the dynamics of its neighbors, it has to regard them as moving uniformly with the current velocities. So from its standpoint, under such conditions the current situation cannot become worse, at least, rather fast. In this case bead i just "allows" itself to do nothing, i.e., not to change the state of motion and to retard the correction of its relative position. This feature is the reason why such beads are called "lazy". Below we will use dimensionless units in which, in particular, the perception threshold is equal to unity $\theta = 1$.

Under these conditions the equation governing the system dynamics is written in the following form

$$\frac{dv_i}{dt} = -\Omega(\vartheta_i)[\eta_i + \sigma\vartheta_i + \sigma_0 v_i] + \epsilon\xi_i(t)\,. \tag{1}$$

If the cofactor $\Omega(\vartheta_i)$ were equal to unity, the given system would be no more then a chain of beads connected by elastic springs characterized by the friction coefficient σ. The term $\sigma_0 v_i$ with the coefficient $\sigma_0 \ll 1$ that can be treated as a certain viscous friction of the beads moving via a medium into which the given system is embedded has been introduced to prevent the beads from attaining extremely high velocities. The factor $\Omega(\vartheta_i)$ is due to the effect of dynamical traps and the ansatz

$$\Omega(\vartheta) = \frac{\Delta + \vartheta^2}{1 + \vartheta^2}\,, \tag{2}$$

is used, where the parameter $\Delta \in [0,1]$ quantifies the intensity of dynamical traps. If $\triangle = 1$, the dynamical traps do not exist at all, in the opposite case, $\triangle \ll 1$, their influence is pronounced inside the neighborhood $\mathbb{Q}^i_{\mathrm{tr}}$ of the axis $v_i = (v_{i-1}+v_{i+1})/2$ (the trap region) whose thickness is about unity (Fig. 1). Model (1) allows for random factors in terms of white noise $\xi_i(t)$ affecting the motion of bead i with intensity ϵ so that

$$\langle \xi_i(t) \rangle = 0 \quad \text{and} \quad \langle \xi_i(t)\xi_{i'}(t') \rangle = \delta_{ii'}\delta(t-t')\,. \tag{3}$$

For the terminal fixed beads, $i = 0$ and $i = N + 1$, we set

$$x_0(t) = 0\,, \qquad x_{N+1}(t) = 0\,, \tag{4}$$

which play the role of the "boundary" conditions for equation (1).

It should be noted that the emergent phenomena in a similar system mimicking car following dynamics were considered for the first time in Refs [13,14]. In addition, the first experimental evidence of the dynamical traps caused by the human fuzzy rationality seems to be obtained in hybrid human-computer experiments of balancing a damped virtual stick [15].

3 Results of simulation

The dynamics of the given system was studied numerically. Initially all the beads were located at the equilibrium positions $\{x_i|_{t=0} = 0\}$ and perturbations were introduced into the system via ascribing random independent values to their velocities. Equation (1) was integrated using the E2 high order stochastic Runge-Kutta method [16]. The integration time step of 0.001 was used; the obtained results were checked to be stable with respect to decreasing the integration time step tenfold. The integration time was equal to 10^5–10^6, which enabled us to deal with the steady state dynamics. The other parameters used in simulation were taken equal to $\Delta = 10^{-3}$ and $\sigma_0 = 0.01$. Besides, to simply the data visualization the bead coordinates are shown with some individual shifts, namely, $x_i \to x_i + 50 \cdot i$.

In order to analyze the dynamical trap effect on its own the noise absence case was studied first. The system dynamics was found to depend on the intensity of "dissipation" quantified by the parameter σ. We remind that the parameter σ specifies the relative weight of the stimuli to take the middle "optimal" position and to eliminate the relative velocity; the larger the parameter σ, the more significant the latter stimulus. When the parameter σ is not too small the system tends to get the regime of regular dynamics represented by a collection of limit cycles of individual bead motion. It should be noted that these limit cycles could be of complex form when the number of beads is not too large, namely, $N \lesssim 10$ [17]. Nevertheless for systems with large number of beads the resulting phase portrait takes a rather universal form shown in Fig. 2(left frame). However, the "time to formation" T_N,

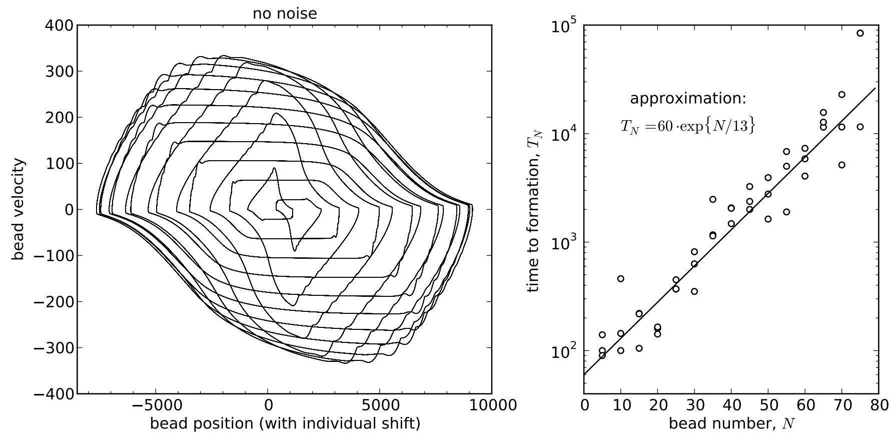

Fig. 2. The characteristic phase portrait of the steady state dynamics exhibited by systems without noise and not too weak "dissipation" (left frame). The chain of 30 beads with $\sigma = 1$ was used in constructing the shown pattern where the limit cycles of each second bead are visualized. The right frame depicts the characteristic time T_N required for such a system to get the steady state dynamics vs the number N of beads. The scatted points are the data obtained for each value of N on three trials, $\sigma = 1$ was used in simulation.

i.e. the mean time required for a given bead chain to get the steady state regular dynamics grows exponentially as the number of beads increases. For example, for beads with $\sigma = 1$ this time can be approximated by the function

$$T_N \approx T_c \cdot \exp\{N/N_c\} \qquad \text{with } T_c \sim 60 \text{ and } N_c \sim 13 \tag{5}$$

(see Fig. 2(right frame)). On one hand, this strong dependence explains that for chains of oscillators with not too weak "dissipation" only chaotic motion was found when the number of beads becomes sufficiently large, $N \gtrsim 100$ [17]. On the other hand, it enables us to pose a question about regarding the chaotic dynamics of such systems for $N \to \infty$ as a certain phase state.

In the case of weak "dissipation" the system dynamics exhibits sharp transition to a stable chaotic regime as the coefficient σ decreases. It is demonstrated in Fig. 3 showing the transition from the regular dynamics for $\sigma = 0.1$ to a chaotic motion when $\sigma = 0.09$. As seen in Fig. 3 the chaotic portrait can be conceived of as a highly chaotic kernel surrounded by fragments of the regular limit cycle destroyed by instability.

Noise forces these systems to undergo two phase transitions as its intensity ϵ increases. The first one can be categorized as the transition from the regular bead motion to a cooperative chaotic bead motion. The latter means that the beads correlate substantially with one another in motion but individual trajectories are rather irregular and the magnitude of this irregularity cannot

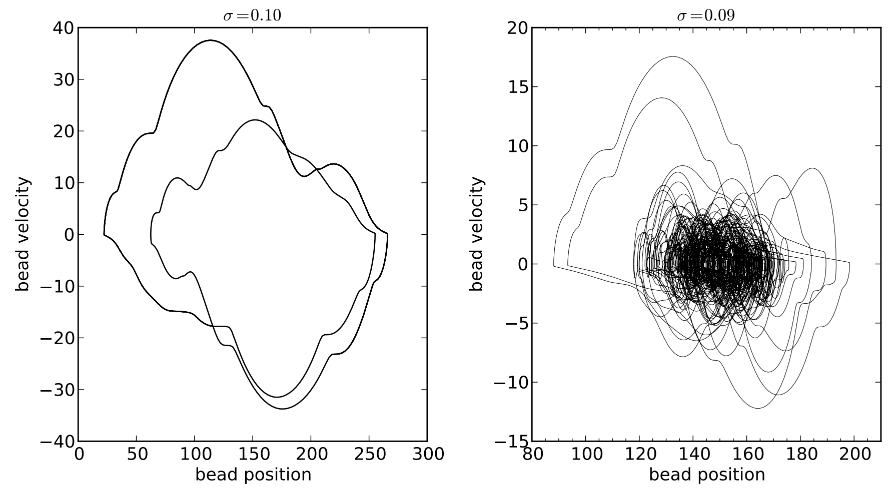

Fig. 3. The phase portraits of the middle bead motion of the 5-bead chain for the "dissipation" parameter σ taking the values 0.1 (left frame) and 0.09 (right frame). The period of the shown limit cycle is about 200; the chaotic phase portrait was obtained by visualizing the system motion within time interval about 5×10^5.

be due to the present noise only. The second transition is determined by the formation of highly irregular mutually independent oscillations in the bead position. To illustrate the first phase transition Figure 4 depicts two phase portraits of the middle bead motion for different values of ϵ. As seen, for $\epsilon = 0.01$ the phase portrait looks like a regular limit cycle disturbed by small noise. In contrast, when the noise intensity increases by two times, i.e., $\epsilon = 0.02$, the corresponding phase portrait becomes rather complex in form and the volume of the phase space layer containing the shown trajectory as a whole sharply grows. Exactly the two features has enabled us to classify the found effect as a phase transitions. It should be noted, that this phase transition from regular motion to stochastic chaos, in contrast to the second transition to highly irregular motion, does not manifest itself in the one-particle distributions of all the variables x, v, η, ϑ ascribed to the beads individually, so, it could be categorized as a "weak" phase transition.

4 Conclusion

The notion of dynamical traps was introduced to describe possible effects caused by the bounded capacity of human cognition in ordering events or actions according to their preference. Its particular implementation is that human beings as active elements of a certain system cannot individually control all the governing parameters within the accuracy required for stabilizing the system dynamics perfectly. Therefore one chooses a few crucial

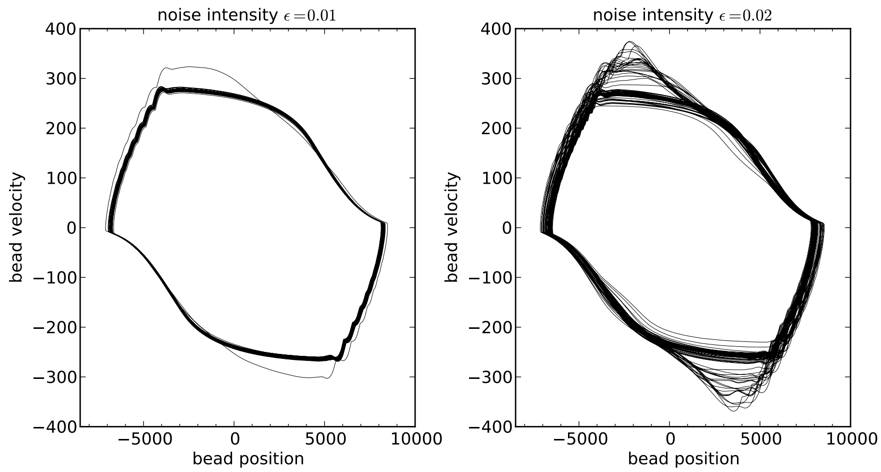

Fig. 4. The phase portraits of the middle bead motion of the 30-bead chain with $\sigma = 1$ for two values of the noise intensity $\epsilon = 0.01$ and 0.02. In plotting these portraits bead trajectories of motion during time interval about 2×10^4 were used.

parameters and mainly focuses attention on them. When the equilibrium with respect to these crucial parameters is attained the human activity slows down, retarding in turn the system dynamics as a whole.

By way of example, we considered emergent phenomena in chains of coupled oscillators with dynamical traps. The motion of oscillating particles (beads) in the phase space $\{x_i, v_i = \dot{x}_i\}$ is assumed to be governed by their interaction via effective elastic springs with viscous friction outside the dynamical trap region $\mathbb{Q}_{\mathrm{tr}}$. For a given bead i the dynamical trap effect is reduced to depressing its interaction with the nearest neighbors $i-1$ and $i+1$ as the relative velocity $\vartheta_i = v_i - (v_{i-1} + v_{i+1})/2$ becomes small in comparison with some threshold. The introduction of additive white noise of intensity ϵ allows for possible uncontrollable factors also affecting the bead motion.

This system was studied numerically. As demonstrated, without noise the system dynamics tends to the regime of regular bead motion if the friction coefficient is not too small. However, the characteristic time required for a given system to get this regime grows exponentially with the number N of beads. It enables us to pose a question about regarding the chaotic transient processes as a certain phase state in the limit $N \to \infty$. When the friction coefficient becomes sufficiently small the steady state dynamics of such systems can undergo transition to chaotic bead motion even for chains with small number of beads. Depending on its intensity noise can induce the formation of three characteristic phases, highly irregular individual oscillations of the beads, the cooperative chaotic bead motion, and the synchronized regular bead motion. It should be noted that the transition between the regimes of regular and cooperative chaotic bead motion manifests itself only the sharp growth of the volume of the phase space layer containing the bead trajectories, whereas all the one-particle distribution functions does not change their forms remarkably.

Acknowledgments

The work was supported in part by the JSPS "Grants-in-Aid for Scientific Research" Program, Grant # 245404100001.

References

1.R. A. Meyers (ed), *Encyclopedia of Complexity and Systems Science*, Springer-Science+Buisiness Media, LLC., New York, 2009.
2.C. Castellano, S. Fortunato, and V. Loreto. Statistical physics of social dynamics. *Rev. Mod. Phys.*, 81:591–646, 2009.
3.F. Slanina. Social Processes, Physical Models of. In Ref. [1], pages 8379–8405.
4.D. Stauffer. Opinion Dynamics and Sociophysics. In Ref. [1], pages 6380–6388.
5.D. Helbing and A. Johansson. Pedestrian, Crowd and Evacuation Dynamics. In Ref. [1], pages 6476–6495.
6.A. Schadschneider, W. Klingsch, H. Klüpfel, T. Kretz, C. Rogsch, and A. Seyfried. Evacuation Dynamics: Empirical Results, Modeling and Applications. In Ref. [1], pages 3142–3176.
7.D. Helbing. Traffic and related self-driven many-particle systems. *Rev. Mod. Phys.*, 73:1067–1141, 2001.
8.G. Yaari, D. Stauffer, and S. Solomon. Intermittency and Localization, in Ref. [1], pages 4920–4930.
9.R. Hegselmann. Moral Dynamics, In Ref. [1], pages 5677–5692.
10.R. R. Vallacher. Social Psychology, Applications of Complexity to. In Ref. [1], pages 8420–8435
11.O. O. Olivier and J. A. S. Kelso. Social Coordination, from the Perspective of Coordination Dynamics. In Ref. [1], pages 8198–8213.
12.K. K. Dompere. *Fuzzy Rationality*, Springer-Verlag, Berlin, 2009.
13.I. A. Lubashevsky, R. Mahnke, M. Hajimahmoodzadeh, and A. Katsnelson. Long-lived states of oscillator chains with dynamical traps, *Eur. Phys. J. B*, 44:63–70, 2005.
14.I. Lubashevsky, M. Hajimahmoodzadeh, A. Katsnelson, and P. Wagner. Noise-induced phase transition in an oscillatory system with dynamical traps. *Eur. Phys. J. B*, 36:115–118, 2003.
15.A. Zgonnikov, I. Lubashevsky, and M. Mozgovoy. Computer simulation of stick balancing: action point analysis. In V. Klyuev and A. Vazhenin (eds), *Proceedings of the 2012 Joint International Conference on Human-Centered Computer Environments (HCCE'12)*, ACM New York, NY, USA, 2012, pages 162–164.
16.P. M. Burrage. *Numerical methods for stochastic differential equations*. Ph.D. thesis, University of Queensland, Brisbane, Queensland, Australia, 1999.
17.I. Lubashevsky. Dynamical traps caused by fuzzy rationality as a new emergence mechanism. E-print: arXiv:1109.0072, to be published in ACS (2012).